INTERFACIAL INSTABILITIES OF SUSPENSIONS IN HELE-SHAW CELL

A Dissertation

by

FENG XU

Submitted to the Office of Graduate and Professional Studies of
Texas A&M University
in partial fulfillment of the requirements for the degree of

DOCTOR OF PHILOSOPHY

Chair of Committee,	Sungyon Lee
Committee Members,	Alan Palazzolo
	Eric Petersen
	Prabir Daripa
Head of Department,	Andreas Polycarpou

December 2017

Major Subject: Mechanical Engineering

ABSTRACT

The objective of this research is to investigate the interfacial instability of suspensions in a Hele-Shaw cell, which involves a dynamical coupling between particle transport and fluid-fluid interfacial deformations. Interfacial instabilities have remained an important subject of research given their complicated nature. They are commonplace in multiphase flows such as enhanced oil recovery, lung airways and micro-fluidic droplets, and controlling them is of critical importance. The inclusion of particles in fluid flows can also modify the interfacial dynamics, which yet remains not well understood.

The Saffman-Taylor fingering instability occurs when a less viscous fluid displaces a more viscous one in porous media, which has been extensively studied for decades. The interface is supposed to be stable in the reverse scenario, in which the more viscous fluid invades the less viscous one. Surprisingly, the inclusion of particles can fundamentally change the interfacial dynamics and even lead to interfacial instability in the absence of the unstable fluid viscosity ratio. This instability phenomenon was first reported by Tang *et al* and extended to squeezing suspension flows by Ramachandran. However, the research on this topic has remained qualitative.

In this research, we carry out rigorous experiments to characterize the fingering instability introduced particles, by varying the particle volume fraction and the gap thickness over particle diameter ratio h/D. The experimental data are analyzed utilizing advanced image processing techniques to aid our understanding of the phenomenon. Theoretically, we use the suspension balance model to validate the shear-induced migration upstream of the expanding interface and successfully explain the mechanism behind fingering. The project is then extended to bi-disperse suspensions. The experiments are conducted with particles having different diameters by varying both the bulk particle concentration and

the respective concentration of each particle species. We observe similar fingering patterns and find that the addition of small amount of large particles leads to an earlier onset of fingering. The suspension balance model is modified to accommodate the bi-disperse suspension system and then utilized to quantitatively explore the dynamics.

DEDICATION

To my dad Jiming Xu and my mom Yan Liu.

ACKNOWLEDGMENTS

When I sit by the table trying to look back the four and a half years life pursuing my PhD, it's hard not to get emotional. It reminds me of all those people come and gone, pains and joys soldier through courses and projects, goods and bads help to shape who I am today. I'm truly grateful that those years are well spent at a great university with the most fantastic people I could ever meet.

I want to take this chance to give my most respectful thanks to my advisor, Dr. Sungyon Lee. Thanks for the thoughtful and insightful suggestions in research, for the selfless help in life, for the candies and food, for the jokes and yells. I still feel lucky thinking of the day I became an official member of the group and I enjoyed every moment ever since.

Thanks to all members in my academic committee, Dr. Alan Palazzolo, Dr. Eric Petersen and Dr. Pabir Daripa, for providing valuable suggestions. Your contributions are highly appreciated.

Thanks to my dad and mom, who provide the strongest support in every aspect. I won't be able to make it thus far without your priceless love.

Thanks to my labmates and loyal friends Yun Chen and Aliriza Hooshanginejad, who give me valuable suggestions in both research and life. I'll treasure and honor the friendship throughout my life.

Thanks to Dr. Jungchul Kim, who used to work in lab as a postdoc for one year. I certainly learnt precious expertise from you.

Thanks to Dr. Tony Yu and Dr. Michael Allshouse for fruitful discussions, which help to improve the quality of data analysis.

Thanks to all the undergraduate students who used to be part of the team. Your contributions are really appreciated.

Thanks to my friends, both far away and around. I find lots of joy and happiness getting along with you all.

Thanks to the coffee shop in the Evan's library, where I grabbed tons of coffee.

I just couldn't say enough thanks to express how grateful I am. Sincere thanks to all of you from deep bottom of my heart!

CONTRIBUTORS AND FUNDING SOURCES

Contributors

This work was supported by a dissertation committee consisting of Professor Sungyon Lee (now at Department of Mechanical Engineering at University of Minnesota), Professor Eric Petersen and Professor Alan Palazzolo of the Department of Mechanical Engineering and Professor Prabir Daripa of the Department of Math.

All other work conducted for the thesis (or) dissertation was completed by the student independently.

Funding Sources

Graduate study was supported by Texas A&M Engineering Experiment Station (TEES).

NOMENCLATURE

PMMA	polymethyl methacrylate
PG	polyalkylene glycol
LDA	laser-Doppler anemometry
LDV	laser-Doppler velocimetry
NMR	nuclear magnetic resonance
SBM	suspension balance model
ANN	Artificial Neural Network
LoG	Laplacian of Gaussian

TABLE OF CONTENTS

Page

LIST OF FIGURES

FIGURE Page

LIST OF TABLES

TABLE Page

1. INTRODUCTION*

1.1 Interfacial Instability

Interfacial instabilities are ubiquitous both in nature and industry, and research in this area has remained active for the past few decades. For example, prior to the eruption of volcanoes, inherent instability is evidenced theoretically in the rapid segregation and shallow accumulation of rhyolitic melt [1, 2]. The interfacial instability is also commonplace inside a human body. In a various of pulmonary diseases, the small airway epithelium that coated by viscous liquid film is more prone to air-liquid two-phase instabilities due to the impaired capabilities of pulmonary surfactant[3, 4]. In industry, the interfacial instability is also observed; for example, the interface between solvent and polymer is unstable during coating process.

As one of the classical instability problems in fluid mechanics, viscous fingering refers to a fluid-fluid instability that takes places when a more viscous fluid is displaced by a less viscous one in porous media. In most but not all cases, the instability is associated with viscosity variations [5] and is observed in a wide range of processes. For example, a non-linear growth of a gravitationally driven unstable interface is observed in a Hele-Shaw cell, where larger fingers are reported to undergo further instabilities to form highly contorted interfaces [6]. Fingering instability is also reported when an arbitrary number of layers of immiscible fluid are involved [7]. Recently, it has been successfully proven that modulating channel properties [8, 9] or employing time-dependent injection strategies [10] is a powerful tool in manipulating viscous fingering. Alternatively, viscous fingering

*Part of this chapter is reprinted with permission from "Particle-induced viscous fingering'' by Feng Xu *et al*, 2016. Journal of Non-Newtonian Fluid Mechanics, Vol. 238, Pages 92-99, Copyright [2016] by Elsevier B.V. and from "Formation and Destabilization of the Particle Band on the Fluid-Fluid Interface'' by Jungchul Kim, Feng Xu and Sungyon Lee, 2017. Physical Review Letters, Vol. 118, Pages 074501, Copyright [2017] by American Physical Society.

can also be modified by changing the fluid phases themselves. For instance, incorporating non-Newtonian fluids, such as shear-thinning [11, 12] and Boger [13] fluids, has shown to change the resultant fingering behaviors compared to their Newtonian counterpart. It remains an actively explored area due to its relevance to geophysical flows and other various phenomena, such as ribbing instability [14], balcony growth [15], dendritic growth [16], and flame propagation[17].

The inclusion of particles in the fluid can bring modifications or even completely change the fingering instability. Particles absorb and assemble into a dense monolayer via capillary attractions and rigidify interfaces against interfacial instability [18]. The stabilizing effects of adsorbed particles on the interface have led to a number of technological advances, from stabilizing emulsions [19] to forming "liquid marble"[20]. More recently, the wettability of particles was utilized to control viscous fingering, as Trojer and colleagues [21] suppressed viscous fingering by injecting air into a saturated packing of hydrophobic particles. In the reverse scenario, oil injection into a channel containing hydrophilic particles was shown to induce viscous fingering [22].

The literature listed above indicate that particles play an important role in interfacial instabilities. It is clear that a thorough understanding of the effect of particles is necessary in understanding many natural and industrial processes. In this dissertation, particles entrained in a fluid flow is investigated, namely, a suspension flow consisting of neutrally buoyant particles and highly viscous fluid.

1.2 Suspension Flow and Particle Migration

The applications of suspension are common in various areas, for instance, the formation of delta, the systematic circulation, food or petroleum industry. Particles contained in such suspension flows experience a variety of forces, including both inertial and viscous effect. However, in the case of highly viscous suspension, inertial effect is likely negli-

gible given that the dimensionless Reynolds Number defined as ratio of inertial force to viscous force, $Re = \rho u L/\mu$, is small. Here, ρ, u, L, μ refer to density of carrying fluid, flow velocity, characteristic length of flow geometry and fluid viscosity respectively. In such systems, particles tend to migrate from high to low shear region, which in turns leads to a variation/gradient in local volume fraction of particles ϕ as well as effective viscosity η_r of bulk suspension.

According to theories proposed in the early 20th century, the mono-disperse suspension is expected to behave as an incompressible, isotropic Newtonian fluid in the absence of non-hydrodynamic effects like Brownian force, van der Waals interactions etc [23, 24]. In other words, the effective viscosity is believed to be a constant scalar given that the stress is a linear function of rate of strain. However, the experimental measurements reported by Hoffman [25] and Gadala-Maria [24] clearly indicate the existence of an anisotropic structure of particles in mono-disperse suspensions, with or without the above mentioned non-hydrodynamic effects, respectively. Those research suggested that a scalar η_r is no longer sufficient to describe the relation between stress and rate of strain, which are among the earliest evidence of the migration of particles away from high to low shear region. In a follow-up study, David Leighton and Andreas Acrivos successfully demonstrated that the decrease in the suspension viscosity reported in [24] is due to the shear-induced migration of particle out of the sheared Couette gap, which arises from irreversible inter-particle interactions [26].

The shear-induced migration is later evidenced by more observations, both experimentally and theoretically. Abbott and colleagues [27] measured the evolution of radial concentration and velocity profiles of an initially well-mixed suspension undergoing a Couette flow between rotating concentric cylinders. They reported that particles migrate from the high shear region near the inner rotating cylinder to the low shear region at the outer wall. The particle concentration at the outer wall goes up to as high as maximum packing for

randomly distributed spheres at steady state. As a result of the shear-induced migration, they also observe the formation of concentric two-dimensional, circular sheets of particles extending inward from the outer wall. Corbett [28] later reported similar shear-induced migration for a 40% volume fraction of polymethyl methacrylate (PMMA) spheres in polyalkylene glycol (PG) in a concentric cylindrical Couette device. They extended the experiments by introducing a different flow geometry: the coaxial cylinders in which a straight flight rotates with the the inner cylinder and spans the annulus between the surfaces. It is reported that the concentration gradient is not exhibited, which indicates the importance of mixing in a classic Couette device.

Efforts are also made experimentally on measuring the migration of particles in different geometries apart from Couette set-ups. Altobelli *et al* [29] measured the concentration and velocity profile of small, negatively-buoyant particles traveling in a horizontal tube with an initial concentration ranging from 0% up to 39% and velocity up to $25cm/s$. a non-uniform particle distribution as well as a "blunted" velocity profile are reported. It is worth mentioning that the observation of the blunted velocity in the circular conduit geometry can date back to as early as 1960s by Karnis & Mason [30] and later is attributed to particles undergoing shear-induced migration by Chapman [31]. Hampton *et al* [32] carried out rigorous experiments with particle concentrations varying between 10% to 45% in a circular tube, picking the ratio of tube to particle 16 and 39. They reported that the velocity profile is parabolic and particle distribution being uniform with ϕ under 10%. But for those experiments with $\phi \leq 20\%$, both blunted velocity profile and non-uniform particle distribution are observed. Koh *et al* [33] utilized the adapted laser-Doppler anemometry (LDA) technique to study concentrated suspension flows with ϕ up to 30% inside a rectangular channel, where they found that the velocity profile is blunted while the the concentration profile reaches an maximum near the center. Another significant observation they have is the velocity profile become more blunted with the increase

in either the particle concentration or the relative ratio between particle size to channel dimension. Lyon & Leal [34] utilized laser-Doppler velocimetry (LDV) to measure the fully developed particle velocity and concentration profiles for suspension of ϕ up tp 50% migrating across a rectangular channel. They reported that the particle concentration reaches a maximum near the channel centerline and is a minimum near the channel walls, which are also coupled with blunted velocity profiles.

More recently, some researchers have focused on the particle-laden thin-film flows down an incline [35, 36]. Zhou *et al* [37] conducted experiments with glass beads suspension flowing down an incline by varying either the bulk concentration ϕ or the inclination angle α. They reported three different regimes with different combinations of ϕ and α: when both parameters are small, a clear liquid front is formed with a distinct front of settled particle following behind; when both parameters are large, a large particle-rich ridge forms at the advancing front, which may grow to several times the thickness of trailing film; for intermediate ϕ and α, the suspension remain well-mixed throughout the experiment. Murisic *et al* [38] looked in more detail into the settled regime corresponding to the above mentioned small ϕ and α. They derived a rigorous dynamic model and found quite good agreement between experimental observations and theoretical predictions.

The experimental works are not restricted to mono-disperse particle suspensions, where only a single size of particle is mixed with carrying fluid to form the suspension. It is also shown that the behavior of particles in a bimodal suspension system share similarities with its mono-disperse counter part which contains single species of particle in the low-Reynolds-number range, in that particles migrate from high to low shear regions regardless of the particle size [39, 40, 41]. However, it is also observed that, in bi-disperse suspensions, there exist an enrichment of concentration in large particles relative to their average concentration in suspension. Graham *et al* [40] employed the nuclear magnetic resonance (NMR) imaging to study the migration of concentrated suspensions undergo-

ing flow between rotating concentric cylinders. They confirmed the migration of particles from high to low shear region and more importantly, they reported that large particles in bimodal suspension form concentric cylindrical sheets, which, to the author's knowledge, provided the first insight into the effects of polydispersity on particle migration in suspension. Husband and colleagues [41] measured the particle migration in suspensions of bimodal spheres and confirmed that suspended particles migrate from regions of high shear rate to regions of low shear rate. They also reported in the same paper that coarse fraction of particles migrates much faster than the fine fraction, which lead to size segregation of initially well-mixed suspensions. Built on those studies, Lyon and Leal [42] designed detailed experiments to report the velocity and concentration profiles for suspensions of bi-disperse distributed particles undergoing a pressure-driven flow through a parallel-wall channel. More recently, Norman *et al* [43] reported the size segregation of bi-disperse suspensions in pressure-driven pipe flows taking into account of the negative buoyancy of particles. Finally, there are other types of research that focus on the migration and concentration distributions of colloidal bi-disperse suspension systems [44, 45], which is beyond the scope of this project.

Several theoretical models have been developed in the past to validate experimental results, by calculating both the concentration and the velocity profiles for two-dimensional suspension flow in confined geometries. There are in general two approaches, and both have been proven to be successful in comparison to experimental results. The first method is the so-called diffusive flux model which is originally proposed by Leighton & Acrivos [26] to explain their experimental observations [46]. The model is intuitively straightforward since it is based on the kinematics of particle interaction: when a particle experiencing simple shear flow is to interact with another particle, it is expected to be displaced in the same direction as the other particle approaching. The microscopic reversibility normally expected for Stokes flows is broken due to the non-hydrodynamic interaction via

surface roughness [26, 47]. Thus a gradient of particle interaction is expected if there exist a gradient in either shear or particle concentration across streamline, which in turns lead to a migration of particles across streamline. Thus the proposed flux constitutive equation is given as

$$D = -K_\sigma \frac{\phi^2}{\tau}\frac{\partial \tau}{\partial y}\dot{\gamma}a^2 - K_{||}\frac{\phi^2}{\mu}\frac{\partial \mu}{\partial \phi}\frac{\partial \phi}{\partial y}\dot{\gamma}a^2 \tag{1.1}$$

where $-K_\sigma$ and $K_{||}$ are constants to be determined empirically, ϕ is the concentration, τ is the shear stress, $\dot{\gamma}$ is the shear rate, μ is the viscosity and a is the particle diameter.

The model is then extended by Phillips *et al* [48] to more general 2-D suspension flow, leading to the following flux constitutive equation

$$D = -K_c a^2(\phi^2 \nabla\dot{\gamma} + \dot{\gamma}\phi\nabla\phi) - K_\eta \frac{\phi^2}{\mu}\frac{\partial \mu}{\partial \phi}\dot{\gamma}a^2\nabla\phi \tag{1.2}$$

with the same definition of parameters as in Eq. 1.1.

Later the model is further developed by Krishnan *et al* [49] to account for the particle flux brought by the streamline curvature, enabling the model to explain the lack of migration of particles in parallel-plate flow where there exists an outward growing shear rate [31]. Inheriting the notation from [48], the fully developed concentration profile for two-dimensional channel flow can be iteratively solved with

$$\phi(z) = \phi_m[1 - \frac{\phi_m z}{k(1-\frac{\phi}{\phi_m})^{\chi-1} + \phi_m z}] \tag{1.3}$$

where z refers to the spatial variable across the gap of channel, ϕ_m is the concentration where viscosity diverges to infinity and χ is a measure of the relative magnitudes of the flux of particles resulting from gradient in particle concentration and the flux of particles through the channel cross-section.

The flux model has been widely applied ever since it is proposed. Zhang and col-

leagues extended the original unidirectional model to cases where they consider all three velocity components to capture the resuspension of heavy particles traveling in fully developed laminar flow in a horizontal pipe. Their predictions are reported to be in very good agreement with existing experimental observations [50]. Shauly and colleagues [51] studies the effect of particle radii on shear-induced migration in Couette flow by constructing a phenomenological model. Notably, they have built models for both discrete and continuous radii of particle and found qualitatively well agreement with existing experimental results. More recently, Murisic *et al* developed a diffusive flux model to study the migration of thin-film particle-laden flow down an incline with very satisfactory agreement between their experiments and numerical calculation [36, 38]. Lee *et al* have successfully applied the model on particle-laden flow in a spiral geometry [35].

Another widely used continuum model is called the suspension balance model (SBM), which was originally developed by Nott & Brady [52] to study pressure-driven suspension flows. Different from the diffusive flux model, the SBM accounts for a non-Newtonian bulk stress with normal stresses induced by shear, and the particle migration is a direct result of the normal stress gradient. Rather than being purely a function of particle concentration ϕ, viscosity is treated in such a way that it also contributes to normal stresses, whereas this viscously generated stress is omitted in the aforementioned flux model. The governing equation for SBM is given by the conservation of momentum,

$$\nabla \cdot \Pi = 0 \tag{1.4}$$

where the stress is a summation of stresses due to the particle interaction, hydrodynamic pressure and viscosity. Due to its effectiveness in describing viscoelastic characteristics of the mixture in a non-dilute limit, the suspension balance model will be employed in the current analysis. A more detailed description as well as equation derivation will be

provided in later chapters.

The SBM has many successful applications in predicting the velocity and concentration profiles of suspension flow in different flow geometries. Morris & Brady [53] applied the model to study curvilinear flow and predicted different behaviors of negatively buoyant particles with an uniform initial distribution via simulation. Morris & Boulay [54] later performed a similar simulation on curvilinear flows. Lyon & Leal [34, 42] utilized the model to verify experimental observations and found good agreement at particle concentrations up to 50%: both the enrichment of particles near the channel centerline and the bluntness in velocity profile are well captured. Norman *et al* [55, 43] made use of the model to predict the migration of negatively buoyant particle through a pipe flow and modified the original model to account for the polydispersity of particles utilized in experiments in the same geometry. His numerical predictions show good agreement with experimental observations. Ramachandran *et al* [56, 57] applied the SBM on the squeeze flow between two parallel plates and successfully captured the outwards migration of particle towards the interface.

There also exists a newly proposed method called frictional suspension rheology that addresses the transition of suspension to granular media [58, 59, 60]. Both the diffusive flux model and the suspension balance model are expected to fail when the particle volume fraction is large, say, approaching the maximum packing value of 0.62. In such transition regimes from suspension to granular flow, the rheology is said to be completely determined by two functions of the inertial number *I*: a friction law for shear stress $\tau = \mu(I)P^p$ and a volume-fraction law $\phi(I)$. The inertial number is defined as $I = d\sqrt{\rho_p/P^p\dot{\gamma}}$ which is basically the ratio of the fluid shear stress and the particulate normal stress, where *d,* ρ_p*,* P^p and $\dot{\gamma}$ are the particle diameter, particle density, confining pressure and shear rate respectively [58]. Lecampion & Garagash investigated the model by applying it to the problem of confined pressure-driven laminar flow of neutrally buoyant non-Brownian suspensions.

They reported an excellent agreement between their numerical calculation and existing experimental data, which shows the great potential of unifying the theories of suspension flow and granular flow [61].

Compared to the rich literature of theoretical modeling of mono-dispersed suspension, there is a significant lack of similar theoretical work of bi-dispersed or poly-dispersed suspensions. However, the aforementioned methods can be modified to accommodate the bi-dispersed suspension systems. For example, Shauly and colleagues [51] studied the effect of particle radii on shear-induced migration in Couette flow by constructing a phenomenological model. Norman *et al* [43] modified the suspension balance model by adding a constitutive stress equation for a second species of particle to calculate the respective concentration profile of both types of particles. Some simulation works [62, 63] employ Stokesian dynamics to measure self-diffusion and viscosity of the neutrally buoyant suspensions of bi-disperse particles, in which the number of particles involved in the simulation are extremely limited due to the complex nature of particle-particle interactions. There is yet no reported attempts to apply the frictional rheology on suspensions containing more than one species of particles to the best knowledge of the author. For the sake of consistency, we follow the successful application of the modified suspension balance model for bi-disperse suspensions by Norman [55] and model our systems in a similar manner.

In parallel to experimental and theoretical work, the existence of pure simulation can not be ignored. Numerical simulation provides an alternative method to study the particle-fluid interaction under complex conditions, especially when it becomes difficult to carry out rigorous experimental measurements. One of those methods employs the phase-resolving model. For example, Hu *et al* [64] developed an finite element method to simulate the motion of large numbers of rigid particles in either 2-D or 3-D in Newtonian fluid. Patankar *et al* [65] later on modified the formulation and proposed a new

Lagrange-multiplier-based fictitious-domain method(DLM). Later on Apte [66] developed an approach under the same discipline with the finite difference method. On the other hand, compared to the amount of available literature research, the collision model application is not as diverse. For example, Glowinski *et al* [67] developed a repulsive potential (RP) model that prevents particles from overlapping by applying a repulsive force at some small distance before the particles come in contact. The method is then employed by researchers [68, 69] to simulate particle-laden flows but only restricted to small volume fraction. Biegert *et al* [70] carried out direct numerical simulations based on the model proposed by Kempe [71] to study the motion of particles with dense packing fractions. In their study, it is worth mentioning that they run the simulation on poly-disperse particles, which is among one of very few simulation works available in literature.

1.3 Motivation and Objective

In this project, we focus on the viscous fingering instability that is specifically *induced* by the inclusion of non-colloidal particles in the displacing liquid. Given the prevalence of suspension flows in geophysical systems, such as avalanches, as well as in industry that ranges from nanotribology to hydraulic fracturing, the study of interfacial instabilities in the presence of particles represents an exciting and relatively unexplored area of research.

Tang *et al.* [72] first observed an unexpected interfacial instability when a mixture of non-colloidal particles and viscous fluid displaces air in a Hele-Shaw cell. Then, they qualitatively correlated the particle volume fraction, ϕ_0, to the instability growth rate. It is noteworthy that the same flow without particles is inherently stable. More recently, Ramachandran & Leighton [56] observed the analogous fingering instability upon squeezing a particle-oil mixture between two parallel plates. To the best knowledge of the author, these are the only existing works that deal with the fingering instability induced by the introduction of particles. Based on this, we carry out rigorous experimental and theoretical

research considering both mono-disperse and bi-disperse suspensions flow in a rectangular Hele-Shaw cell. We aim to identify the mechanism that drives the instability and to provide theoretical validation to experimental observations.

In the mono-disperse case, though Tang [72] and Ramachandran [56] respectively reported the experimental observation and qualitative justification of the particle-induced viscous fingering, no thorough quantitative experimental and theoretical investigation of this phenomenon have been given to establish the connection between the interfacial instability and particle transport. In the present work, we propose to experimentally quantify the aforementioned particle-induced viscous fingering by injecting suspensions of varying ϕ_0 into a Hele-Shaw cell with varying gap thicknesses. We observe the particle accretion and identify the critical particle volume fraction at which the viscous fingering initiates. Image processing techniques will be employed to measure the particle concentration as well as the extent of interfacial deformations. In parallel to experiments, we theoretically confirm the effects of shear-induced migration far upstream of the interface based on the suspension balance method, in good agreement with the experimental data.

In contrast to mono-disperse suspensions, the viscous fingering induced by particles as well as the dynamics lying behind for bi-disperse suspension flow remain completely unexplored. In this work, careful experiments are carried out by either systematically varying the ratio of large to small particles at fixed total concentrations, or by changing the total concentrations for constant large particle concentrations. We observe the instability and its dependence on the presence of large particles compared to the pure small particle case. We will make use of image processing and machine learning technologies to identify the respective concentration profiles of each species of particle in experiments. The aforementioned suspension balance model is modified to provide validation for our experimental observations.

1.4 Data Acquisition and Processing Technologies

The primary technologies noticed so far in literature fall mainly into three categories: the Nuclear Magnetic Resonance (NMR), the Laser-Dopler Velocimetry (PLV) and the electrical impedance tomography (EIT) imaging.

The foundation for NMR imaging is the combination of an applied magnetic field gradient and a static magnetic field. The variation in the so-called Larmor frequency makes it possible to image spin density, hence the particle distribution as a result of the magnetic field gradient. Compared to techniques based on sound waves [73] or particle beam, which may suffer signal attenuation, the noninvasive NMR imaging show a great advantage in analyzing particle distribution in two-dimensional flows [40]. The NMR technology has been successfully applied in measuring the particle concentration profiles in various flow geometries, such as concentric cylindrical Couette flow [27, 28], tube flow [29, 32] and rectangular channel flow. However, limited by its complex and expensive nature, NMR is not very widely used.

The LDV technique is also among those noninvasive methods in measuring particle distribution, which incorporates the index-of refraction matching of the suspending and particulate phases. A great advantage of LDV is its high spatial resolution, which makes it even possible to measure the velocity of every particle passing the probing volume. Successful application of LDV can be found in [34, 42, 33].

The EIT imaging technique is based on the fact that different materials have different impedance. By introducing a current passing through a series of electrodes, a potential field is produced corresponding to the conductivity distribution inside the test section. The potential field is then used to reproduce the conductivity field, which is subsequently mapped to particle distribution profiles via correlation [55].

1.5 Outline

The remainder of this dissertation is organized as follows. In Chapter 2, a detailed description of the experimental setup is provided, including both the individual components and the flow system as a whole. We will also give details about the data processing techniques, such as the edge detection and artificial neural network that are used throughout the research. The mathematical foundation of those techniques will be reviewed for the sake of completeness.

In Chapter 3, we will focus on the migration of particles in a mono-disperse suspension inside the rectangular Hele-Shaw cell. Experimental observations are listed in detail, followed by our analysis. A detailed description of the suspension balance model is provided, in the context of model development and derivation. We will present our numerical calculation results, which will be compared with our experimental observations for validation. A brief conclusion of the mono-disperse suspension project will come at the end of Chapter 3.

In Chapter 4, the focus will be the migration of particles in bi-disperse suspensions. Key observations from experiments are presented first, accompanied by our analysis. A modified suspension balance model is employed to describe the bi-disperse suspensions and explained in the following section. We show the numerical results by solving the model and compare the results with experiments. The chapter concludes with a brief summary.

In the last chapter, an overall conclusion for the whole research is given. We will also elaborate on the contribution of the author's work to science. Future work will also be discussed, in hopes of providing the vision and direction for continued research.

2. EXPERIMENTAL SETUP AND DATA ANALYSIS METHODS*

2.1 Experimental Setup

In this research, the Hele-Shaw cell is constructed from two piece of plexi-glass (acrylic) plates (30.5 $\times$ 30.5 $\times$ 3.8 cm). The plates are specifically chosen at a thickness larger than 2.5cm (1 inch) to avoid possible bending effects. The plates are leveled and separated to a gap thickness h. The gap separation is controlled by securing shims (McMaster) of different sizes (will be provided in later chapters) at the four corners of the plates. According to the definition of capillary length shown in Eq. 2.1, which characterizes the relative relationship of Laplace pressure and hydrodynamic pressure [74], the characteristic length scale is roughly estimated as 1.5mm. Thus the shim are chosen to be thinner than the capillary length so that all experiments can be considered in the range of low Bond number, where surface tension dominates over gravity. In the equation, γ and ρ refer to the surface tension and density of fluid (silicone oil in this research) respectively, g is the gravitational acceleration.

$$\lambda_c = \sqrt{\frac{\gamma}{\rho g}} \tag{2.1}$$

A through hole is drilled at each corner of the two pieces of plates, so that the glass plates can be locked rigidly using long bolts. We also drill a through hole at the center of bottom plate, which serves as the source of suspension supplement. The Hele-Shaw cell is then placed and locked onto a frame built from standard $80/20$ ($80/20$ Inc.) parts. The frame is specifically designed so that an LED panel (EnvirOasis, 75W, 4200 Lumen) can be placed under the cell to provide uniform illumination and a digital camera (Canon 60D, 1920x1080 pixel images, FOV 64^{o}) is secured directly above the cell to record all

*Part of this chapter is reprinted with permission from "Particle-induced viscous fingering'' by Feng Xu *et al*, 2016. Journal of Non-Newtonian Fluid Mechanics, Vol. 238, Pages 92-99, Copyright [2016] by Elsevier B.V..

experiments at 30 frames per second.

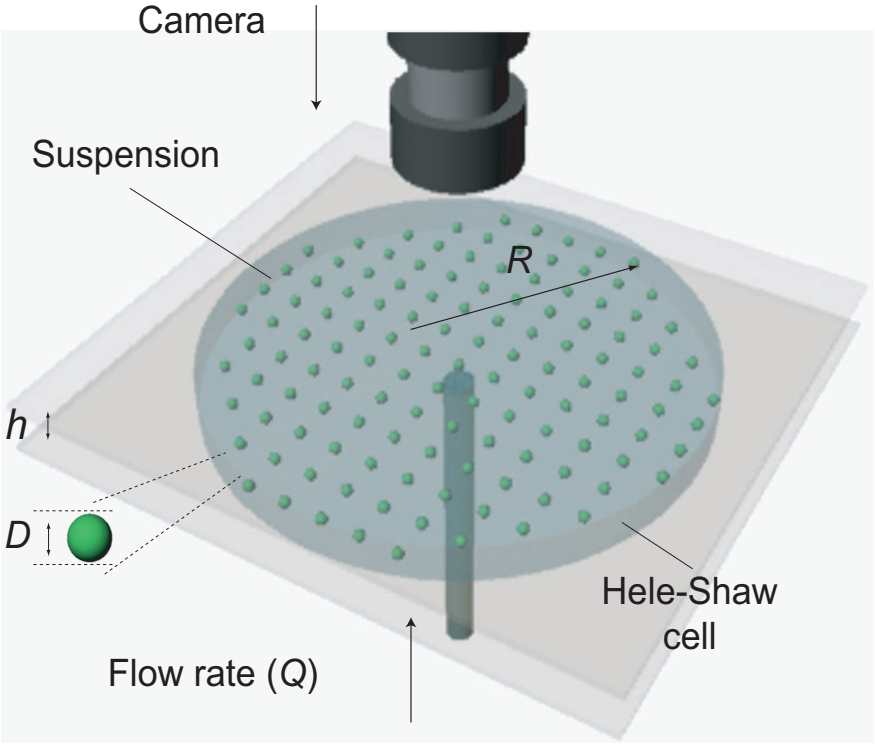

Figure 2.1: Schematic of the experimental setup: suspensions are injected into the Hele-Shaw cell from the center hole, and experimental observations are recorded with the camera from above.

The particles used in this research are fluorescent polyethylene green or red particles purchased from Cospheric. They are carefully chosen to stay in a safe range where the Brownian motion is negligible, with diameters of $D = 125 - 150\mu m$ and $D = 300 - 355\mu m$ respectively. The carrying fluid is chosen as PMMS silicone oil from UCT. The oil has a density of $\rho_l = 0.96$ g/cm^3 and viscosity of $\eta_l = 0.096$ Pa·s. The contact angle of oil on the plexi-glass plate is measured to be smaller than 1°, which means the silicone oil wets the plate surface completely. In the preparation of suspension, the particles are weighed carefully and then mixed with a given volume of oil to secure a precise particle

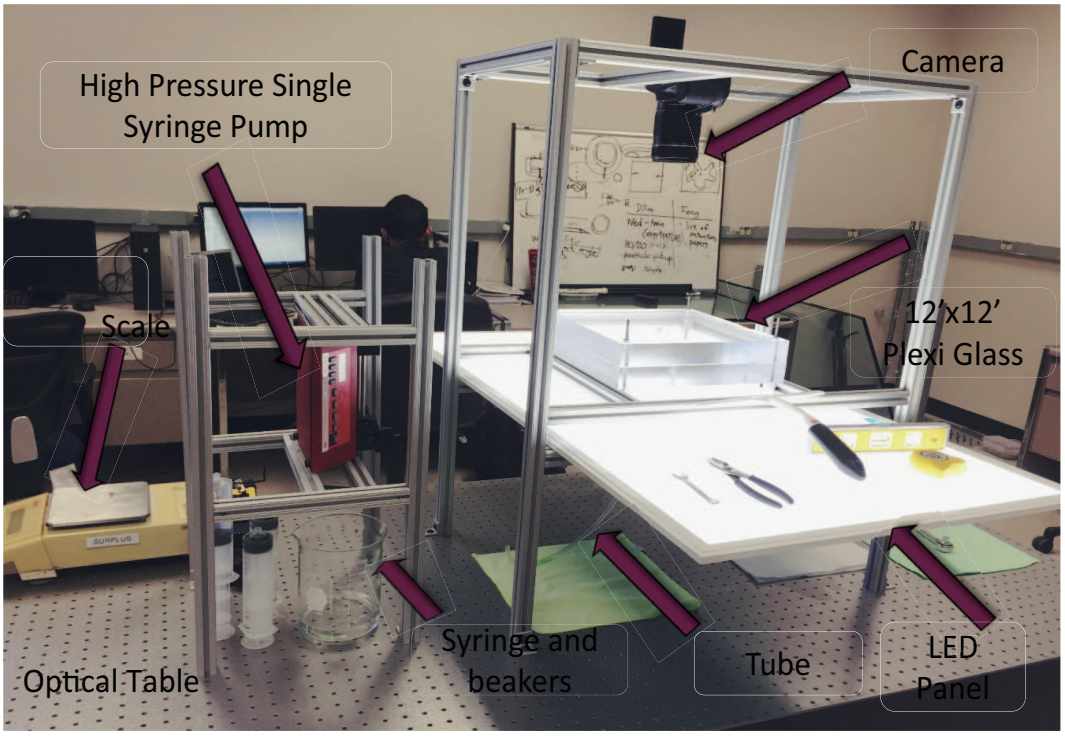

Figure 2.2: The experimental setup, with each key component labeled. The main test section is the Hele-Shaw cell secured by the frame, with an LED panel lying underneath providing uniform background and a digital camera recording experiments from top-down view. The suspension is prepared using beakers and syringes, and then injected into the cell via a tube using a syringe pump. The whole setup is secured on an optical table for seek of stableness.

volume fraction. The mixed suspension is then loaded into a syringe with a capacity of 140 mL, which is left still to get rid of any air bubble trapped inside. We use a syringe pump from New Era to pump the suspension into the Hele-Shaw cell through a tube. The pump is capable of providing flow rates that range from $95.37\mu L/hr$ to $208.3mL/min$ with a 140mL capacity syringe. The typical flow rate used in this research is 150mL/min. The whole setup is secured onto an optical table from New Port. A schematic of the test section and a picture of the whole experimental setup are shown respectively in the following figures.

2.2 Data Analysis Techniques: Image Processing

A very large portion of data analysis in this research falls into image processing. There are two major challenges encountered in processing our experimental data: a clean edge detection and particle concentration profiles estimation. The concentration profile calculation becomes especially difficult for bi-disperse suspensions, given that the particles of different colors and diameters are so mixed up. An artificial neural network (ANN) is thus designed to classify different particles, aiding the calculation of the concentrated profiles.

2.2.1 Edge detection

It is essential to acquire structural/segmental features like edges from images prior to detailed analysis. Edge detection continues to be an active research area due to its importance, especially in the sense that it is usually among one of the earliest steps to recover desired information from images. Indicating a significant local change in images, edges typically occur on the boundary between two different regions. More specifically speaking, the edges in an image correspond to significant local changes in intensity, which in most cases are associated with either a discontinuity in local intensity value or the first derivative of intensity. In this section, we will discuss briefly some basic concepts and the mathematical background of the edge detection.

As mentioned above, edges are basically discontinuities in images. The discontinuity falls into two categories: (1) *step discontinuity*, where the value of intensity on one side of the edge changes abruptly to a different value and remains; (2) *line discontinuity*, where the value of intensity on one side of the edge changes to a different value and returns to the initial value after some short distance[75]. In real images, neither step nor line discontinuity is often observed due to the smoothing technologies introduced by sensing devices. Instead, what is mostly observed as a substitute is *ramp discontinuity* (corresponding to step discontinuity) and *roof discontinuity* (corresponding to line discontinuity). What is

also commonly observed in real images is a combination of both. It is worth mentioning that noise is almost impossible to avoid, which makes it even more common to observe the above mentioned combination, and indefinitely makes it harder to obtain a clean edge. We will hereby introduces some concepts and mathematical symbols for further reference in the remainder of the section (Please also refer to [76] for original definitions if interested).

Definition 2.1. An edge point is a point in an image with coordinates $[i, j]$ at the location of a significant local intensity change in the image.

Definition 2.2. An edge fragment corresponds to the i and j coordinates of an edge and the edge orientation θ, which may be the gradient angle.

It makes sense in general to consider an image as a series of some continuous function of intensity values. Thus a significant change in intensity in an image can be expressed in terms of the gradient of the function, which in two-dimensional images is given as:

$$G[f(x,y)] = \begin{bmatrix} G_x \\ G_y \end{bmatrix} = \begin{bmatrix} \frac{\partial f}{\partial x} \\ \frac{\partial f}{\partial y} \end{bmatrix} \tag{2.2}$$

where $f(x, y)$ represents the function that describes the intensity distribution. It is noteworthy that the gradient $G[f(x, y)]$ points in the direction of the maximum of rate of increase of the function $f(x, y)$. The magnitude of the gradient is hence given as:

$$|G[f(x,y)]| = \sqrt{G_x^2 + G_y^2} \tag{2.3}$$

In reality or algorithm development, the gradient is however approximated by,

$$G[f(x,y)] \approx |G_x| + |G_y| \tag{2.4}$$

In practice, the gradient vector is actually approached numerically by considering the differences in absolute intensity values in a digital image, which mathematically can be expressed as,

$$G_x \cong f[i, j+1] - f[i, j] \tag{2.5}$$

$$G_y \cong f[i, j] - f[i+1, j] \tag{2.6}$$

This can be easily implemented using convolution masks. For example, the above Eqs. 2.5 and 2.6 can be performed with the help of the masks shown in Table 2.1,

-1	1

1
-1

Table 2.1: Example of one-dimensional mask used to perform intensity gradient numerically.

Different edge detection operators have been developed in the past few decades, for instance, the Robert operator makes use of two 2×2 masks while the Sobel operator and Pewitt operator perform the convolution with 3×3 masks.

So far we have talked about the edge detectors that compute the first derivatives of intensity values, where an edge is marked whenever the magnitude is above a chosen threshold. Those detectors can be problematic in the sense of detecting too many edge points. For example, the detected edge is likely to be much thicker than it actually is. A better solution is to look for the points having local gradient maxims, which in other words means that a peak is expected in the first derivatives at edge points. It is also equivalent to try to find the zero crossings in the second derivatives.

A very commonly used second derivative operator is the Laplacian, which takes the

form of,

$$\nabla^2 f = \frac{\partial^2 f}{\partial x^2} + \frac{\partial^2 f}{\partial y^2} \tag{2.7}$$

The second derivatives along the x and y direction are approximated numerically as follows,

$$\frac{\partial^2 f}{\partial x^2} = f[i, j+1] - 2f[i, j] + f[i, j-1] \tag{2.8}$$

$$\frac{\partial^2 f}{\partial y^2} = f[i+1, j] - 2f[i, j] + f[i-1, j] \tag{2.9}$$

Again we notice that the numerical approximation can be achieved with the help of convolution masks. The Laplacian marks a point as 'on the edge' when it detects a zero crossing, where trivial zeros (corresponding to uniform intensity regions) are omitted. The Laplacian operator is not frequently used however, given that it is more sensitive to noise in nature than first derivative operator. To avoid the influence of noise while still maintaining the advantages of running second derivative, we introduce a powerful filter, the Gaussian filter.

The Laplacian of Gaussian (LoG) [76] combines the Gaussian filter with the Laplacian operator. In this methods, the Gaussian filter plays the role of smoothing the image by filtering out isolated noise points and small structures while the edge points are signaled upon the detection of zero crossings in second derivatives. To make sure the method detects only the significant edges, a signal is given only if the first derivatives corresponding to zero crossings are above a pre-selected threshold. Mathematically, this can be expressed as:

$$h(x, y) = \nabla^2[(g(x, y) * f(x, y))] = [\nabla^2 g(x, y)] * f(x, y) \tag{2.10}$$

where,

$$\nabla^2 g(x, y) = (\frac{x^2 + y^2 - 2\sigma^2}{\sigma^4}) e^{-\frac{x^2+y^2}{2\sigma^2}} \tag{2.11}$$

In the equations above, the parameter σ is playing an important role in the method. It controls how much blurriness is brought to the actual edges as well as to other significant discontinuities. There exists a trade-off between noise reduction and maintaining edge information, being that larger value of σ results in the dislocation of edges or even false edges while smaller σ values leads to more noise as a result of insufficient averaging.

Due to the existence of the trade-off mentioned above, we want to find an operator that provides the best compromise between noise suppression and edge localization, while still being able to maintain the advantages of Gaussian filtering. The operator turns out to be the first derivative of Gaussian, which is used to construct the *Canny edge detector*. Given the fact that the operator is symmetric along the edge, it is very sensitive to the edge in the direction of steepest change. It is, however, insensitive in the direction of antisymmetric perpendicular to edge and provides smoothing effects.

Given an image represented by $I[i, j]$, the intensity matrix is smoothed by running convolution with a Gaussian filter, which gives,

$$S[i, j] = G[i, j; \sigma] * I[i, j] \tag{2.12}$$

The gradients of the smoothed matrix $S[i, j]$ is then computed numerically by performing finite difference operation on both x and y directions (convolution masks),

$$P[i, j] \approx (S[i, j + 1] - S[i, j] + S[i + 1, j + 1] - S[i + 1, j])/2 \tag{2.13}$$

$$Q[i, j] \approx (S[i, j] - S[i + 1, j] + S[i, j + 1] - S[i + 1, j + 1])/2 \tag{2.14}$$

Both gradients in x and y directions are then used to calculate the magnitude matrix,

$$M[i, j] = \sqrt{P[i, j]^2 + Q[i, j]^2} \tag{2.15}$$

Edges are eventually detected by performing the nonmaxima suppression, which finds the local maxima in the magnitude matrix. It is common practice to apply a threshold to reduce $M[i, j]$, where all values in M smaller than the threshold are turned to zero. This helps to reduce the amount of false edges detected. Applying only one threshold can be problematic however, considering that false edges are signaled if the threshold is set too low or portions of edge will be missing if the threshold is selected too high.

A more effective thresholding strategy applies two thresholds, or in other words, a threshold vector $[\tau_1, \tau_2]$ with $\tau_2 > \tau_1$. By implementing two thresholds, the algorithm is able to construct two different edge images T_1 and T_2. The algorithm finds all edges in T_2 first, which contains fewer false edges. It then searches for edges in T_1 that are able to bridge to the edge contour constructed from edges detected in T_2. This way the performance is improved compared to the single-threshold strategy.

In this research, the *Canny edge detector* is implemented to find edges in the images obtained from our experiments. We vary both the smoothing controller σ and threshold vector $[\tau_1, \tau_2]$ to achieve best performance in finding clean edges.

2.2.2 Median filter

It turns out that the *Canny* detector does not provide satisfactory processing results, mainly because the images from experiments are too noisy to be smoothed out enough by the Gaussian filter no matter how we adjust σ or vector $[\tau_1, \tau_2]$. We need to run a bit more noise suppression or noise cleaning before feed the images to the detector. There are some established filtering methods, for example, the linear noise cleaning in either spatial or Fourier domain, the Homomorphic Filtering technique etc [77]. In this research, we make use of a non-linear noise reduction method called the *median filter*, which is developed by Tukey [78].

The median filter takes different forms in different dimensions. For a one-dimensional

filter, it consists of a sliding window encompassing an odd number of pixels. The way the filter works is it replaces the intensity value of center pixel by the median of all pixel intensity values inside the window. Similar to the Gaussian filter mentioned in previous section, there also exists a trade-off between noise reduction and resolution loss for median filter. Various strategies may apply when implementing a median filter. One may begin with a window length of 3 and continuously increase the window length (note, should all be *odd* numbers) until a significant loss is observed or one judges that the filter is doing more harm than good.

The median filter can be easily extended to two-dimensional, where one replaces the window with a two-dimensional one having a desired shape. The shape of window depends on the application, it can take the shape of rectangular or discrete approximation to a circle. Similar strategies are inherited to decide the desired size of the window by starting small and change gradually till satisfactory smoothness is achieved. In this research, we find a median filter with a 3×3 rectangular window is good enough to reduce noise so that the performance of *Canny* detector improves significantly. The Fig. 2.3 shows an image example processed by *Canny* detector before median filtered. The noise points are removed in almost all cases once the images are smoothed out by the filter.

2.2.3 Calculation of concentration profile from intensities

The conversion from numerics from digital images to particle concentration has been studies and implemented in various research. Researchers are using either Hue in HSI (stands for *hue, saturation, intensity*) systems acquired from colored image [79] or the intensity value acquired from gray-scale images to approach the concentration profile [80, 81]. For example, Lim *et al* [81] assumes the concentration of particles is a third order polynomial function of intensity value and calibrate their experimental data to acquire a predictive model, which receives good agreement. In this research, rather than the

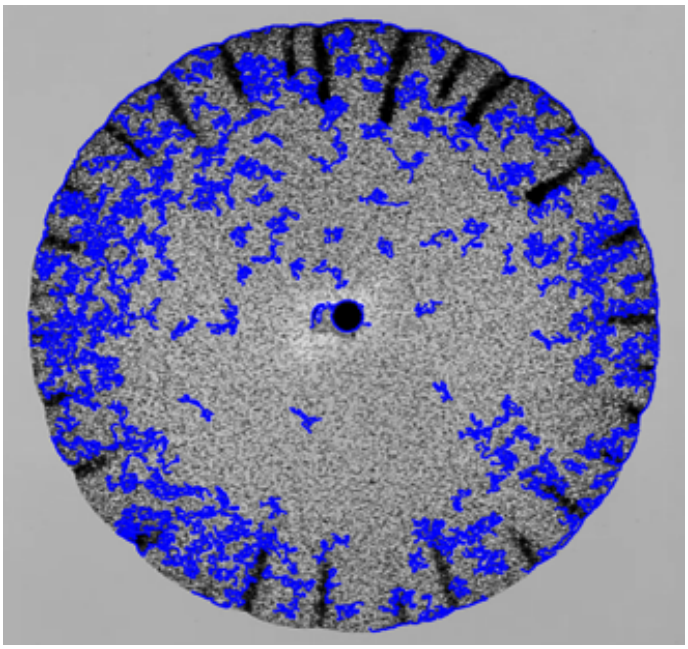

Figure 2.3: An example image that contain too much noise. The noise points will be removed if the image is smoothed out by a median filter before feed to the *Canny* edge detector.

polynomial fitting method, we employ a model which is less dependent on fitting parameter, as described in detail below.

To start with, the author would like to make it clear that we are correlating gray-scale intensity value I to concentration profile. Thus it is essential to convert the color images acquired from experiments to gray-scale ones. With that done, we then systematically subtract the background image prior to injection to eliminate any possible effect of non-uniformity in lighting on I. The relationship between I and the depth-averaged concentration $\bar{\phi}(r)$ in the radial direction is given as [82] :

$$k\frac{\log\frac{I(r)}{I_{\min}}}{\log\frac{I_{\max}}{I_{\min}}} = \bar{\phi}(r), \tag{2.16}$$

where, $I_{\min}$ and $I_{\max}$ are the minimum and maximum intensity values of a given image,

respectively. The empirical parameter, k, in Eq. (2.16) is obtained by integrating $\bar{\phi}(r)$ from the center to the fluid interface and satisfying mass conservation, such that

$$\int_0^R 2\pi\bar{\phi}rdr = \phi_0\pi R^2. \tag{2.17}$$

In order to discard the injection hole area, the lower limit of the integral in Eq. (2.17) is set to be a non-zero value, which is negligibly small compared to the characteristic radius R in experiments.

2.2.4 Artificial neural network and calculation of concentration in bi-disperse suspension

The image processing method utilized for mono-disperse suspension along with the code generated are inherited to analyze videos acquired from experiments with bi-disperse suspensions. This way, we will be able to estimate the bulk concentration profile in experiments ($\phi_{bulk} = \phi_{large} + \phi_{small}$). However, it is not enough to just being able to calculate the bulk concentration only. It's also desirable to acquire the respective local concentration information for each size of particle, i.e., ϕ_{large} and ϕ_{small}. The neural-networks algorithm is hereby applied to detect particles with different colors to provide help in calculating the concentrations of small and large particles.

Artificial neural networks (ANN) are inspired by animal brains, which is nothing more than a collection of huge amount of 'processors', or say, *neurons*. The part that makes brain really complicated and powerful is not just that it contains so many neurons ($\sim 10^{11}$), it is more about that every single neuron is connected via *synapses* to around 10^4 other neurons. The combination of absolute number of neurons and connections enables brain to function incredibly powerful with those neurons being able to process information in parallel. The kind of ANN utilized in this research, which is called *multi-layer perceptron* is an analogy to the brain. It learns (progressively improves performance) to do tasks by considering ex-

amples, generally without task-specific programming. For example, in image recognition, they might learn to identify images that contain cats by analyzing example images that have been manually labeled as "cat" or "no cat" and using the analytic results to identify cats in other images. They have found most use in applications difficult to express in a traditional computer algorithm using rule-based programming.

To start with, what is a perceptron? Simply speaking, perceptron is the most basic processing unit inside a network. It takes inputs which might be either from environment or the output of other perceptrons, denoted as $x_i, i = 1, 2, ..., d$. Each of the inputs is associated with a weight θ_i and in the simplest case, the output h is a weighted sum of all inputs:

$$h = \sum_{i=1}^{d} x_i \theta_i + \theta_0 \tag{2.18}$$

θ_0 is defined as a intercept value for the seek of generality. There is usually a bias input x_0 associated with θ_0, which always takes the value of $+1$. Thus Eq. 2.18 can be expressed in the form of vector dot product $h = \boldsymbol{x_i}\boldsymbol{\theta_i}$ with $\boldsymbol{x_i} = [1, x_1, x_2, ..., x_d]$ named the augmented input vector. According to the mathematical definition of a perceptron, it represents a line (if only one input available) or a (hyper)plane (if two or more inputs are provided), which divides the space into two. It thus can be used to perform classification as long as a threshold can be found.

The output doesn't necessarily have to be restricted to one. When there are $L > 2$ outputs, there are as a result K perceptrons, each of which are represented by,

$$h_i = \sum_{j=1}^{d} \theta_{ij} x_j + \theta_{i0} = \boldsymbol{\theta_i}\boldsymbol{x} \tag{2.19}$$

where θ_{ij} is the weight associated from input x_j to output h_i. In matrix form, Eq. 2.19 is expressed as $\boldsymbol{h} = \boldsymbol{\Theta}\boldsymbol{x}$ with $\boldsymbol{\Theta}$ defined as the $L \times (d + 1)$ weight matrix.

One should notice that the perceptron network we discuss so far is nothing more than the linear representation of inputs, with each percepton viewed as a local linear function of all inputs and associated weights. It however will be much more powerful if the perceptron network is able to represent non-linear model. Plus, though a single layer perceptron network expresses the boolean operations AND and OR well, it won't be able to solve problems like XOR, which really limits its application. The problem can be easily overcame by introducing a hidden layer, which lyes in-between the input and output layer. In such *multi-layer perceptron network*, inputs $\boldsymbol{x}$ are fed to the first layer, all units in the second layer are perceptrons of inputs, whose values are then fed to the perceptrons in output layer. For a perceptron labeled $\boldsymbol{j}$, there are following components linked with it:

- An activation a_j received from its predecessor perceptron;
- An output function g that computes the output from activation, which is provided to successor perceptron: $o_j = g(a_j)$

To empower the network the ability of representing non-linear model, the outputs of perceptrons in the hidden layer are fed to sigmoid function $S(x) = \frac{1}{1+e^{-x}}$ first. The true inputs to the perceptrons in output layer are thus the function values of the sigmoids. The network consists of connections, each connection transferring the output of a perceptron $\boldsymbol{i}$ to the input of a perceptron $\boldsymbol{j}$. In this sense $\boldsymbol{i}$ is the predecessor of $\boldsymbol{j}$ and $\boldsymbol{j}$ is the successor of $\boldsymbol{i}$. Each connection is assigned a weight $\theta_{ij}^{(l)}$, where l marks the layer the weights are associated with and take the values $1, ..., L-1$. A three-layer perceptron network thus is expressed as follows,

$$z_i = S(\sum_{j=1}^{d} \theta_{ij}^{(1)} x_j + \theta_{i0}^{(1)}) = S(\boldsymbol{\Theta_i^{(1)}} \boldsymbol{x}) \tag{2.20}$$

$$h_{\theta i} = \sum_{j=1}^{d} \theta_{ij}^{(2)} z_j + \theta_{i0}^{(2)} = \boldsymbol{\Theta_i^{(2)}} \boldsymbol{z} \tag{2.21}$$

where z_i represents the outputs of the perceptrons in the hidden layer.

With all the foundations provided so far, we hereby define the following cost function for an ANN applying the logistic discrimination for multi-class classification:

$$J(\Theta) = -\frac{1}{m}[\sum_{i=1}^{m}\sum_{k=1}^{K} y_k^{(i)} log h_\theta(x^{(i)})_k + (1 - y_k^{(i)}) log(1 - h_\theta(x^{(i)})_k))] \tag{2.22}$$

where, Θ is the matrix of all weights, h_θ is the output of the network, x is the input to the network, y corresponds to the classification vector and $y \in \mathbb{R}^K$, m represents the total number of training samples and K the number of classes for classification problem. Thus our goal is to minimize the cost function $J(\Theta)$ with the training samples, i.e., to find the set of Θ which gives us the smallest value of J. The most efficient way to find the local minimum for the cost function is the gradient decent method, which transfers the problem into searching for the weights that leads $\frac{\partial}{\partial \Theta_{ij}^{(l)}} J(\Theta)$ to approach 0.

One way to acquire the solution/weights is by performing back-propagation[]. Suppose we are to classify all samples into K different classes C_i, and construct a three-layer network to achieve the goal. When considering the hidden layer as input, the way to

update the corresponding weights is given as,

$$E = \frac{1}{2}(y_i - h_{\theta i})^2 = \frac{1}{2}(y_i - \boldsymbol{\Theta_i^{(2)}} \boldsymbol{z})^2 \tag{2.23}$$

$$\Delta\theta_{ij}^{(2)} = \frac{\partial E}{\partial \theta_{ij}^{(2)}} = \alpha(y_i - h_{\theta i}) z_j \tag{2.24}$$

where E is the square error defined over output by implementing regression, α is defined as the learning rate, y_i is 1 if $\boldsymbol{x} \in C_i$ and 0 otherwise. Then to update the weights connecting input to hidden layer, we need to make use of chain rule to calculate the gradient,

$$\frac{\partial E}{\partial \theta_{ij}^{(1)}} = \frac{\partial E}{\partial h_{\theta k}} \frac{\partial h_{\theta k}}{\partial z_i} \frac{\partial z_i}{\partial \theta_{ij}^{(1)}} \tag{2.25}$$

This method acts as if we are calculating the error in inputs by back-propagating from outputs, hence is called back-propagation. The following pseudo code shows how the weights are updated as well as how the errors are evaluated.

- Get the training set $(x^{(1)}, y^{(1)}), ..., (x^{(m)}, y^{(m)})$
- Set $\Delta_{ij}^{(l)} = 0$ for all l, i, j
- For $i = 1$ to m
  - Set $a^{(1)} = x^{(i)}$
  - Perform forward propagation to compute $a^{(l)}$ for $l = 2, 3, ..., L$: $a^{(l)} = g(\Theta^{(l-1)} a^{(l-1)})$
  - Using $y^{(i)}$, compute $\delta^{(L)} = a^{(L)} - y^{(i)}$
  - Compute $\delta^{(L-1)}$, $\delta^{(L-2)}$, ..., $\delta^{(2)}$
  - $\Delta_{ij}^{(l)} := \Delta_{ij}^{(l)} + a_j^{(l)} \delta_i^{(l+1)}$
- $D_{ij}^{(l)} := \frac{1}{m}\Delta_{ij}^{(l)} + \lambda \Theta_{ij}^{(l)}$ if $j \neq 0$

- $D_{ij}^{(l)} := \frac{1}{m}\Delta_{ij}^{(l)}$ if $j = 0$

It turns out that after performing the above algorithm, the gradient is $\frac{\partial}{\partial \Theta_{ij}^{(l)}} J(\Theta) = D_{ij}^{(l)}$. Detailed and rigorous proof is omitted for simplicity and interested reader are referred to the book by Alpaydin [83].

In practice, people rarely use networks with more than three layers. And for the seek of generality, the weights are randomly initialized to values between $[-0.01\ 0.01]$. It is also very common to normalize all inputs to speed up the calculation. In this project, a three-layer ANN is constructed with one hidden layer. As we know, the reason why humans' eye could tell different colors is that a specific spot stands out from its background texture. So we pick rectangular boxes that contain 25 pixels centering at the pixels that we know which class (red, green or transparent) they belong to as our training sample. Thus we need 75 inputs (25 pixels and each having its own R, G, B value) and three outputs (corresponding to three pre-defined classes). The error of the algorithm is calculated as a function of number of iterations before we stop the training over a total of 3000 training samples (80% of which used for training, 20% of which used to test). as shown in Fig. 2.4. We can see that after roughly 1000 iterations, the rate of correctness stabilize at around 99%, so we pick a total iteration of 2000 for best performance to acquire our trained network.

2.3 Conclusion

In this chapter, we introduce the experimental setup and the techniques utilized throughout the whole research to analyze experimental data, emphasizing on image processing. The experimental system is flexible enough to allow experiments with different combinations of controlling parameters, such as the flow rate Q, the particle size D, the oil viscosity μ etc.

Data analysis techniques including edge detection and particle concentration extraction are explained in detail. The algorithm and code developed based on the foundation

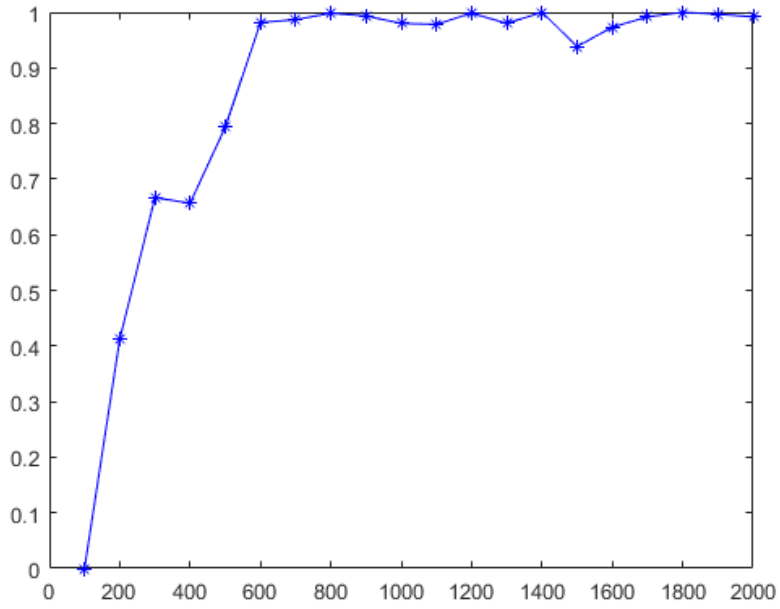

Figure 2.4: Correctness rate of neural-network algorithm as a function of total number of iterations. The rate increases with the increase of iterations and stabilizes after roughly 1000 iterations.

mentioned in this chapter is highly reusable and can be easily modified to accommodate different systems while still maintaining good performance. Experimental results and analyzed data will be presented in the following chapters.

3. PARTICLE-INDUCED VISCOUS FINGERING IN MONO-DISPERSE SUSPENSION*

3.1 Introduction

Although viscous fingering has been extensively investigated in the past few decades, the viscous fingering that is induced by the involvement of particles is rarely studied. Tang *et al*[72] first reported the unexpected fingering phenomenon when a mixture of non-colloidal particles and viscous fluid displaces air in a Hele-Shaw cell. Then, they qualitatively correlated the particle volume fraction, ϕ_0, to the instability growth rate. Later on Ramachandran & Leighton [56] observed the analogous fingering instability upon squeezing a particle-oil mixture between two parallel plates. These are the only existing research work available in literature and no quantitative analysis is yet available to the best knowledge of the authors.

In this chapter, we present our work to quantify this interesting viscous fingering phenomenon induced by particles. We perform complete series of carefully designed experiments. The experimental observations are then analyzed with the help of image processing technologies to get the particle distribution in the radial direction. We explain in detail that the fingering is a consequence of the shear-induced migration upstream of the unstable interface. Our theory is confirmed by the numerical calculations acquired following suspension balance model. The experimental observations and theoretical quantifications are compared, which provide satisfactory agreement.

*Part of this chapter is reprinted with permission from "Particle-induced viscous fingering'' by Feng Xu *et al*, 2016. Journal of Non-Newtonian Fluid Mechanics, Vol. 238, Pages 92-99, Copyright [2016] by Elsevier B.V. and from "Formation and Destabilization of the Particle Band on the Fluid-Fluid Interface'' by Jungchul Kim, Feng Xu and Sungyon Lee, 2017. Physical Review Letters, Vol. 118, Pages 074501, Copyright [2017] by American Physical Society.

3.2 Experimental Observations and Analysis

The experimental setup is described in Sec. 2.1. Among all the variables that are changeable, we focus on mainly two of them: initial particle volume fraction, ϕ_0, and the ratio of gap thickness to particle diameter, h/D. The experiments performed are summarized in Table 3.1. Fig. 3.1 shows a typical image of fingering at $\phi_0 = 0.35$ and $h/D = 10.2$: as particles accumulate on the interface, the fluid-fluid interface deforms with growing particle clusters (see zoomed-in image of Fig. 3.1). However, fingering does not occur in all conditions, as demonstrated in Fig. 3.2. At very low volume fractions, the distribution of suspension in the cell is uniform, with no resultant fingering. As ϕ_0 is increased, the particle accumulation on the meniscus becomes visible; finally, beyond some critical value of ϕ_0, the interfacial deformations appear, accompanied by the formation of particle clusters.

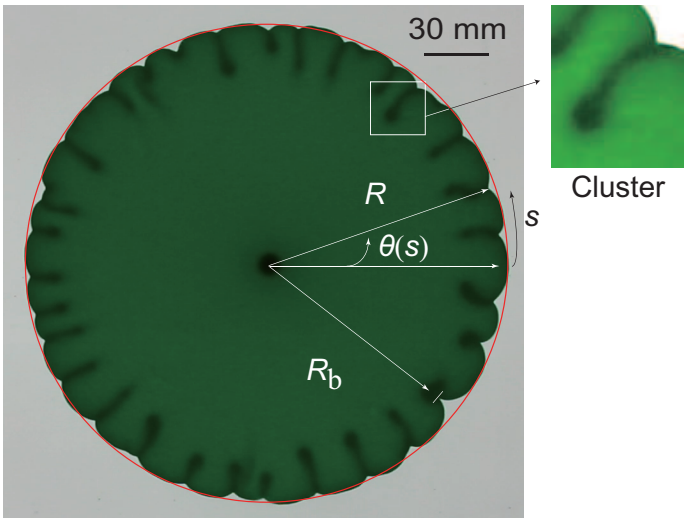

Figure 3.1: Image of fingering phenomenon at $\phi_0 = 0.35$, $h/D = 10.2$: both the interfacial deformations and particle clusters are clearly visible. The symbol, s, corresponds to the curvilinear coordinate defined along the edge; R_b is the instantaneous radius from the center to the interface, while R denotes the radius of the best fitted circle. The inset shows the zoomed image of the particle cluster that grows perpendicular to the interface.

D (μm)	h (mm)	ϕ_0 ($\times 100\%$)
125-150	0.635	10-18, 20-30 (increment of 1)
	0.762	12-30
	0.940	12-15, 17-32
	1.150	14, 15, 17, 20-28, 30-35
	1.270	8, 11, 14, 17, 20-35
	1.397	8, 11, 14, 15, 17, 20-35

Table 3.1: Experimental conditions tested; for all experimental runs, the flow rate Q and particle size D are kept constant at 150 mL/min and $125 - 150$ μm, respectively. A ϕ_0 range that is denoted as '# - #' increases by an increment of 1%.

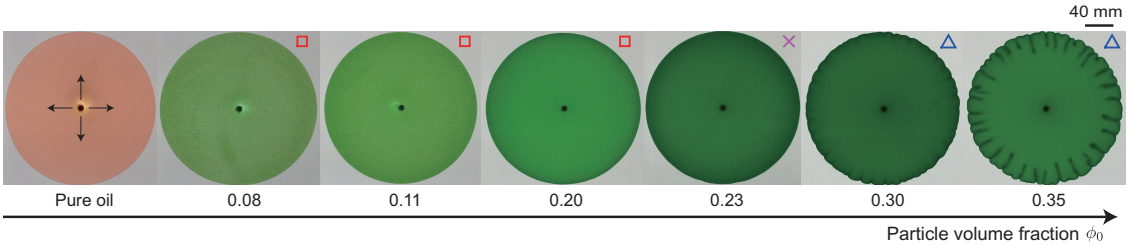

Figure 3.2: Dependence of fingering phenomenon on initial particle volume fraction, ϕ_0, is clearly demonstrated via the experimental images with $h/D = 10.2$ and increasing ϕ_0. At small ϕ_0, the distribution of suspension remains quite uniform. Interfacial deformations are first observed at $\phi_0 = 0.24$ and become more pronounced as ϕ_0 further increases. The black arrows in the pure oil case indicate the direction of the flow.

Fig. 3.3 illustrates the time-elapsed comparison between typical low concentration ($\phi_0 = 0.14$) and high concentration ($\phi_0 = 0.35$) cases, while all the other parameters (*i.e.* h/D, Q) remain unchanged. At $\phi_0 = 0.14$, the interface remains circular over time, with the uniform distribution of particles throughout. At $\phi_0 = 0.35$, the interfacial deformations and particle cluster formation are first observed around time $= 5.8$ s. As the interface advances further, the fingering patterns do not significantly change in magnitude,

while the particle clusters grow radially. Notably, the spatial distribution of interfacial fingers and particle clusters appears remarkably uniform for all times.

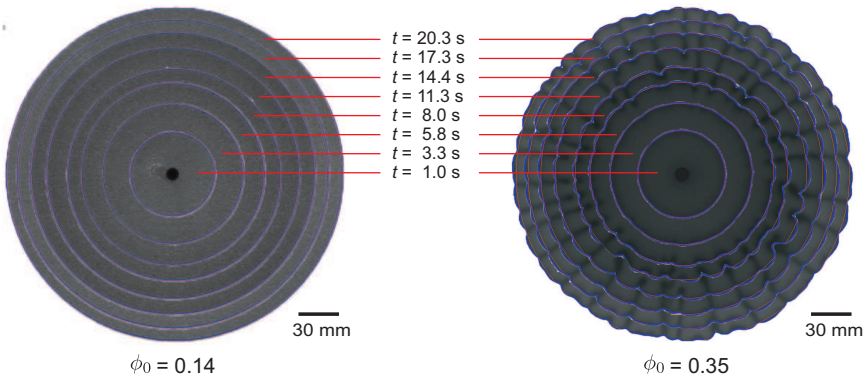

Figure 3.3: Time-elapsed images from two separate experimental runs: $\phi_0 = 0.14$ (left) and $\phi_0 = 0.35$ (right). At $\phi_0 = 0.14$, the shape stays almost circular over time, and the particle concentration appears uniform over the whole suspension. At $\phi_0 = 0.35$, interfacial deformations and particle clusters initially appear around $t = 5.8$ s and are observed for all times thereafter.

In addition, the plot of the instantaneous radius, R_b, as a function of θ in Fig. 3.4 clearly demonstrates the difference between the low and high concentration regimes; R_b at $\phi_0 = 0.35$ strongly varies with θ while that of $\phi_0 = 0.14$ remains relatively uniform, which matches the qualitative observations.

The overall magnitude of interfacial deformation can be computed as a single dimensionless parameter, Λ [56], such that

$$\Lambda = \frac{1}{S}\int_0^S \left(1 - \frac{R_\mathrm{b}(s)}{R}\right)^2 ds, \tag{3.1}$$

where s refers to the curvilinear coordinate defined along the interface, while R is the radius of the best fitted circle of the area occupied by the suspension (notations given in

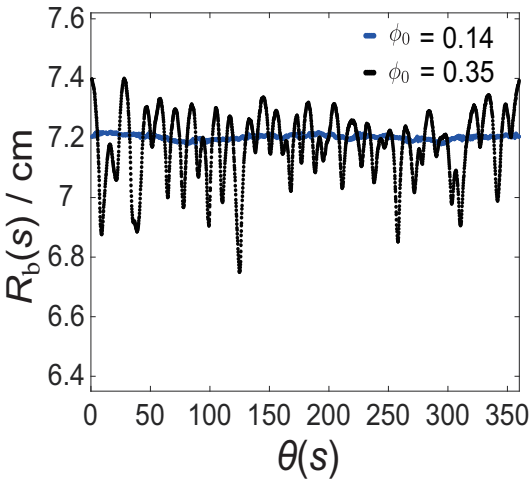

Figure 3.4: The plot of the center-to-interface distance, $R_{\rm b}$ for $\phi_0 = 0.14$ and 0.35 at $h/D = 10.2$. Consistent with the interfacial shapes in Fig. 3.3, $R_{\rm b}$ is nearly uniform for $\phi_0 = 0.14$, indicating a circular shape, while $R_{\rm b}$ for $\phi_0 = 0.35$ strongly varies with θ.

Fig. 3.1). As Λ characterizes the deviation of the instantaneous interface from a circle, it reduces to zero when $R_{\rm b}(s) = R$, or the interface forms a perfect circle. Fig. 3.5 shows the plot of Λ versus $R(t)/R_0$ for varying values of ϕ_0. Consistent with our observations, Λ at early times appears to be independent of ϕ_0 for all cases within the margin of error [84]. The effect of ϕ_0 on Λ is evident at later times, as Λ rises much more significantly for larger ϕ_0. However, overall the value of Λ remains in the order of 10^{-4} even for large ϕ_0, suggesting that the interfacial deformations are minimal, compared to the classical viscous fingering with fractal-like patterns [85]. Interestingly, our fingering patterns are reminiscent of "stubby" fingers observed by Pilher-Puzovic and co-authors [86] who displaced oil with air in an elastic walled channel. In [86], the elastic membrane is shown to *stabilize* the unstable air-oil interface, hence, suppressing the growth of fingers. Similarly, in our present work, the inherently stable viscosity ratio between the suspension and air also suppresses interfacial deformations and yields "stubby" fingers.

Based on aforementioned observations and measurements, each experimental run can

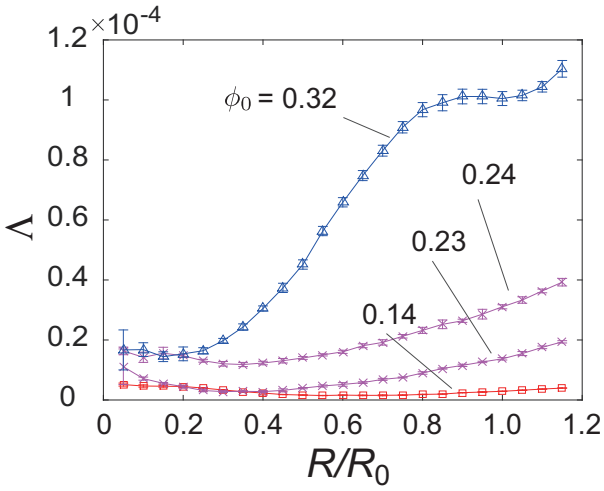

Figure 3.5: The plot of Λ over dimensionless time, R/R_0, at different initial concentration ϕ_0

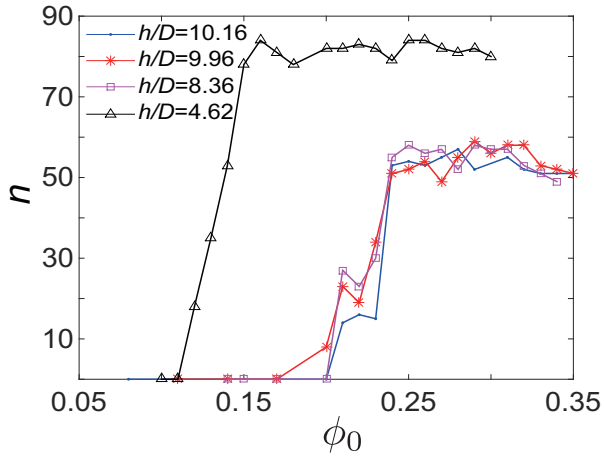

Figure 3.6: The number of total fingers, n, at $R \approx 10$ cm is counted for all ϕ_0, At $h/D = 10.2$, for instance, there is a sharp increase in n at $\phi_0 = 0.23 - 0.24$ and plateaus to approximately 50 for large ϕ_0. This transition point in n is used to systematically determine the boundary between "no fingering" and "fingering" regimes

be organized into 'no fingering' versus 'fingering' regimes, for given ϕ_0 and h/D. In order to identify the transition between the two regimes in a consistent and quantitative manner, the total number of fingers, n, (determined by the number of local minima in

R_b) at $R \approx 10$ cm has been extracted for varying ϕ_0 and h/D. For given h/D, n sharply increases for increasing ϕ_0 and plateaus to a relatively constant value for large ϕ_0 (Fig. 3.6). In corroboration with the videos, this point of transition in n reliably marks the boundary between 'no fingering' versus 'fingering' regimes. For instance, at $h/D = 10.2$, the interface consists of approximately 20 fingers for $\phi_0 = 0.23 - 0.24$, which more than doubles for $\phi_0 \geq 0.25$. Accordingly, $\phi_0 = 0.23 - 0.24$ is considered the transition regime.

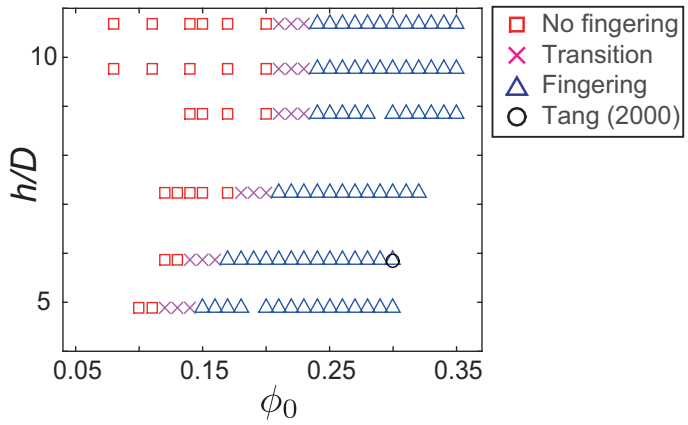

Figure 3.7: All experimental runs are organized into a phase diagram that shows the dependence of fingering instability on ϕ_0 and h/D. At large h/D, the boundary between no fingering (square) and fingering (triangle) appears to be independent of h/D; however, the onset of fingering notably shifts to a smaller value of ϕ_0 as h/D decreases (the bottom three rows of data).

Based on the values of n, we systematically determine fingering regimes and summarize them in a ϕ_0-h/D phase diagram. In Fig. 3.7, the square and triangle symbols correspond to 'no fingering' and 'fingering' regimes, respectively, while '$\times$' indicates the transition between the two. For large $h/D \gtrsim 10$ or the "continuum" limit, the onset of fingering appears to coincide with $\phi_0 \approx 0.24$, independent of h/D. This h/D-independent behavior is also evident in the number of fingers; for $h/D \gtrsim 10$, n plateaus at around 50, while it reaches up to 80 for smaller h/D. Interestingly, in addition to an increase in n, the

fingering initiates at lower ϕ_0 as h/D decreases. This alludes to two possible effects that affect fingering: the effects of wall confinement (*i.e.* small h/D) and the increased injection velocity that scales as $Q/(rh)$. To decouple the two effects, additional experiments have been conducted in which the injection velocity is kept constant (by adjusting Q for varying h). The results reveal that decreasing h at a constant injection velocity induces fingering at a lower value of ϕ_0, confirming the effects of wall confinement. On the other hand, the increased velocity is shown to cause fingering to initiate at a larger radius; this transient nature of fingering is beyond the scope of this manuscript and will be addressed as future work.

D (μm)	h (mm)	ϕ_0 ($\times 100\%$)
300-355	0.400	7-10, 12-15, 20-25, 27, 30 (increment of 1)
	0.635	7-10, 12, 15-17, 19-23, 25, 27-30
	0.762	7-16, 18, 20-22, 25, 27, 30
	1.150	5-20, 22, 25, 27, 30
	1.397	6, 8-10, 12-18, 20, 22, 25, 27, 30

Table 3.2: Experimental conditions tested; for all experimental runs, the flow rate Q and particle size D are kept constant at 150 mL/min and $300 - 355$ μm, respectively. A ϕ_0 range that is denoted as '# - #' increases by an increment of 1%.

We have also ran experiments at much smaller gap over diameter ratio $h/D < 4$, where particles with larger diameter ($D = 300 \sim 355\mu m$) are used in suspension, see Table 3.2 for a complete list of experimental runs. Similar phenomenon is observed: the interface stays stable at low particle concentrations, and with the increase in ϕ_0, the fingering starts to appear and becomes more and more pronounced. Of-course, the clusters observed before appear again in this series of experiments, each of which corresponds to a finger. The trend in fingering phenomenon over ϕ_0 is summarized in Fig. 3.8. It is worth mentioning that compared to those experiments at much larger ratios of h/D, the instability initiates

at lowers concentration. What's more, we are very surprised to find that at relative high concentrations, a distinct phenomenon is observed, where the particles accumulate at the interface and form a very thick band. The band expands and breaks up later on, which leads to a much more pronounced fingering compared to large h/D ratio case where small particles are used. Fig. 3.9 is a showcase of the thick particle band and its breakup, accompanied by a severe deformation of the interface.

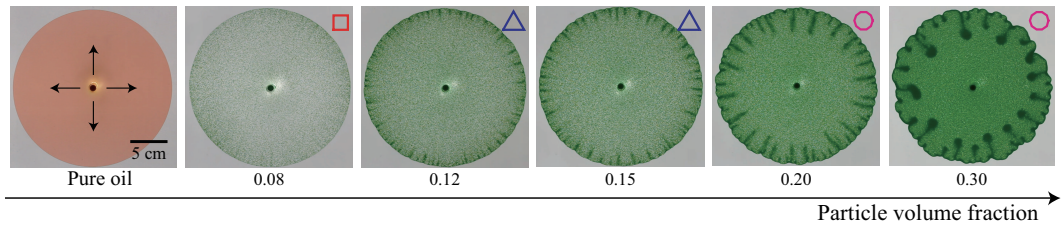

Figure 3.8: Dependence of fingering phenomenon on initial particle volume fraction, ϕ_0, at much smaller gap diameter ratio, $h/D = 3.5$. At small ϕ_0, the distribution of suspension remains quite uniform. Interfacial deformations are first observed at $\phi_0 = 0.12$ and become more pronounced as ϕ_0 further increases. It can also be clear seen that the deformation occurs at lower concentration compared to $h/D = 10.2$ shown in Fig. 3.2. The black arrows in the pure oil case indicate the direction of the flow.

We then perform similar analysis as we mention above to calculate the Λ values for experiments with small h/D. For relative low concentrations, we find that the values of Λ gradually increase over radius R. However, at higher concentrations, especially when the aforementioned thick band is observed, we notice that there is a peak in the $\Lambda - R$ plot. When we compare the Λ values carefully with the experimental images, we figure that the peak actually corresponds to the breakup of the band. We do also compare the Λ plots acquired from different h/D ratios, we find that there is a significant difference in the magnitudes, where those of small h/D are much larger than those linked to large ratios, see Fig. 3.10.

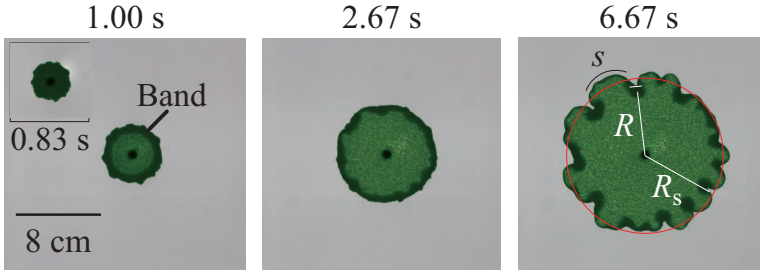

Figure 3.9: Time evolution of band fingering at $h/D = 3.5$ and $\phi_0 = 0.30$. It can be seen clearly that there is a thick band at early stage and the band later breaks up, leading to significant interfacial deformation. The symbols s indicates we follow a curvilinear coordinate, the R and R_s corresponds to the instant radius and the radius of best-fitted circle, respectively.

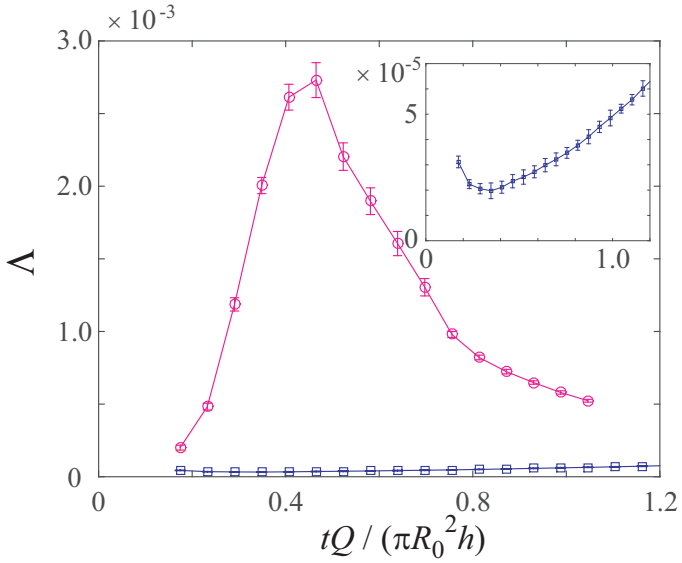

Figure 3.10: Comparison of Λ plots at different h/D ratios while keeping the initial concentration the same (*i.e.* $\phi_0 = 0.30$). The curve which contains a peak corresponds to band fingering at $h/D = 3.5$ while the other curve is obtained from experiment with $h/D = 8.2$.

Based on the Λ plots generated from different experiments by varying the h/D ratio, while still keep the ratios relatively small (the largest ratio in this series of experiment is kept at 4.2), we summarize all experiment in the following phase diagram. In the digram,

all experiments are divided into three regime, the 'no fingering', the 'weak fingering' and the 'band fingering', as shown in Fig. 3.11. The fingering depends on h/D ratio in two ways, on one hand, there exists a boundary between 'no fingering' and 'weak fingering'; on the other hand, the 'band fingering' appears to be delayed with decreasing h/D ratio

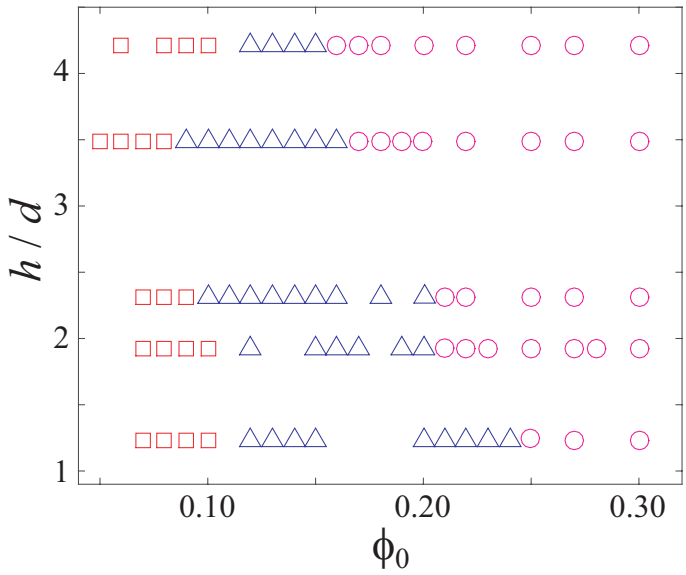

Figure 3.11: Summary of experiments carried out at relatively small h/D ratios. Experimental points are classified into three regimes, the 'no fingering', the 'weak fingering' and the 'band fingering'. All experiments are carried out with $Q = 150mL/min$.

In order to confirm the particle accumulation experimentally, we measure the depth-averaged volume fraction $\bar{\phi}$, as a function of the radial position r. Detailed description of methods utilized to extract the $\bar{\phi}$ profile is given in Sec. 2.2.3. Fig. 3.12 demonstrates typical $\bar{\phi}(r)$ profiles evolving over time for two different values of ϕ_0: (a) $\phi_0 = 0.11$ that falls in the no fingering regime and (b) $\phi_0 = 0.32$ with clear fingering. For both cases, the particle volume fraction at the entrance is consistently lower than ϕ_0 and rises as $r \to R$. This rise in ϕ near the interface is notably steeper for larger ϕ_0 and is preceded by the

region of constant ϕ. Interestingly, Fig. 3.12 suggests that the increase in $\bar{\phi}$ over r alone does not guarantee the occurrence of fingering.

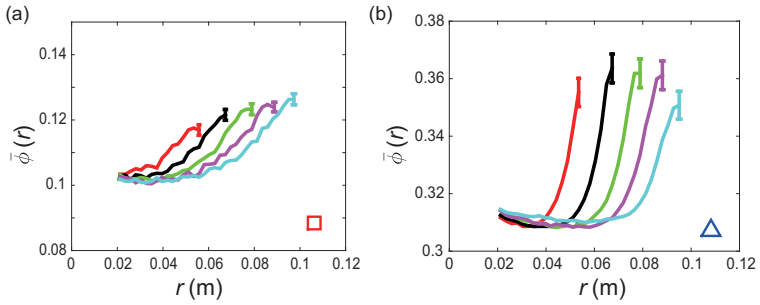

Figure 3.12: Profile of particle volume fraction at $h/D = 10.2$ and $\phi_0 = 0.11$ (a) and $\phi_0 = 0.32$ (b), respectively. In both plots, the depth-averaged local volume fraction $\bar{\phi}(r)$ increases in r. At $\phi_0 = 0.32$, the curve increases more sharply, preceded by a notably constant region of $\bar{\phi}$, compared to the $\phi_0 = 0.11$ case that shows a more gradual increase. The error in $\bar{\phi}_0$ as a result of an estimated 1% error in I has been computed to be approximately ± 0.002 for all times and r and included as error bars.

3.3 Mono-disperse Suspension Balance Model

Particle-induced viscous fingering is caused by the accumulation of particles on the meniscus, as described in Fig. 3.13(b). This increase in particle concentration directly correlates to an increase in the effective suspension viscosity, which results in *miscible* viscous fingering and subsequent formation of particle clusters (labelled as C in Fig. 3.13(d)). Finally, the interface deforms due to a greater flow resistance through viscous clusters (C) relative to the surrounding medium (D) (see Fig. 3.13(e)). Therefore, as shown in Fig. 3.3, the particle clusters and fingering patterns on the interface are perfectly correlated from its initial appearance over time. Furthermore, if more particles collect near the interface with increasing ϕ_0, more pronounced interfacial deformations and particle clustering are observed. Therefore, the key to understand particle-induced fingering lies in the funda-

mental understanding of the particle accumulation mechanism. However, it is important to note that the particle accumulation on the interface is a bare *minimum* condition for fingering, not necessarily a sufficient one in itself, as demonstrated in Fig. 3.12(a), and requires further investigation.

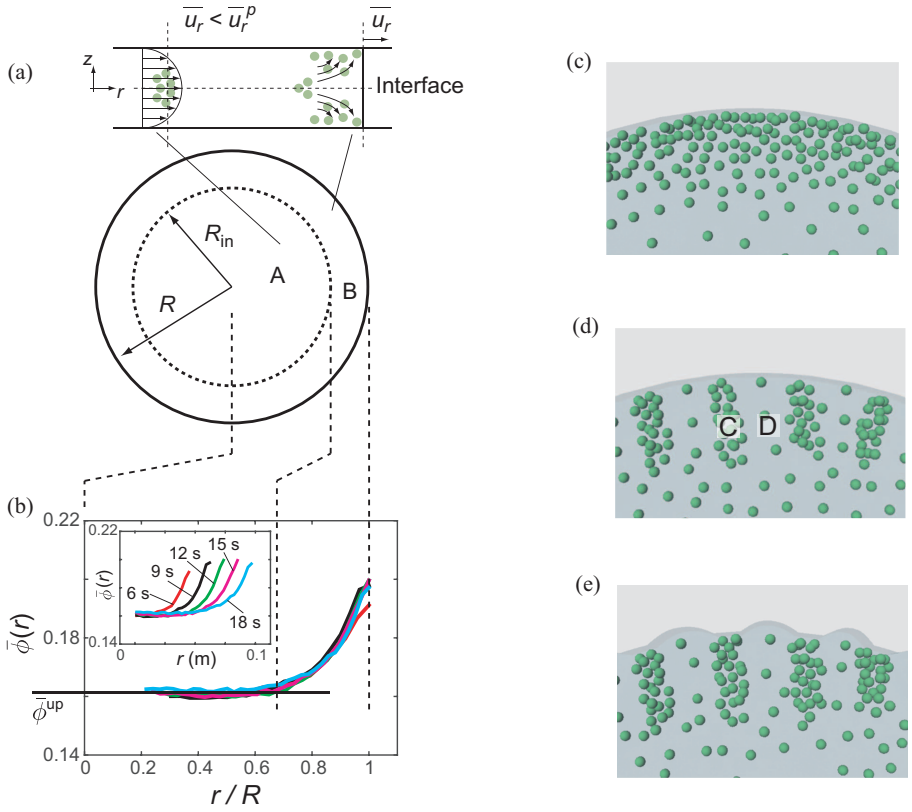

Figure 3.13: (a) The radial particle-laden flow is divided into an upstream region (A) versus downstream region (B). In region A, the flow can be assumed to be steady and unidirectional, resulting in a simple 1D model based on the suspension balance approach. The particle dynamics in region B involves the effects of a fountain flow and is not straightforward to model at this stage. (b) The plot of $\bar{\phi}$ versus r/R for $\phi_0 = 0.17$ and $h/D = 10.2$ that clearly exhibits an upstream region A over which $\bar{\phi}$ is constant followed by B over which $\bar{\phi}$ steeply rises. (c)-(e) Schematic illustrating the sequence of events that lead to fingering: (c) particles collect near the interface as they move faster than the suspension; (d) the concentration gradient yields an effective viscosity gradient that leads to miscible fingering and particle clustering; (e) the relatively slow flow through clusters causes interfacial deformations.

Two physical mechanisms behind the particle accretion on the meniscus have been identified, originally in the context of the particle-laden flow in a tube: *particle-entrainment* in the "fountain" flow and *shear-induced migration* in the fully-developed upstream flow [30, 31, 87]. Karnis and Mason found that the fountain flow near the meniscus diverts particles that approach the interface towards the tube walls; however, finite-sized particles become re-entrained into the fountain flow instead of being swept onto the walls, leading to particle accumulation [30]. Accordingly, this wall exclusion effect is supposed to vanish in the limit of vanishingly small particles, or in the continuum limit.

Surprisingly, Chapman demonstrated experimentally that the meniscus enrichment is present even in the continuum limit due to particle migration far upstream of the interface [31]. Shear-induced migration refers to the particle diffusion from the regions of high shear (*i.e.* near channel walls where particles are more likely to collide) to those of low shear in a fully-developed, pressure-driven flow [26, 48]. Hence, as illustrated in Fig. 3.13(a), upstream of the interface, there are more particles near the centerline where the flow is the fastest, leading to a net flux of particles towards the interface that is moving at the mean suspension velocity. Therefore, this net flux of particles upstream of the interface leads to the non-zero accumulation of particles near the interface, even in the continuum limit in which the wall exclusion effects are negligible.

The analogous particle accretion phenomenon that drives the interfacial instability is also observed in our current Hele-Shaw geometry, as it has previously been shown in [72, 56]. While the actual mechanism behind particle accretion may be some combination of particle dynamics in the fountain flow and in the fully-developed flow, we presently focus on the effects of shear-induced migration upstream of the interface, which should be dominant in the continuum limit. We hereby define the ratio of the upstream mean particle

speed, $\bar{u}_r^{\mathrm{p}}$, to that of the suspension, $\bar{u}_r$, in the following way:

$$\beta \equiv \frac{\bar{u}_r^{\mathrm{p}}}{\bar{u}_r} = \frac{(\bar{\phi}h)^{-1}\int_{-h/2}^{h/2} u_r^{\mathrm{p}}\phi dz}{h^{-1}\int_{-h/2}^{h/2} u_r dz}, \tag{3.2}$$

where $\bar{\phi}(r) = h^{-1}\int_{-h/2}^{h/2}\phi dz$, and u_r and u_r^{p} denote local suspension and particle radial velocities, respectively. As previously explained, the value of β must be greater than 1 far upstream of the interface, in order for the particle accretion and fingering to occur. In addition, β qualitatively corresponds to the *rate* of particle accumulation on the interface, while the detailed particle concentration near the interface is strongly coupled to the fountain flow [30] (*i.e.* regime B in Fig. 3.13(a)), which is beyond the scope of the paper. Therefore, we will theoretically verify this necessary condition for particle accumulation (*i.e.* $\beta > 1$), by deriving the expression of β as a function of ϕ_0 and h/D in the upstream regime away from the interface (A in Fig. 3.13(a)).

In order to compute β that depends on ϕ and velocity profiles, we model the particle-laden flow as a continuum based on the suspension balance approach [52]. The suspension balance method [52] considers the conservation of mass and momentum of both the overall suspension and the particulate phase in the low Reynolds number limit. Then, the governing equations are given as follows: for the suspension,

$$\nabla \cdot \mathbf{u} = 0, \tag{3.3}$$

$$\nabla \cdot \mathbf{\Sigma} = 0, \tag{3.4}$$

and for the particulate phase,

$$\frac{\partial \phi}{\partial t} + \nabla \cdot (\phi \mathbf{u}^{\mathrm{p}}) = 0, \tag{3.5}$$

$$\nabla \cdot \mathbf{\Sigma}^{\mathrm{p}} + \mathbf{F} = 0, \tag{3.6}$$

where $\boldsymbol{\Sigma}$ and $\boldsymbol{\Sigma}^{\mathrm{p}}$ correspond to the total stress tensors of the suspension and particulate phase, respectively. The inter-phase drag force, $\mathbf{F}$, is given by

$$\mathbf{F} = -\frac{18\eta_{\mathrm{l}}}{D^2}\frac{\phi}{f(\phi)}(\mathbf{u}^{\mathrm{p}} - \mathbf{u}), \tag{3.7}$$

where the hindrance function, $f(\phi)$ has an empirical form, $f(\phi) = (1-\phi)^n$, with $n \approx 5.1$ in the Stokes flow [88]. Note that, specific to our current geometry, the governing equations will be considered in the cylindrical coordinate system, such that the suspension velocity vector is given by $\mathbf{u} = (u_r, u_\theta, u_z)$; $\mathbf{u}^{\mathrm{p}}$ refers to the velocity vector of the particulate phase.

The suspension and particulate phase are coupled through the constitutive relationships of the stress tensors, namely,

$$\boldsymbol{\Sigma} = -p\mathbf{I} + \eta_{\mathrm{l}}\left[\nabla\mathbf{u} + \nabla\mathbf{u}^{\mathsf{T}}\right] + \boldsymbol{\Sigma}^{\mathrm{p}}, \tag{3.8}$$

$$\boldsymbol{\Sigma}^{\mathrm{p}} = \boldsymbol{\Sigma}^{\mathrm{p}}_{\mathrm{n}} + \left(\eta_{\mathrm{s}}(\phi) - \eta_{\mathrm{l}}\right)\left[\nabla\mathbf{u} + \nabla\mathbf{u}^{\mathsf{T}}\right], \tag{3.9}$$

where p is the suspension pressure, and the effective suspension viscosity, η_{s}, is empirically given as

$$\eta_{\mathrm{s}}(\phi) = \eta_{\mathrm{l}}\frac{\exp\left(-2.34\phi\right)}{(1-\phi/\phi_{\mathrm{m}})^3}, \tag{3.10}$$

valid even for dense suspensions [89], where $\phi_{\mathrm{m}} = 0.62$ is the maximum packing fraction. Furthermore, the particulate stress, $\boldsymbol{\Sigma}^{\mathrm{p}}$, consists of the viscously generated normal stress, $\boldsymbol{\Sigma}^{\mathrm{p}}_{\mathrm{n}} \propto \eta_{\mathrm{n}}\dot{\gamma}$, where $\dot{\gamma}$ is the shear rate and η_{n} refers to the effective normal viscosity [89, 54]:

$$\frac{\eta_{\mathrm{n}}}{\eta_{\mathrm{s}}} = \frac{0.75(\frac{\phi}{\phi_{\mathrm{m}}})^2(1-\frac{\phi}{\phi_{\mathrm{m}}})^{-2}}{1 + 2.5\phi_{\mathrm{m}}(1-\frac{\phi}{\phi_{\mathrm{m}}})^{-1} + 0.1\frac{\phi^2}{\phi_{\mathrm{m}}}(1-\frac{\phi}{\phi_{\mathrm{m}}})^{-2}}. \tag{3.11}$$

In the upstream regime (A) away from the interface, it is reasonable to assume a steady

state suspension flow, so that the governing equations for the particulate phase yield $\nabla \cdot \mathbf{\Sigma}^{\mathrm{p}} = 0$, and $\mathbf{u}^{\mathrm{p}} - \mathbf{u} = 0$. Furthermore, in the lubrication limit (*i.e.* $\partial/\partial r \ll \partial/\partial z$) and assuming axisymmetry (*i.e.* $\partial/\partial\theta = 0$), the particulate governing equation reduces to

$$0 = \frac{d}{dz}\left(-\eta_{\mathrm{n}}\dot{\gamma}\right), \tag{3.12}$$

where $\dot{\gamma} = du_r/dz$ in the thin-film limit; physically, this equation implies that the particles must arrange themselves in the z-direction in such a way that the normal stress is constant throughout the thin film. Under the same assumptions, the suspension momentum equation reduces to

$$\frac{dp}{dr} = \frac{d}{dz}\left(\eta_{\mathrm{s}}\dot{\gamma}\right). \tag{3.13}$$

Integrating both sides with respect to z, subject to the boundary condition, $\dot{\gamma}(z = 0) = 0$, yields $(dp/dr)z = \eta_{\mathrm{s}}\dot{\gamma}$. Hence, by combining Eq. (3.12) and (3.13), we obtain the following ordinary differential equation,

$$\frac{\eta_{\mathrm{n}}}{\eta_{\mathrm{s}}} z = \left(-\eta_{\mathrm{n}}\dot{\gamma}\right)\left(\frac{dp}{dr}\right)^{-1} = \text{constant}, \tag{3.14}$$

which can be solved numerically to yield ϕ, u_r, and p, subject to

$$Q = 2\pi r \int_{-h/2}^{h/2} u_r dz, \tag{3.15}$$

$$Q\phi_0 = 2\pi r \int_{-h/2}^{h/2} u_r^{\mathrm{p}} \phi dz, \tag{3.16}$$

where $u_r^{\mathrm{p}} = u_r$. The two conditions above, (3.15) and (3.16), ensure the steady flow rate of the mixture, Q, as well as the uniform concentration, ϕ_0, upon injection.

The resultant local volume fraction, $\phi(z)$, and the mixture velocity profile, u_r, are plotted in Fig. 3.14 and Fig. 3.15 respectively, which qualitatively match the previous results

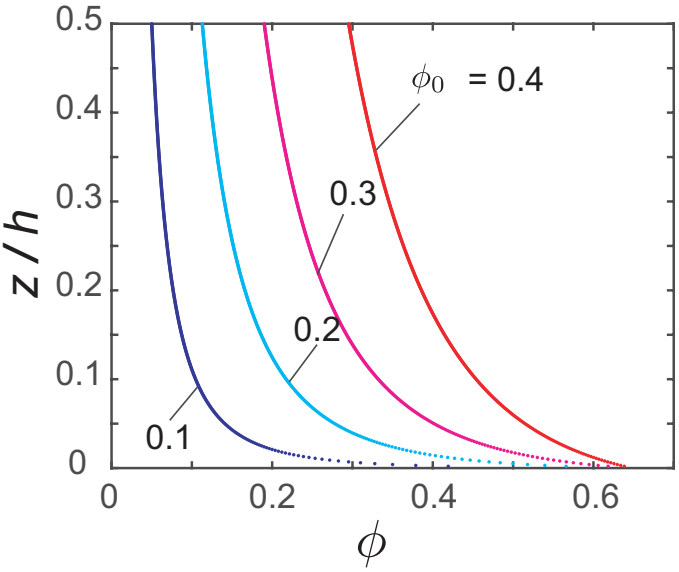

Figure 3.14: Profiles of local ϕ along the z-axis for varying ϕ_0.

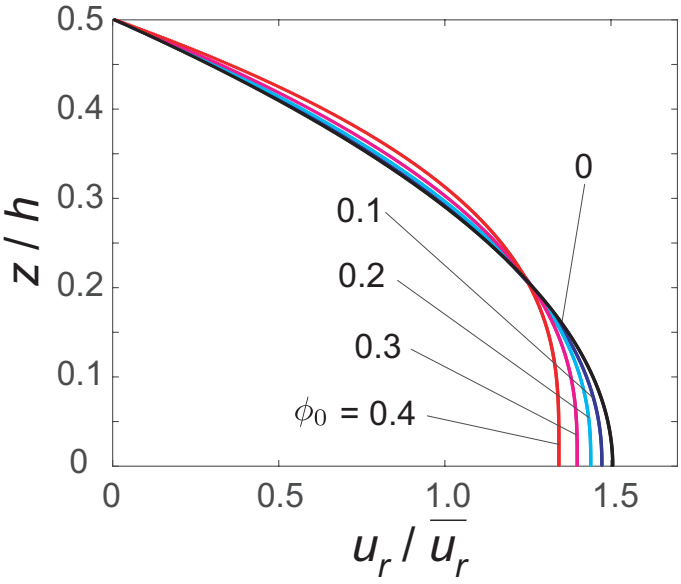

Figure 3.15: Profiles of normalized radial velocity, $u_r/\bar{u}_r$, along the z-axis for varying initial concentrations ϕ_0.

of a fully-developed 1D suspension flow [52, 90, 91]. Due to shear-induced migration, or, equivalently, to ensure constant particulate normal stress, the particle concentration is found to be higher near the centerline ($z = 0$) than near the wall ($z = h/2$). Unlike the diffusive flux model [91], the particle concentration at $z = 0$ remains below ϕ_{m} for the range of ϕ_0 considered (Fig. 3.14(a)). The corresponding dimensionless velocity profile, $u_r/\bar{u}_r$, is plotted in Fig. 3.14(b) and exhibits the blunting of the velocity near $z = 0$, due to a higher particle concentration at the centerline, also consistent with previous findings [52, 90, 91].

Going back to the necessary condition for particle accumulation and fingering, we expect the ratio of the mean particle velocity to the mean suspension velocity, β, to be greater than 1. As a direct result of higher ϕ near $z = 0$ where the flow is the fastest, we show in Fig. 3.16(a) that $\beta > 1$ for all ϕ_0; however, β surprisingly *decreases* with ϕ_0. The latter indicates that the resultant fingering does not generally increase with the *rate* of particle accumulation on the interface, given by β. Instead, the fingering mechanism is shown to depend on the *total amount* of particles accumulated on the interface, $\phi_0(1 - \beta^{-1})$: the product of the relative particle accumulation rate, $(\beta - 1)$, and the depth-average particle concentration in the upstream regime, $\bar{\phi}^{\mathrm{up}} = \phi_0\beta^{-1}$, by mass conservation in Eq. (3.16). As $\phi_0(1-\beta^{-1})$ increases, the higher particle concentration and effective viscosity become higher near the interface. As a result, larger $\phi_0(1 - \beta^{-1})$ is more likely to cause miscible fingering and interfacial deformations. As shown in Fig. 3.16(b), $\phi_0(1 - \beta^{-1})$ increases with ϕ_0; thus, fingering becomes more pronounced as ϕ_0 increases, as shown in Fig. 3.2. Note that there is no explicit dependence on h/D in the continuum model, which qualitatively explains why the fingering onset appears to be independent of h/D for $h/D \gtrsim 10$, as shown in Fig. 3.7.

As $\bar{\phi}^{\mathrm{up}}$ can be directly measured from experimental results shown in Fig. 3.12, we can thus obtain the value of β experimentally (denoted with superscript 'exp') and compare

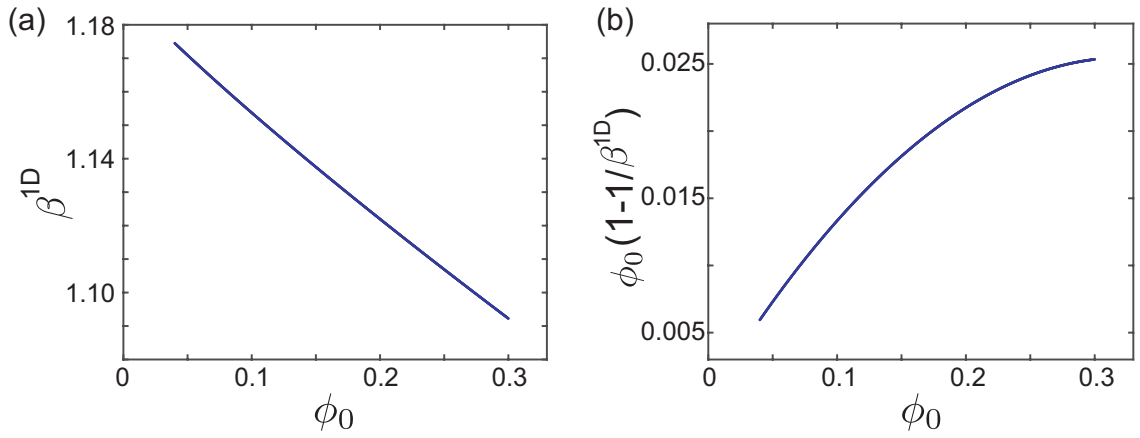

Figure 3.16: Plots of (a) β^{1D} and (b) $\phi_0(1-1/\beta^{1D})$ with varying ϕ_0, where β^{1D} denotes β derived based on the suspension balance model.

it to that derived theoretically (denoted with superscript '1D'). The resultant plot of β^{1D} versus β^{exp} shows a reasonable collapse onto a single line of the slope $= 1.06$, for all values of ϕ_0 and h/D considered, shown in Fig. 3.17. Finally, the average concentration of downstream region, ϕ_{av}, is derived as $\phi_{av} = \phi_0 + \phi_0(1-\beta^{-1})R_{in}^2/(R^2 - R_{in}^2)$ by volume conservation of particles. According to Fig 3.13(b), the size of the upstream regime, R_{in}, collapses onto a single line for all times when scaled by R. This implies that $R_{in} \propto R$, which leads to $\phi_{av} - \phi_0 \propto \phi_0(1-\beta^{-1})$. Therefore, for given ϕ_0, the average downstream concentration, ϕ_{av}, does not change over time, while the local particle concentration near the interface cannot be computed without resolving the fountain flow.

3.4 Conclusion and Future Work

In summary, we hereby present the particle-induced viscous fingering when a suspension of neutrally buoyant particles and oil is injected radially into a Hele-Shaw cell, which was previously observed in [72, 56]. This surprising fingering phenomenon is directly due to the presence of particles, as the injection of a clear oil into a Hele-Shaw cell is inherently stable. Building on the previous work [72, 56], we experimentally quantify the

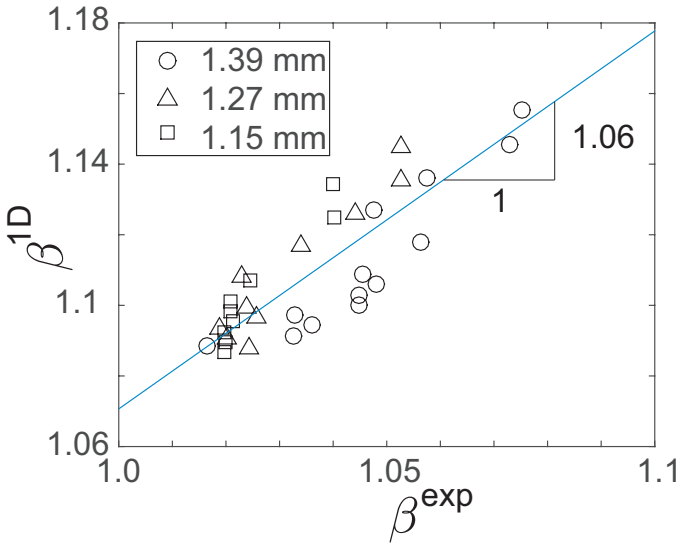

Figure 3.17: The values of β^{1D} reasonably match those obtained experimentally (*i.e.* β^{exp}) for varying ϕ_0 and h/D.

critical volume fraction, ϕ_0, at which fingering initiates for given h/D, by measuring the the total number of fingers at a fixed suspension radius. In addition, we experimentally measure the depth-average particle concentration, $\bar{\phi}$, which clearly shows that the particles accumulate near the interface. This increase in particle concentration near the interface corresponds to a higher effective viscosity; this viscosity gradient results in *miscible* fingering and subsequent interfacial deformations.

In tandem to experiments, we use the suspension balance approach to model the particle-laden flow as a continuum valid in the limit of $D/h \ll 1$, far upstream of the interface where we can reasonably assume a fully-developed, unidirectional flow. This simple model is motivated by the fact the particle accumulation on the interface arises from shear-induced migration of particles upstream of the interface. Specifically, we compute β which is the measure of the particle accumulation rate on the interface as a function of ϕ_0. Our results indicate that, while β must be greater than 1 for fingering to occur, fingering depends more directly on the total amount of particles collected near the interface, given by

$\phi_0(1-\beta^{-1})$, instead of β alone.

Although the particle-induced viscous fingering shares similar fundamental physics with miscible viscous fingering for clear fluids, some key differences exist. Notably, while miscible fingering occurs inside the suspension flow, "de-fingering" must also take place on the interface, since the air viscosity outside of the interface is much lower than the suspension viscosity. This stabilizing effect suppresses the finger growth; thus, the particle-induced viscous fingering exhibits relatively dull and short fingers, distinct from narrow and long fingering patterns observed in the clear fluid counterpart [**?**]. During "de-fingering", two adjacent fingers merge, leaving a particle cluster between the fingers. This process is repeatedly observed, splitting each finger into mostly two fingers, which is part of our on-going investigation. Additional on-going work includes performing a stability analysis of the particle-laden flow to identify the critical value of ϕ_0 that leads to miscible fingering. While our current simple model successfully validates the effect of shear-induced migration on particle accumulation, further analysis is needed to predict the onset of fingering as well as to understand the particle dynamics in the fountain flow region. Finally, complete understanding of the effect of the wall confinement on fingering may necessitate full numerical simulations based on Stokesian dynamics [92].

Overall, the interfacial instability in the suspension flow is relevant for various geophysical flows as well as numerous applications both in the energy sector (*i.e.* enhanced oil recovery) and biomedical field. Despite its significance, the coupled dynamics between the fluid-fluid interface and particles remains relatively unexplored, and this work represents initial steps towards elucidating this coupling. The results of this study can be expanded to other types of flows involving suspension film flows, such as suspension drop dynamics on a surface, suspension spreading in a rheometer [56], or blood flows in a thin film geometry [93].

4. PARTICLE-INDUCED VISCOUS FINGERING IN BI-DISPERSE SUSPENSION

4.1 Introduction

Researchers have investigated very deeply in the migration of particles in mono-disperse suspension over the past few decades. More recently, particle migration in bi- or poly-disperse suspension is drawing more and more attention in different flow geometries. For example, Husband and colleagues [41] measured the particle migration in suspensions of bimodal spheres and confirmed that suspended particles migrate from regions of high shear rate to regions of low shear rate. They also reported in the same paper that coarse fraction of particles migrates much faster than the fine fraction, which lead to size segregation of initially well-mixed suspensions. Later on Lyon and Leal [42] designed detailed experiments to report the velocity and concentration profiles for suspensions of bi-disperse distributed particles undergoing pressure-driven flow through a parallel-wall channel. From the perspective of theoretically modeling, Shauly and colleagues [51] studies the effect of particle radii on shear-induced migration in Couette flow by constructing a phenomenological model, where their calculation received good agreement with available data from other groups. Norman *et al* [43] modified the suspension balance model by adding a constitutive stress equation for a second species of particle to calculate the respective concentration profile of both sizes of particles.

In terms of the interfacial instability induced by particles occurring in suspension flow, we find only Tang *et al*[72] and Ramachandran & Leighton [56] have conducted relevant studies in mono-disperse suspension. The kind of research involving bi-disperse suspension is still completely missing, though we believe there is rich physics lying behind the observations. In this chapter, the author will extend his research introduced in previous chapter by introducing a second species of particle with different size (diameter) into the

system and study the particle induced viscous fingering in bi-disperse suspension both experimentally and theoretically.

The chapter is organized as follows. We first explain in detail the experiments we have performed, by presenting observations directly obtained from recorded videos. The experimental data are carefully examined and analyzed to provide more quantitative explanation. We then introduce the SBM specifically modified to accommodate the bi-disperse system. Numerically calculations are presented including the concentration and velocity profiles across the gap, the radial direction flux etc.

4.2 Experimental Results

It should be clarified first that all the experiments are performed utilizing the same setup as introduced in Fig. 2.1. Before each experimental run, the particles having different sizes in diameter are weighed separately to give precise initial volume fraction. The mixture are shaken to make sure the particles are uniformly distributed before injected into the Hele-Shaw cell. The possibly existing miniature air bubbles are taken care of by sit the suspension still to let the bubbles escape. In order to acquire a clean and clear visualization of each species of particle, we specifically choose the particle with smaller diameter ($D = 125 - 150\mu m$) to be fluorescent green while that has larger diameter ($D = 300 - 355\mu m$) comes in fluorescent red. The following Table 4.1 summarizes the experiments conducted, by gradually increasing the bulk concentration ϕ_{bulk}. The initially concentration of large particles takes the values of $1\%, 3\%, 5\%$ while that of small particle is adjusted accordingly to satisfy $\phi_{bulk} = \phi_{large} + \phi_{small}$.

We hereby report the following key observations from experiment. First of all, we observe similar fingering instability at the interface as in mono-disperse experiments. It still holds that, while keeping initial concentration of large particles ϕ_{large} constant, the interface remains circular while propagating outwards at relatively low bulk concentration

$D(\mu m)$	ϕ_{bulk}	$\phi_{large} + \phi_{small}$
125-150(green) & 300-355(red)	15%	$5\% + 10\%$
	16%	$1\% + 15\%, 3\% + 13\%$
	17%	$1\% + 16\%, 3\% + 14\%, 5\% + 12\%$
	18%	$1\% + 17\%, 3\% + 15\%$
	19%	$1\% + 18\%, 3\% + 16\%$
	20%	$1\% + 19\%, 3\% + 17\%, 5\% + 15\%$
	21%	$1\% + 20\%, 3\% + 18\%$
	22%	$1\% + 21\%$
	23%	$1\% + 22\%, 5\% + 18\%$
	24%	$1\% + 23\%$
	25%	$1\% + 24\%$
	30%	$5\% + 25\%$

Table 4.1: Experimental conditions tested; for all experimental runs, the flow rate Q and the gap thickness h are kept constant at 150 mL/min and 1.397mm, respectively. The experiments are carefully assessed to maintain the relationship $\phi_{bulk} = \phi_{large} + \phi_{small}$ before injection.

ϕ_{bulk}. The fingering phenomenon starts to initiate with the increase in ϕ_{bulk} and become more and more pronounced. Snapshots from experimental videos taken from same time are collected in the following Fig. 4.1, where the trend is very clearly shown.

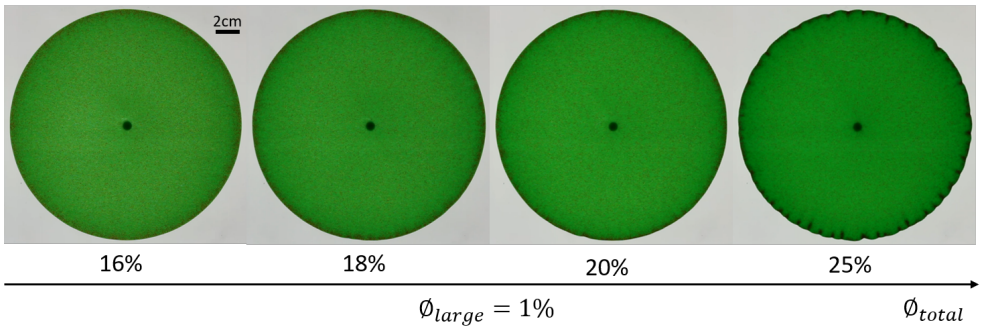

Figure 4.1: The dependence of fingering phenomenon on ϕ_{bulk} is clearly demonstrated that with increasing ϕ_{bulk} fingering initiates and grows more pronounced. All experiments are performed at gap thickness $h = 1.397mm$ and flow rate $Q = 150mL/min$.

Meanwhile, we notice that the interface may behave differently if we gradually change the concentration of large particles ϕ_{large} while keeping ϕ_{bulk} constant. It appears that the fingering phenomenon is possible to be induced at bulk concentrations where no finger is expected for mono-disperse counterpart by adding large particles. What's more, once the finger starts to occur, it becomes more and more pronounced with increasing large particle concentration, even though ϕ_{large} is kept small relative to ϕ_{bulk}. This trend is captured and summarized in the following Fig. 4.2.

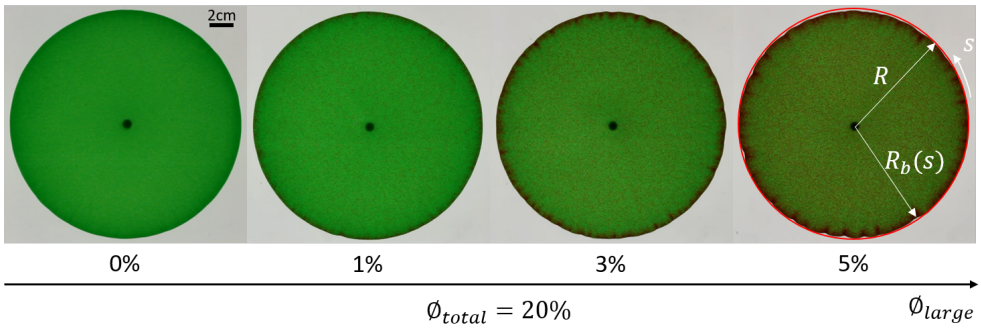

Figure 4.2: Induction of fingering phenomenon by adding small amount of large particles to the bulk suspension. It is clearly shown that the interface is stable for mono-disperse suspension with $\phi_0 = 20\%$. The fingering phenomenon also grows more and more pronounced as ϕ_{large} increases. All experiments are performed at gap thickness $h = 1.397mm$ and flow rate $Q = 150mL/min$.

The fact observed from experiments that the addition of small amount of large particles is able to induce fingering at bulk concentrations where fingering shouldn't occur for mono-disperse suspension is very surprising and interesting. We then perform further data analysis on available videos to investigate deeper into this trend. As shown in the last image in Fig. 4.2, we inherit the same strategy by following a curvilinear coordinate s and defining the best-fitted circle radius R and the instantaneous center-to-interface distance $R_b(s)$ respectively. According to Eq. 3.1, the Λ values are calculated for different

experiments.

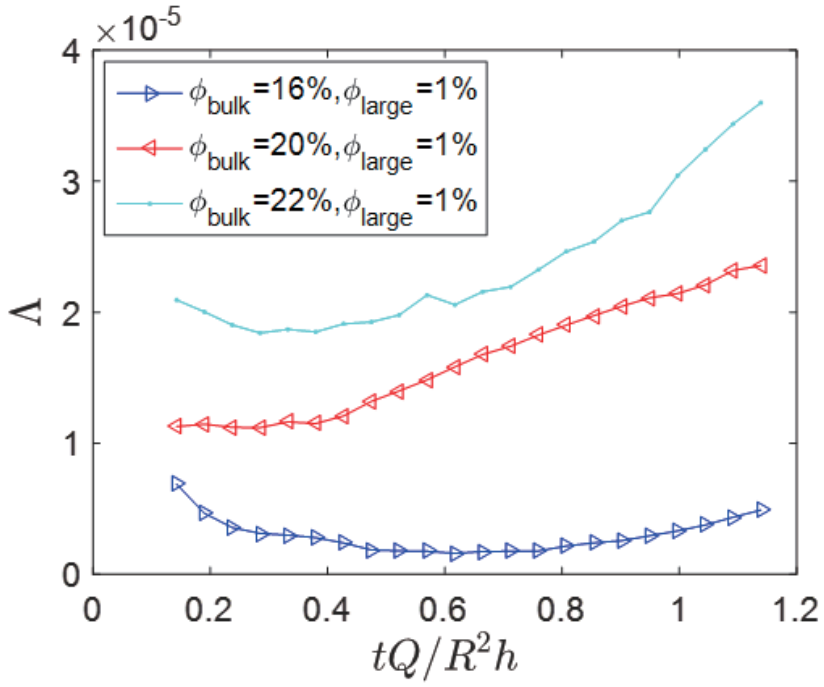

Figure 4.3: Comparison of Λ curves with different ϕ_{bulk}, where the large particle concentration is kept constant $\phi_{large} = 1\%$. The plot shows that when ϕ_{large} remains the same, larger ϕ_{bulk} leads to large Λ, which agrees with our observation that fingering grows more and more pronounced with increasing ϕ_{bulk}.

Fig. 4.3 shows the time-dependent Λ plots for experiments with constant $\phi_{large} = 1\%$ while ϕ_{bulk} is increasing. It can be seen that the magnitudes of the curve with higher ϕ_{bulk} also lyes on top of that corresponding to smaller ϕ_{bulk}, which is in agreement of our observation presented in Fig. 4.1. If we keep the bulk concentration ϕ_{bulk} as a constant and gradually increase $\phi_{large} = 1\%$, the corresponding magnitudes of Λ are observed to increase too, which is shown in Fig 4.4. We have also compared the Λ curves where ϕ_{bulk} is kept constant at 30%, as shown in Fig. 4.5. We find that not only the magnitude of Λ corresponding to the experiment where 5% of large particles are added to the bulk is larger,

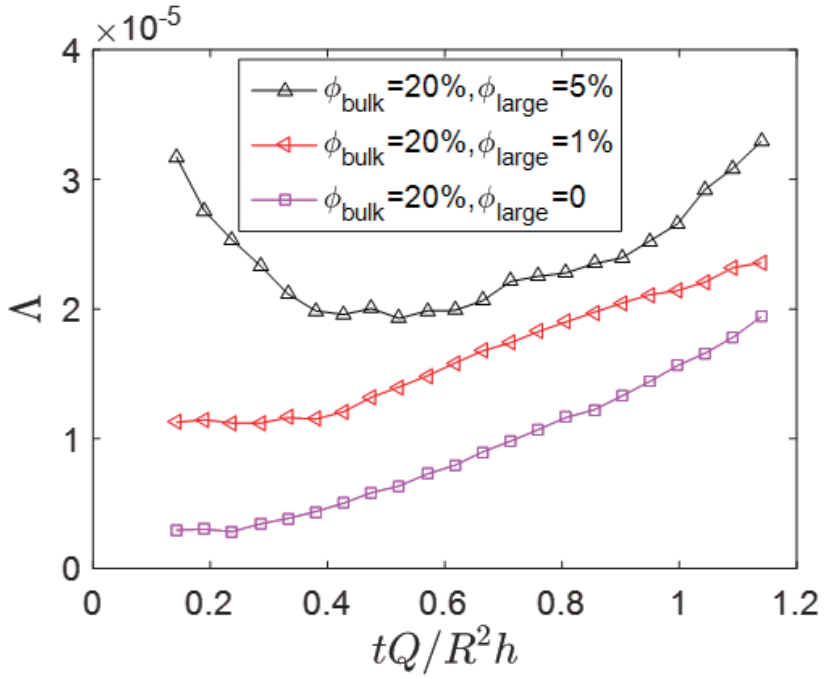

Figure 4.4: Comparison of Λ curves with different ϕ_{large}, where the bulk concentration is kept constant $\phi_{bulk} = 20\%$. The plot shows that when ϕ_{bulk} remains the same, larger ϕ_{large} leads to an increase in magnitude in Λ, which agrees with our observation that fingering grows more and more pronounced with increasing ϕ_{large} while keeping bulk concentration invariant.

we even see a peak in the curve, which is unique to *band fingering* at small h/D ratios for mono-disperse suspension. Again this difference in Λ plot confirms our observation in Fig. 4.2.

With all the analysis carried out so far, we put all the experiments on one phase diagram, by including also the mono-disperse suspension experiments conducted at same situation. As shown in Fig. 4.6, the presence of large particles results in a shift of the regimes, being that fingering happens at smaller ϕ_{bulk}. It can also be concluded that the higher ϕ_{large} is, the more significant the shift, or in other words, the earlier (in terms of ϕ_{bulk}) fingering will be observed.

Once again, we would like to confirm the particle accumulation with the depth-averaged

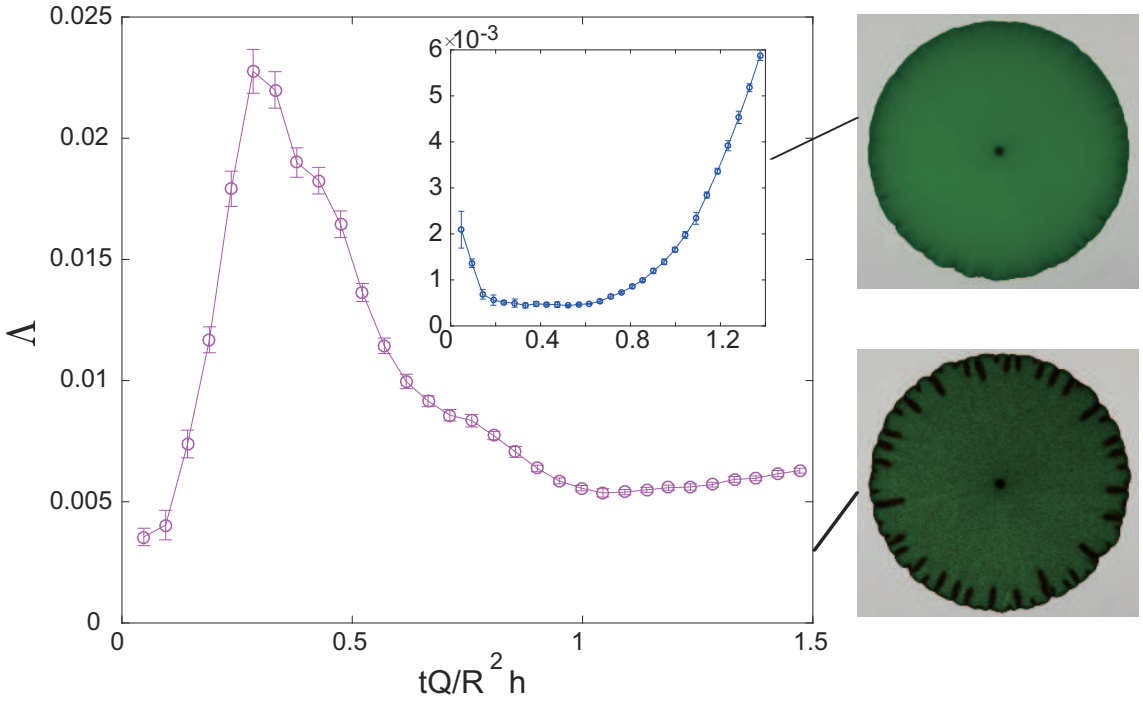

Figure 4.5: Comparison of Λ keeping $\phi_{bulk} = 30\%$. The inset plot corresponds to mono-disperse suspension where no large particle exists. The other curve represents the experiment with $\phi_{large} = 5\%$. The magnitude of Λ is much larger when large particle present and very surprisingly, we get the peak in the curve representing bi-disperse experiment, which previously is only observed in *band fingering* for mono-disperse suspension at small h/D ratios.

concentration profile $\bar{\phi}$ as a function of the radius r, for both the bulk suspension and the respective particle phase. The goal is accomplished utilizing the artificial neural network described in Sec. 2.2.4. We hereby present the concentration profiles for bulk suspension, large and small particles respectively in Fig. 4.7 for an experiment with initial $\phi_{bulk} = 21\%$ and $\phi_{large} = 1\%$. The plots are generated by evaluating the concentrations at different time (indicated in figure) after t_0, the starting point when suspension enters the cell. Clearly the concentration profiles are increasing in radial direction, which agrees with analysis. What's more, the variation of concentration for small particle (Fig. 4.7(b)) seems to be

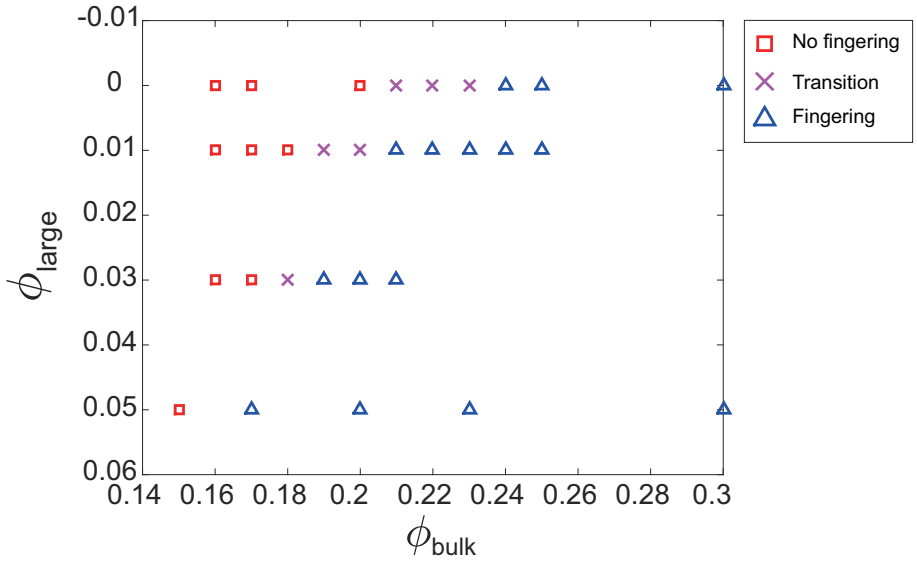

Figure 4.6: The phase diagram summarizing all experiments to show the effect on fingering instability of the presence of small fraction of large particle in bi-disperse suspension. The data points are classified into three regimes: "no fingering","transition" and "fingering". The diagram shows two facts: first the boundary concentrations between different regimes are shifted to left, indicating that fingering happens at smaller bulk concentration; second, an increase in large particle concentration while keeping bulk concentration constant triggers earlier onset of fingering.

relatively small while on the contrary, that of large particle (Fig. 4.7(c)) is notably big.

4.3 Theory

We believe that the key mechanism driving the fingering instability for mono-disperse suspension still holds even if we have extended our research to bi-disperse suspension. The mechanism of shear-induced migration results in the particles to collect near the centerline of the channel regardless of particle sizes, which then leads to a larger averaged velocity of particles than the bulk suspension. Moreover, we notice that the strength of shear-induced migration is proportional to the particle diameter squared, which means that the effect of shear-induced migration is much stronger on large particles than on small ones. We argue that the averaged velocity of large particles is larger than that of small particles as a result,

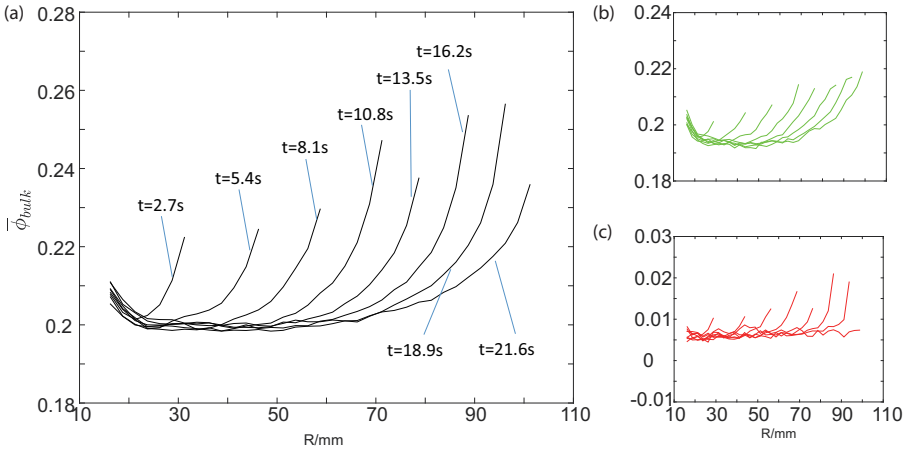

Figure 4.7: Concentration profiles acquired through image processing for an experiment with initial $\phi_{bulk} = 21\%$ and $\phi_{large} = 1\%$. Different curves correspond to times after the starting point t_0 when suspension enters the Hele-Shaw cell. The concentrations profiles remain relatively constant and then rise, indicating the accumulation of particles near interface. (a) The dependence of ϕ_{bulk} on R and t; (b) The dependence of ϕ_{small} on R and t; (c) The dependence of ϕ_{large} on R and t;

which gives the relative relationship between the magnitudes of $v_{large} > v_{small} > v_{bulk}$. The particles hence will accumulate near the interface with large one accumulate faster. The accumulation eventually leads to an increase in concentration, which correlates directly to the effective viscosity for suspension. Thus the fingering occurs due to the favorable viscosity contrast inside the suspension and propagates to eventually deform the interface. However, distinct from the mono-disperse case, we notice from experiment that fingering initiates at smaller bulk concentration, i.e., we observe fingering at concentrations where finger is not expected for mono-disperse suspension only by substituting a very small portion of small particles with large particles. Besides, an increase in large particle concentration while keeping bulk concentration constant triggers earlier onset of fingering. For example, at $\phi_{bulk} = 17\%$, no fingering is observed for experiments with ϕ_{large} up to 3% while fingering appears when ϕ_{large} continues to increase to 5%, see Fig. 4.6.

As mentioned in previous chapters, the shear induced migration far upstream leads to an enrichment of particles at the centerline, which subsequently results in the accumulation of particles near the interface, noticing that the enrichment brings a difference to velocities of suspension and particle and hence a net flux of particles. Though the large particle used in this research has a diameter $D = 350 - 355\mu m$ and a ratio $h/D = 4.5$, we argue that it is still acceptable to treat both particles as in continuum limit [94]. We thus employ the modified suspension balance model to account for a second species of particle to analyze why the presence of small amount of large particle brings a notable different to fingering instability.

We start with the governing equations for bulk suspension:

$$\nabla \cdot \boldsymbol{u} = 0 \tag{4.1}$$

$$\nabla \cdot \boldsymbol{\Sigma} = 0 \tag{4.2}$$

For particles, there are governing equation for each species of particle,

$$\frac{\partial \phi_i}{\partial t} + \nabla \cdot (\phi_i \boldsymbol{u}_i^p) = 0 \tag{4.3}$$

$$\nabla \cdot \boldsymbol{\Sigma}_i^p + \boldsymbol{F}_i = 0 \tag{4.4}$$

where $\boldsymbol{u}$ and $\boldsymbol{\Sigma}$ represent velocity vector and stress tensor respectively, the superscript p indicates those terms are for particulate phases and the subscript i takes the values of $i = 1, 2$, corresponding to two different species of particles. The inner drag force F_i is given as:

$$\boldsymbol{F}_i = -\frac{9\eta_l}{2a_i^2}\frac{\phi_i}{f(\phi)}(\mathbf{u}_i^p - \mathbf{u}) \tag{4.5}$$

with the hindrance function $f(\phi) = (1-\phi)^{4.4}$. It is worth mentioning that all the above governing equations will be considered in cylindrical coordinate to accommodate our ge-

ometry considered in experiment. The velocities $\boldsymbol{u}$ and $\boldsymbol{u^p}$ thus consist of components in r, θ, z directions.

The suspension and particulate phase are coupled through the constitutive relationships of the stress tensors,

$$\boldsymbol{\Sigma}_i^p = 2\eta_l \hat{\eta_{p_i}} \boldsymbol{E} + \boldsymbol{\Sigma}_{n_i}^p \tag{4.6}$$

$$\boldsymbol{\Sigma} = -p\boldsymbol{I} + 2\eta_l \boldsymbol{E} + \boldsymbol{\Sigma}_1^p + \boldsymbol{\Sigma}_2^p \tag{4.7}$$

with the empirical expressions for particulate viscosity $\hat{\eta}_{p_i} = (\hat{\eta}_s - 1)\frac{\phi_i}{\phi}$, shear viscosity $\hat{\eta}_s = (1 + \frac{\alpha\phi}{1-\frac{\phi}{\phi_m}})^{3.3\phi_m}$ and normal viscosity $\hat{\eta}_n = (\frac{\phi}{\phi_m})^2 K_n \hat{\eta}_s$.

In analogous to the mono-disperse model, it is reasonable to assume a steady state flow so that $\boldsymbol{u} - \boldsymbol{u}^p = 0$ in the upstream region. Thus both the governing equations for particulate phase reduce to $\nabla \cdot (\phi_i \boldsymbol{u}_i^p) = 0$ and $\nabla \cdot \boldsymbol{\Sigma}_i^p = 0$. The governing equations will further be reduced to the following form in lubrication limit ($\frac{\partial}{\partial r} \ll \frac{\partial}{\partial z}$) and axisymmetric assumption ($\frac{\partial}{\partial \theta} = 0$),

$$\frac{\partial}{\partial z}(-\hat{\eta}_n \dot{\gamma} \frac{\phi_i}{\phi}) = 0 \tag{4.8}$$

where the shear rate $\dot{\gamma} = du_r/dz$ in lubrication limit. Similarly, under same assumption, the governing equations for bulk suspension reduces to,

$$\frac{\partial P}{\partial r} = \frac{\partial}{\partial z}(\hat{\eta}_s \frac{\partial u_r}{\partial z}) \tag{4.9}$$

$$\frac{\partial P}{\partial z} = 0 \tag{4.10}$$

Thus By rearranging terms and combining the equations, we have the following ordi-

nary differential equation (ODE),

$$\frac{\eta_n}{\eta_s}\frac{\phi_i}{\phi}z = (\eta_n\dot{\gamma}\frac{\phi_i}{\phi})(\frac{\partial P}{\partial r}) = const \tag{4.11}$$

which is numerically solvable subject to the following constraints,

$$Q = \int_{-\frac{h}{2}}^{\frac{h}{2}} u_r dz \tag{4.12}$$

$$Q\phi_{0i} = \int_{-\frac{h}{2}}^{\frac{h}{2}} u_{ri}\phi_i dz \tag{4.13}$$

However, we note that the equations are highly coupled, especially when considering the concentration profiles under the relation of $\phi = \phi_1 + \phi_2$, which makes it extremely complicated to solve directly. There are two ways to overcome this coupling in equation. The first method is by assuming that the contribution of one phase of particle to the bulk is considerably small, which mathematically means $\phi = \phi_1 + \delta\phi_2$ with $\delta \ll 1$. There is no specific reason in choosing the contribution of ϕ_2 to be small, the relation can be revised the other way to indicate the contribution of ϕ_1 is small. This choice won't effect the solving process after all since the subscripts are purely dummy indicators. Another approach is numerically even easier for the system to be solved, where we assume the concentration of small particles ϕ_{small} to be constant. This assumption follows the work by Leal *et al* [42], in which they measured the concentration profile of small particle across the gap and found it barely changes in z direction while there is a clear increase toward centerline in concentration for large particles. They concluded that for relatively dilute bi-disperse suspensions ($\phi_{bulk} < 40\%$), it is acceptable to treat small particle as a background phase that effects nothing more than the effective viscosity of carrying fluid. Besides, their calculation based on mono-disperse suspension balance model under the $\phi_{small} = const$ assumption receive satisfactory agreement with experimental measurements. In this

research, we apply the second approach to numerically solve the ODE for ϕ, u etc.

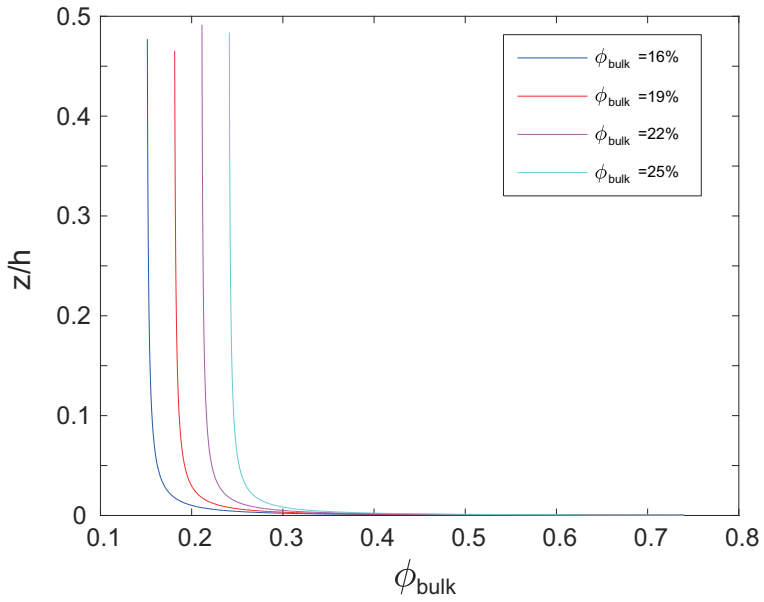

Figure 4.8: Bulk concentration profile at different initial ϕ_{bulk} while keeping large particle concentration $\phi_{large} = 1\%$.

Fig. 4.8 shows our calculation result of bulk concentration profile at different initial ϕ_{bulk} while keeping $\phi_{large} = 1\%$. The increasing trend in ϕ_{bulk} from wall to centerline confirms our analysis that the particle are undergoing shear induced migration, which leads to the enrichment of particles in the middle of channel. The concentration profile of large particles will take similar shape, given that one only needs to subtract the respective uniform small particle concentration from the those shown in Fig. 4.8. The velocity profile utilizing exact the same parameters is shown in Fig. 4.9. It is very surprising for us to see that the velocity profiles are almost identical at different ϕ_{bulk} while keeping ϕ_{large} constant. We do still observe the bluntness in velocity profile[34, 42, 94] near the centerline

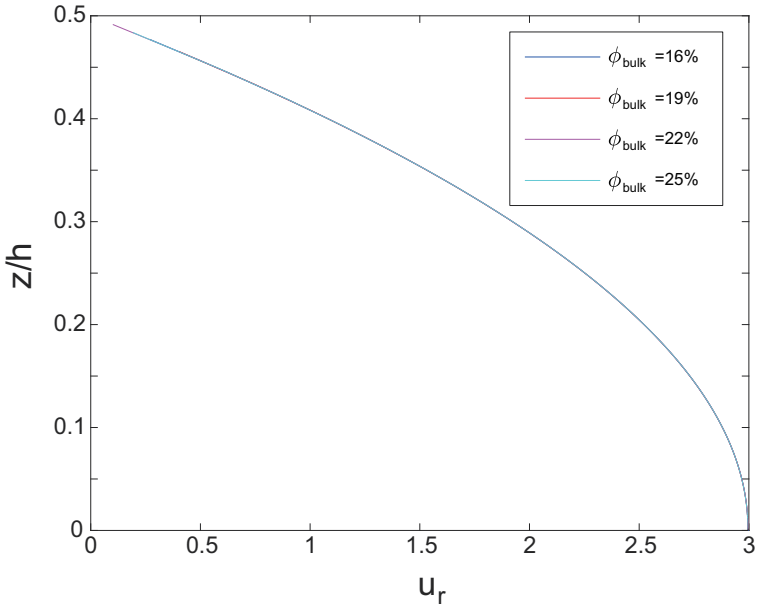

Figure 4.9: Bulk suspension velocity profile at different initial ϕ_{bulk} while keeping large particle concentration $\phi_{large} = 1\%$.

The concentration profiles are then used to calculate the depth-averaged concentrations $\bar{\phi}$ for both the bulk suspension and the large particle phase, which is then compared with those values acquired from experiments. Fig. 4.10 shows the comparison of depth averaged concentration between experiments $\bar{\phi}_{exp}$ and theoretical calculation $\bar{\phi}$ for $\phi_{large} = 1\%$, 3% and 5% respectively. It appears that the calculated depth-average concentration values for bulk concentration is in very good agreement with those acquired from experiments.

On the other hand, we also notice from Fig. 4.10 that the depth averaged concentrations of large particles do not depend on the bulk concentration ϕ_{bulk} as long as the initial large particle concentration ϕ_{large} is constant. Inspired by this observation, we then proceed to calculate the net flux of large particles in the upstream region, which is defined as follows,

$$D = \int_{-h/2}^{h/2} \phi(z)u(z)dz \tag{4.14}$$

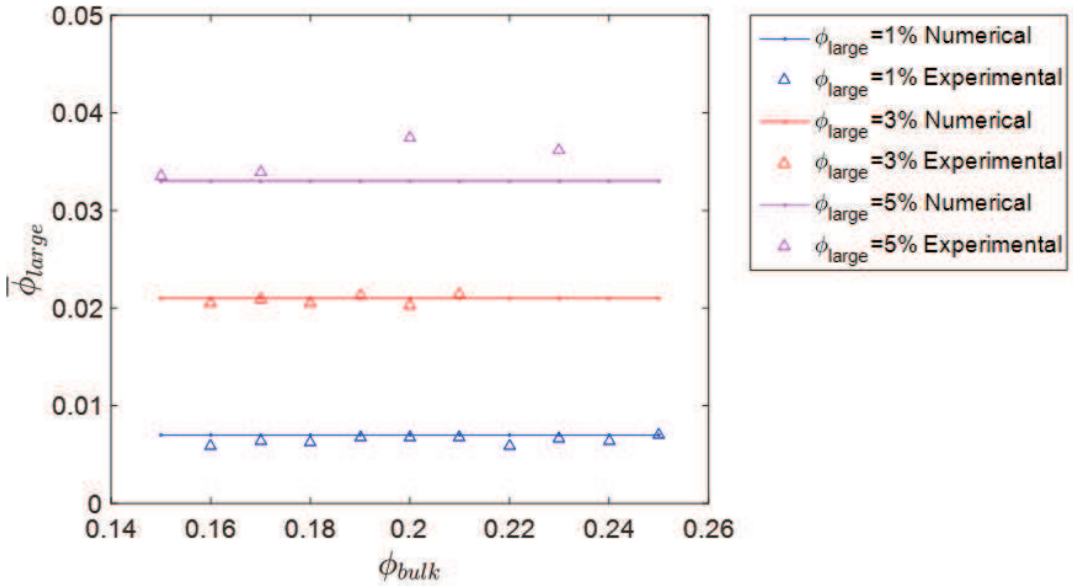

Figure 4.10: Comparison of depth-averaged $\bar{\phi}$ for large particles between numerical calculation and image processing. The results show that the theoretical calculation agrees quite well with experiment.

where $\phi(z)$ and $u(z)$ are the concentration and velocity profiles for either large particle or bulk suspension calculated from our model.

The results from flux calculation is shown in Fig. 4.11. It appears that at fixed large particle concentration ϕ_{large}, the flux remains constant over increasing bulk concentration ϕ_{bulk}, indicating the independence of flux on ϕ_{bulk}. The flux increases however with large particle concentrations while fixing the bulk concentration, being that the larger ϕ_{large}, the larger the flux. If we apply the simple mass conservation law in the upstream region, as shown in Fig. 4.12, we have the following equation for large particles

$$Q\phi_0 = \frac{\partial}{\partial t}(\pi R_{in}^2 \bar{\phi}_{large} h) + \int_{-h/2}^{h/2} \phi_{large}(z) u_{large}(z) dz \tag{4.15}$$

where Q is the flow rate, ϕ_0 is the initial large particle concentration, R_{in} is the radius of the boundary of the upstream region. According the the above equation, it is easy to

conclude that R_{in} should be independent on ϕ_{bulk} as long as the large particle concentration ϕ_{large} is kept invariant.

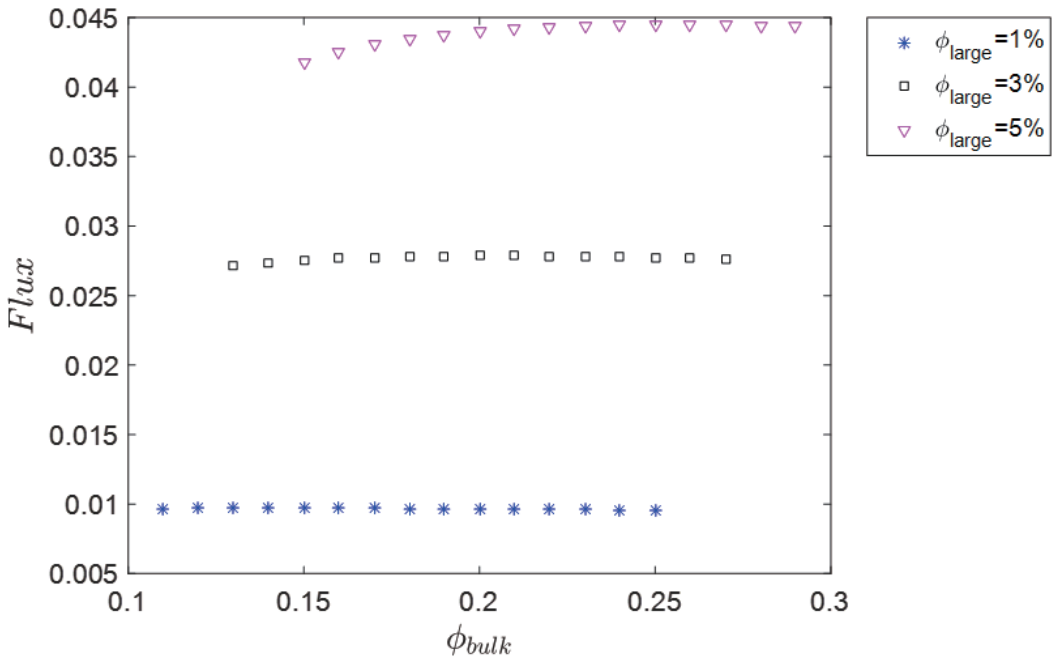

Figure 4.11: The change in net flux of bulk suspension as a function of ϕ_{bulk} at various ϕ_{large}. The net flux increases with the increase of ϕ_{large} while remain constant for increasing ϕ_{bulk} with ϕ_{large} kept constant.

In order to verify the dependence of R_{in} on ϕ_{bulk}, we examine the concentration profiles acquired from experiments. Similar to the mono-disperse case, we note that the concentration profiles still collapse on a single curve if we normalize the radius. There is a region in the concentration profile where the particle distribution is fairly uniform, or say, the concentration profile is flat. As mentioned previously, our analysis is valid far upstream of the interface, which corresponds to flat region of the concentration profile, as shown in Fig. 4.12. By extracting the radii corresponding to the turning points in concen-

tration profiles, we are able to get the experimental measures of R_{in} and plot them as a function of bulk concentration ϕ_{bulk}, which is shown in Fig. 4.13. The plot shows that the values of R_{in} increases over time but remain constant at the same time even if the bulk concentration ϕ_{bulk} increase, which is exactly as predicted by our analysis from Eq. 4.15.

4.4 Conclusion and Future Work

In summary, we present in this chapter particle-induced fingering for bi-disperse suspension, where a mixture of two species of neutrally buoyant particles with different diameter are mixed with oil and injected radially into a Hele-Shaw cell. As an extension of the work where we experimentally and theoretically quantify the fingering instability induced by particles observed in mono-disperse suspension, we report that similar fingering phenomenon are still observed. Like mono-disperse cases, fingering is not observed in all bulk concentration ϕ_{bulk}. It initiates as we gradually increase ϕ_{bulk} and becomes more and more pronounced as ϕ_{bulk} gets bigger. More interestingly, we find that the addition of small amount of large particles to bulk suspension will result in an early occurrence of fingering compared to mono-disperse experiments under exactly the same conditions. We carry out rigorous experiments to quantify the critical ϕ_{bulk} at which fingering appears by measuring the interface deformation, which is described by Λ. Different series of experiments with increasing amount of large particle are performed, where we always see the early initiation of fingering. Both the depth-averaged bulk concentration and the respective particle concentration are measured experimentally utilizing an artificial neural network to classify different particles by color (RGB values). The concentration profiles clearly indicate the accumulation of particles near the interface, which is in agreement with our analysis on fingering mechanism.

We carry out theoretical work utilizing the suspension balance model which is modified to accommodate the existence of a second species of particle. We argue that the sus-

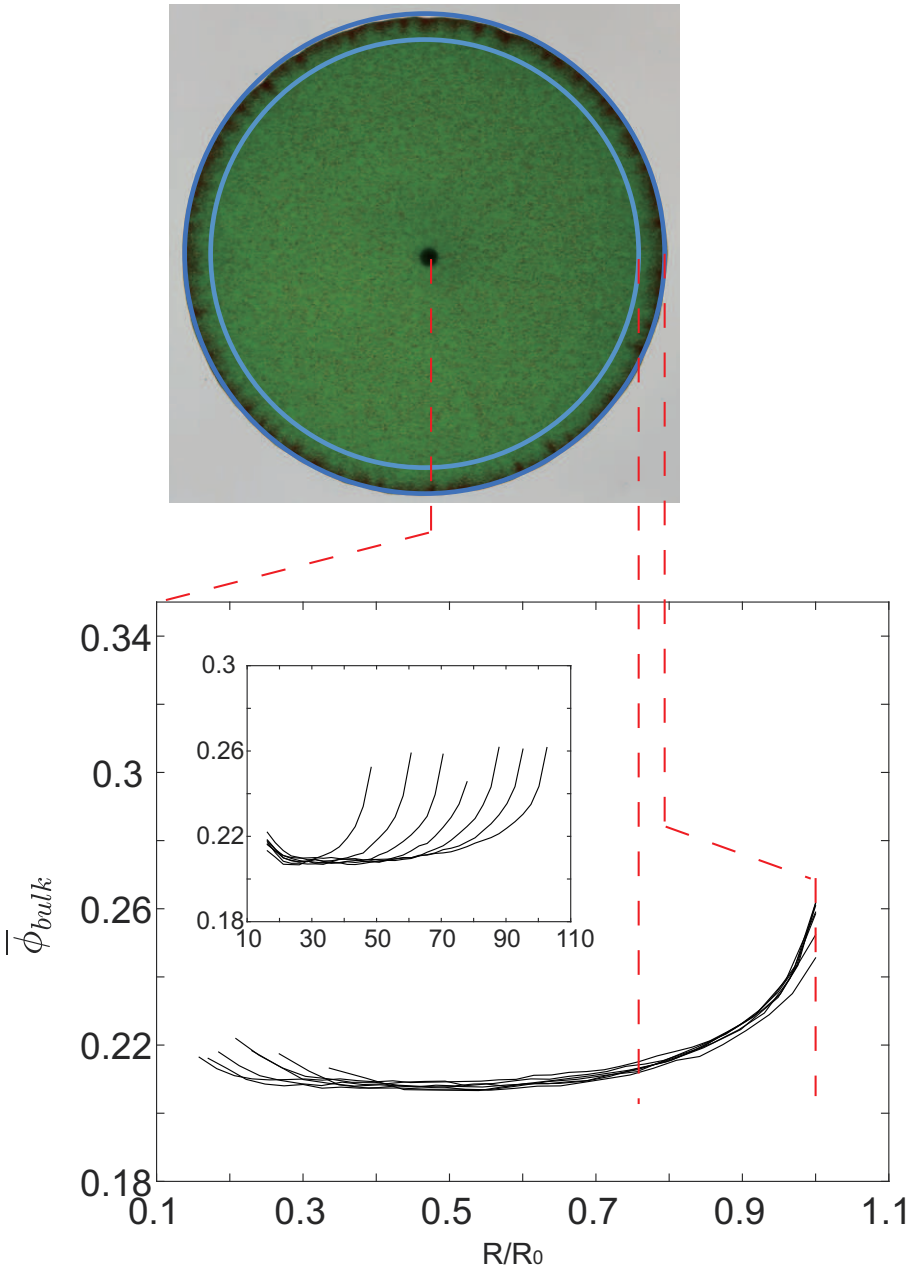

Figure 4.12: The collapse of concentration profile, data taken from experiment where $\phi_{bulk} = 22\%$ and $\phi_{large} = 1\%$. The flat part of the concentration corresponds to the upstream region we are interested in while the rapidly rising part corresponds to the region near the interface, where accumulation is most significant.

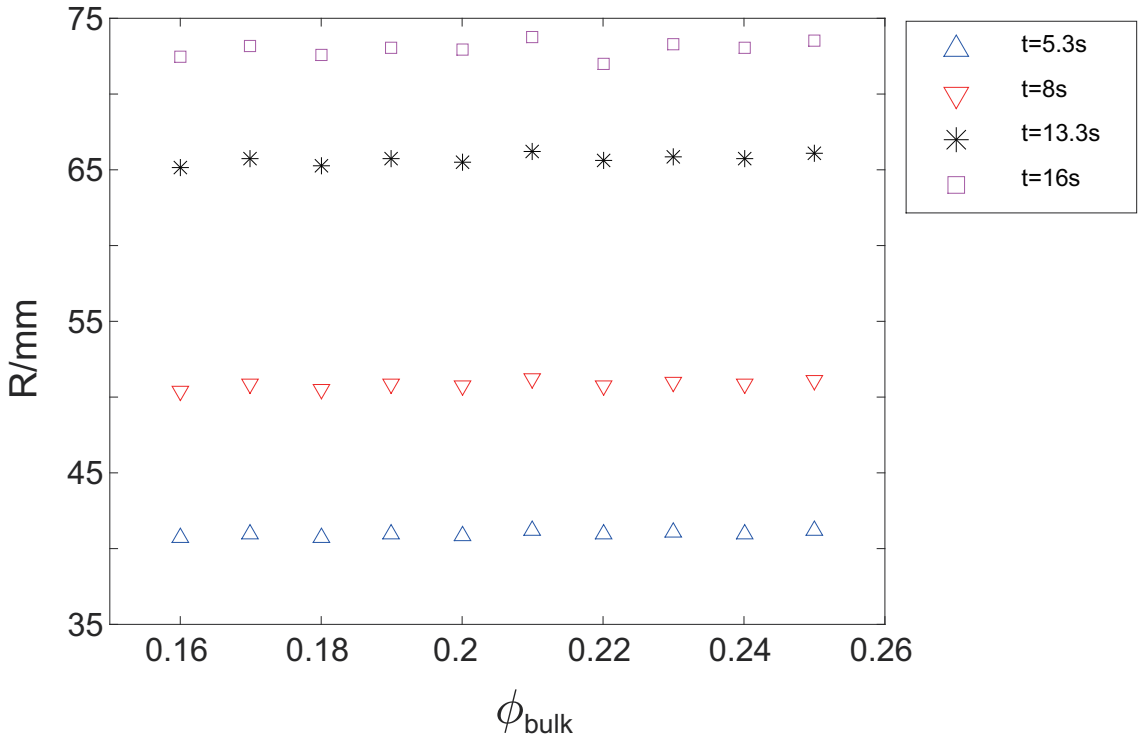

Figure 4.13: The radius at which concentration starts to rise acquired from experiments with different initial ϕ_{bulk} but identical $\phi_{large} = 1\%$. The turning radius doesn't depend on ϕ_{bulk} but increase with time in one experimental run.

pension balance model is still valid even though for large particles used in this research, the gap thickness over particle diameter ratio h/D falls in a dangerous region where the continuum assumption may break. Our theoretical modeling is performed far upstream of the interface where we can reasonably assume a fully-developed, unidirectional flow.The model is motivated by our belief that the shear-induce migration, which successfully explain our observations for mono-disperse suspension, is still the key driving mechanism even if we have extended to bi-disperse suspension. We have calculated the depth-averaged concentration for large particles, assuming a uniform distribution of small particles in the background [42]. The concentrations calculated match perfectly with our experimental measurements. We find that for fixed initial ϕ_{large}, the depth averaged concentration is

relatively invariant, regardless of the bulk concentration. Further calculation for net flux of large particles indicates an invariance in flux for fixed large particle concentrations, utilizing the concentration and velocity profiles acquired. Combining the invariance of the flux at fixed ϕ_{large} and simple mass conservation law, we expect the radius of the boundary for the upstream region to be independent on ϕ_{bulk}. The independence is further verified by our experimental observations by carefully examine the concentration profiles.

Although the addition of large particles to the bulk suspension brings us new observations, it still share similarity with fingering induced by the particles in mono-disperse suspension. In both case of scenario, the fingering induced by particles is driven by the viscosity difference brought by the accumulation of particles inside of the suspension. Meanwhile, the "de-fingering" also happens for bi-disperse suspension at the interface, since there always exist a huge difference in viscosity between the suspension at interface and the air, regardless of whether it is mono- or bi-disperse. This competition happening in the near-interface region between fingering and "de-fingering" could bring effects like the split of fingers, which is worthy investigating as future work. Besides, it appears that there is a difference in the number of fingers or wave length between bi-disperse suspension and mono-disperse suspensions. What's more, the role of the clusters formed inside of the suspension is never well appreciated, which could also be part of future work. We would love to see what changes will it make if we manipulate the size ratio of the particles D_1/D_2 and repeat current experiments, since the ratio is kept at roughly 2.4 as a constant.

5. SUMMARY AND REMARKS

In this research, we rigorously study the particle-induced viscous fingering that occurs in the migration of suspensions in a Hele-Shaw cell, both experimentally and theoretically.

We first study the fingering phenomenon for mono-disperse suspensions, which is prepared by mixing particles of the same size with silicone oil. We have constructed our own experimental setup, which consists of the flow and imaging systems. The experiments are performed by injecting suspensions into the Hele-Shaw cell while recording with a digital camera from top down. Complete series of experiments are conducted by varying the particle concentration ϕ and the ratio h/D, where h is the gap thickness of the cell and D is the diameter of particles. We observe that the outward expanding suspension maintains a circular and stable interface at low concentrations and fingering starts to initiate when the concentration increases to given values. The transient concentration is found to be dependent on h/D and thus different for different series of experiments. We also observe that, when h/D is quite small, there is a unique phenomenon called 'band fingering', in which a thick band of particles forms first on the interface and then breaks up leading to very pronounced fingering. Image processing technologies are used to aid our understanding of the fingering instability. We are able to measure the depth-averaged concentration profiles in the radial direction from experimental data.

Physically, the fingering mechanism is explained by the mechanism of shear induced migration, which causes particles to migrate towards and gather near the channel centerline. This results in the averaged velocity of particles to be larger than that of the bulk suspension. The velocity difference makes it possible for particles to eventually catch up to the expanding interface and accumulate there. This accumulation of particles gives an increasing profile of particle concentration in the radial direction and hence an increasing

profile of the effective viscosity. Due to the unfavorable viscosity contrast, miscible fingering initiates inside the suspension and eventually deforms the interface. We implement the suspension balance model to validate the particle migration upstream of the interface. We confirm the effects of shear induced migration of particles by numerically evaluating our model.

The project is then extended by replacing the mono-disperse suspension with bi-disperse one, which contains particles of two different sizes. We again perform series of experiments by varying the bulk concentrations and the respective concentrations of each species of particles. We observe that fingering still occurs when the bulk particle concentration is increased to given values and grows more pronounced as the bulk concentration continues to increase. Very surprisingly, we also find that the addition of small amount of large particles into the suspension leads to an earlier onset of fingering compared to the mono-disperse counterpart. The image processing techniques developed for first part of this research are used to perform data analysis. To find the concentration profiles for each species of particle, an artificial neural network is developed to classify the particles base on the color difference on pixel level.

The suspension balance model is modified by introducing governing equations and extra terms in particulate stress to account for the existence of a second species of particles. The model is solved numerically and the depth-averaged concentrations acquired agree well with our experimental measurements. We also notice that the predicted depth averaged concentrations of large particles stay invariant even if the bulk concentration increases, as long as the initial large particle concentration is fixed. Further calculations of net flux in the upstream region for large particles show that the flux is also independent of the bulk concentration when the initial large particle concentrations are kept constant. As a result, we expect the radius at which the large particle concentration starts to increase rapidly remain invariant regardless of the bulk concentrations as long as the initial large

particle concentration is the same. This trend is confirmed by the experimental measurements through detailed examination of the concentration profiles.

Despite the rich literature of the suspension migration, it remains an active research area. In comparison, the interfacial instability driven by particle migration has drawn much less attention. In particular, the particle induced viscous fingering in bi-disperse suspensions reported in this research is non-existent in the literature to the best of the author's knowledge. We provide quantitatively analysis both experimentally and theoretically for this fingering instability and receive satisfactory results. Though there are interesting unanswered questions, for example the formation of patterns, or the mechanism that sets the wave number of fingers, we believe our research has successfully captured the essence of the rich physics. We hereby hope this research could shed light on this interesting and exciting topic and provide vision for continued research.

REFERENCES

[1] K. V. Cashman and R. S. J. Sparks, "How volcanoes work: A 25 year perspective," *GSA Bulletin*, vol. 125, no. 5-6, p. 664, 2013.

[2] B. Voight, R. S. J. Sparks, A. D. Miller, R. C. Stewart, R. P. Hoblitt, A. Clarke, J. Ewart, W. P. Aspinall, B. Baptie, E. S. Calder, P. Cole, T. H. Druitt, C. Hartford, R. A. Herd, P. Jackson, A. M. Lejeune, A. B. Lockhart, S. C. Loughlin, R. Luckett, L. Lynch, G. E. Norton, R. Robertson, I. M. Watson, R. Watts, and S. R. Young, "Magma flow instability and cyclic activity at Soufriere Hills Volcano, Montserrat, British West Indies," *Science*, vol. 283, no. 5405, pp. 1138–1142, 1999.

[3] D. Huh, H. Fujioka, Y.-C. Tung, N. Futai, R. Paine, J. B. Grotberg, and S. Takayama, "Acoustically detectable cellular-level lung injury induced by fluid mechanical stresses in microfluidic airway systems," *Proceedings of the National Academy of Sciences*, vol. 104, no. 48, pp. 18886–18891, 2007.

[4] J. B. Grotberg, , and O. E. Jensen, "Biofluid mechanics in flexible tubes," *Annual Review of Fluid Mechanics*, vol. 36, no. 1, pp. 121–147, 2004.

[5] G. M. Homsy, "Viscous fingering in porous media," *Annual Review of Fluid Mechanics*, vol. 19, no. 1, pp. 271–311, 1987.

[6] T. Maxworthy, "The nonlinear growth of a gravitationally unstable interface in a Hele-Shaw cell," *Journal of Fluid Mechanics*, vol. 177, pp. 207–232, 1987.

[7] C. Gin and P. Daripa, "Stability results for multi-layer radial Hele-Shaw and porous media flows," *Physics of Fluids*, vol. 27, no. 1, p. 012101, 2015.

[8] T. T. Al-Housseiny, P. A. Tsai, and H. A. Stone, "Control of interfacial instabilities using flow gerometry," *Nature Physics*, vol. 8, pp. 747–750, 2012.

[9] D. Pihler-Puzović, P. Illien, M. Heil, and A. Juel, "Suppression of complex finger-like patterns at the interface between air and a viscous fluid by elastic membranes," *Physical Review Letters*, vol. 108, p. 074502, Feb 2012.

[10] Z. Zheng, H. Kim, and H. A. Stone, "Controlling viscous fingering using time-dependent strategies," *Physical Review Letters*, vol. 115, p. 174501, Oct 2015.

[11] A. Lindner, D. Bonn, E. C. Poire, M. B. Amar, and J. Meunier, "Viscous fingering in non-Newtonian fluids," *Journal of Fluid Mechanics*, vol. 469, pp. 237 – 256, 2002.

[12] P. Tordjeman, "Saffman-Taylor instability of shear thinning fluids," *Physics of Fluids*, vol. 19, p. 118102, 2007.

[13] D. H. Vlad and J. V. Maher, "Tip-splitting instabilities in the channel Saffman-Taylor flow of constant viscosity elastic fluids," *Physical Review E*, vol. 61, pp. 5439 – 5444, 2000.

[14] D. A. Reinelt, "The primary and inverse instabilities of directional viscous fingering," *Journal of Fluid Mechanics*, vol. 285, pp. 303–327, 1995.

[15] E. Ben-Jacob, H. Shmueli, O. Shochet, and A. Tenenbaum, "Adaptive self-organization during growth of bacterial colonies," *Physica A: Statistical Mechanics and its Applications*, vol. 187, no. 3, pp. 378 – 424, 1992.

[16] A. K. McAllister, "Cellular and molecular mechanisms of dendrite growth," *Cerebral Cortex*, vol. 10, no. 10, pp. 963–973, 2000.

[17] C. Clanet and G. Searby, "First Experimental Study of the Darrieus-Landau Instability," *Physical Review Letters*, vol. 80, pp. 3867–3870, Apr. 1998.

[18] D. VELLA, P. D. METCALFE, and R. J. WHITTAKER, "Equilibrium conditions for the floating of multiple interfacial objects," *Journal of Fluid Mechanics*, vol. 549, pp. 215–224, 2006.

[19] S. U. Pickering, "CXCVI.-emulsions," *Journal of Chemical Society, Transactions*, vol. 91, pp. 2001–2021, 1907.

[20] P. Aussillous and D. Queue, "Liquid marbles," *Nature*, vol. 411, pp. 924–927, 2001.

[21] M. Trojer, M. L. Szulczewski, and R. Juanes, "Stabilizing fluid-fluid displacements in porous media through wettability alteration," *Physical Review Applied*, vol. 3, p. 054008, May 2015.

[22] I. Bihi, M. Baudoin, J. E. Butler, C. Faille, and F. Zoueshtiagh, "Inverse Saffman-Taylor experiments with particles lead to capillarity driven fingering instabilities," *Physical Review Letters*, vol. 117, p. 034501, Jul 2016.

[23] G. K. Batchelor and J. T. Green, "The determination of the bulk stress in a suspension of spherical particles on order c^2," *Journal of Fluid Mechanics*, vol. 56, pp. 401–427, 1972.

[24] F. Gadala-Maria and A. Acrivos, "Shear-induced structure in a concentrated suspension of solid spheres," *Journal of Rheology*, vol. 24, p. 799, 1980.

[25] R. L. Hoffman, "Discontinuous and dilatant viscosity behavior in concentrated suspensions. I. observation of a flow instability," *Journal of Rheology*, vol. 16, p. 155, 1972.

[26] D. Leighton and A. Acrivos, "The shear-induced migration of particles in concentrated suspensions," *Journal of Fluid Mechanics*, vol. 181, pp. 415–439, 1987.

[27] J. R. Abbott, N. Tetlow, A. L. . Graham, S. A. Altobelli, E. Fukushima, L. A. Mondy, and T. Stephens, "Experimental observations of particle migration in concentrated suspensions: Couette flow," *Journal of Rheology*, vol. 35, p. 773, 1991.

[28] A. M. Corbett, R. J. Phillips, and R. J. Kauten, "Magnetic resonance imaging of concentration and velocity profiles of pure fluids and solid suspensions in rotating geometries," *Journal of Rheology*, vol. 39, p. 907, 1995.

[29] A. A. Altobelli, R. C. Givler, and E. Fukushima, "Velocity and concentration measurements of suspensions by nuclear magnetic resonance imaging," *Journal of Rheology*, vol. 35, p. 721, 1991.

[30] A. Karnis and S. G. Mason, "The flow of suspensions through tubes IV. meniscus effects," *Journal of Colloid Interface Science*, vol. 23, pp. 120 – 133, 1967.

[31] B. K. Chapman, *Shear-induced migration phenomena in concentrated suspensions*. PhD thesis, University of Notre Dame, 1990.

[32] R. E. Hampton, A. A. Mammoli, A. L. Graham, and N. Tetlow, "Migration of particles undergoing pressure-driven flow in a circular conduit," *Journal of Rheology*, vol. 41, p. 621, 1997.

[33] C. J. Koh, P. Hookham, and L. G. Leal, "An experimental investigation of concentrated suspension flows in a rectangular channel," *Journal of Fluid Mechanics*, vol. 266, pp. 1–32, 1994.

[34] M. L. Lyon and L. G. Leal, "An experimental study of the motion of concentrated suspensions in two-dimensional channel flow. Part 1. Monodisperse systems," *Journal of Fluid Mechanics*, vol. 363, pp. 25–56, 1998.

[35] S. Lee, Y. Stokes, and A. Bertozzi, "Behavior of a particle-laden flow in a spiral channel," *Physics of Fluids*, vol. 26, p. 043302, 2014.

[36] N. Murisic, J. Ho, V. Hu, P. Latterman, T. Koch, K. Lin, M. Mata, and A. Bertozzi, "Particle-laden viscous thin-film flows on an incline: Experiments compared with a

theory based on shear-induced migration and particle settling," *Physica D: Nonlinear Phenomena*, vol. 240, no. 20, pp. 1661 – 1673, 2011.

[37] J. Zhou, B. Dupuy, A. L. Bertozzi, and A. E. Hosoi, "Theory for shock dynamics in particle-laden thin films," *Physical Review Letters*, vol. 94, p. 117803, Mar 2005.

[38] N. Murisic, B. Pausader, D. Peschka, and A. L. Bertozzi, "Dynamics of particle settling and resuepension in viscous liquid films," *Journal of Fluid Mechanics*, vol. 717, pp. 203–231, 2013.

[39] G. Krishnan and D. T. L. Jr, "Shear-induced size segregation phenomena in bidisperse suspensions," *Applied Mechanics Reviews*, vol. 47, no. 6, pp. S236 – S239, 1994.

[40] A. L. Graham, S. A. Altobelli, E. Fukushima, L. A. Mondy, and T. S. Stephen, "Note: NMR imaging of shear-induced diffusion and structure in concentrated suspensions undergoing Couette flow," *Journal of Rheology*, vol. 135, pp. 191 – 201, 1991.

[41] D. M. Husband, L. A. Mondy, E. Ganani, and A. L. Graham, "Direct measurements of shear-induced particle migration in suspensions of bimodal spheres," *Rheologica Acta*, vol. 33, pp. 185 – 192, 1994.

[42] M. K. Lyon and L. G. Leal, "An experimental study of the motion of concentrated suspensions in two-dimensional channel flow. Part 2. Bidisperse systems," *Journal of Fluid Mechanics*, vol. 363, pp. 57 – 77, 1998.

[43] J. T. . Norman, B. O. Oguntade, and R. T. Bonnecaze, "Particle-phase distributions of pressure-driven flows of bidisperse suspensions," *Journal of Fluid Mechanics*, vol. 594, pp. 1 – 28, 2008.

[44] D. Semwogerere and E. R. Weeks, "Shear-induced particle migration in binary colloidal suspensions," *Physics of Fluids*, vol. 20, p. 043306, 2008.

[45] H. M. Vollebregt, R. G. M. van der Sman, and R. M. Boom, "Model for particle migration in bidisperse suspensions by use of effective temperature," *Faraday Discuss*, vol. 158, pp. 89 – 103, 2012.

[46] D. Leighton and A. Acrivos, "Measurement of shear-induced self-diffusion in concentrated suspensions of spheres," *Journal of Fluid Mechanics*, vol. 177, pp. 109–131, 1987.

[47] A. Ramachandran and D. T. L. Jr., "The infuence of secondary flows induced by normal stess differences on the shear-induced migration of particles in concentrated suspensions," *Journal of Fluid Mechanics*, vol. 603, pp. 207–243, 2008.

[48] R. C. A. R. J. Phillips, R. A. Brown, A. L. Graham, and J. R. Abbott, "A constitutive model for concentrated suspensions that accounts for shear-induced particle migration.," *Physics of Fluids A*, vol. 4, pp. 30–40, 1992.

[49] G. P. Krishnan, S. Beimfohr, and D. T. Leighton, "Shear-induced radial segregation in bidisperse suspensions," *Journal of Fluid Mechanics*, vol. 321, pp. 371–393, 1996.

[50] K. Zhang and A. Acrivos, "Viscous resuspension in fully developed laminar pipe flows," *International Journal of Multiphase Flow*, vol. 20, pp. 579 – 591, 1994.

[51] A. Shauly, A. Wachs, and A. Nir, "Shear-induced particle migration in a polydisperse concentrated suspension," *Journal of Rheology*, vol. 42, pp. 1329 – 1348, 1998.

[52] P. R. Nott and J. F. Brady, "Pressure-driven flow of suspensions - simulation and theory," *Journal of Fluid Mechanics*, vol. 275, pp. 157 – 199, 1994.

[53] J. F. Morris and J. F. Brady, "Pressure-driven flow of a suspension: Buoyancy effects," *International Journal of Multiphase Flow*, vol. 24, pp. 105 – 130, 1998.

[54] J. F. Morris and F. Boulay, "Curvilinear flows of noncolloidal suspensions: The role of normal stress," *Journal of Rheology*, vol. 43, p. 1213, 1999.

[55] J. T. Norman, *Imaging Particle Migration with Electrical Impedance Tomography: An investigation into the behavior and modeling of suspension flows*. PhD thesis, University of Texas at Austin, 2004.

[56] A. Ramachandran and D. T. Leighton, "Particle migration in concentrated suspensions undergoing squeeze flow," *Journal of Rheology*, vol. 54, pp. 563 – 589, 2010.

[57] A. Ramachandran and D. T. Leighton, "The infuence of secondary flows induced by normal stress difference on the shear-induced migration of particles in concentrated suspensions," *Journal of Fluid Mechanics*, vol. 603, pp. 207–243, 2008.

[58] F. Boyer, E. Guazzelli, and O. Pouliquen, "Unifying suspension and granular rheology," *Physical Review Letters*, vol. 107, p. 188301, 2011.

[59] S. Dagois-Bohy, S. Hormozi, E. Guazzelli, and O. Pouliquen, "Rheology of dense suspensions of non-colloidal spheres in yield-stress fluids," *Journal of Fluid Mechanics*, vol. 776, p. R2, 2015.

[60] C. Ness and J. Sun, "Shear thickening regimes of dense non-Brownian suspensions," *Soft Matter*, vol. 12, pp. 914 – 924, 2016.

[61] B. Lecampion and D. I. Garagash, "Confined flow of suspensions modelled by a frictional rheology," *Journal of Fluid Mechanics*, vol. 759, pp. 197 – 235, 2014.

[62] C. Chang and R. L. Powell, "Dynamic simulation of bimodal suspensions of hydrodynamically interacting spherical particles," *Journal of Fluid Mechanics*, vol. 253, pp. 1 – 25, 1993.

[63] C. Chang and R. L. Powell, "Self-diffusion of bimodal suspensions of hydrodynamically interacting spherical particles in shear flow," *Journal of Fluid Mechanics*, vol. 281, pp. 51 – 80, 1994.

[64] H. H. Hu, D. D. Joseph, and M. J. Crochet, "Direct simulation of fluid particle motions," *Theoretical and Computational Fluid Dynamics*, vol. 3, pp. 285–306, Sep 1992.

[65] N. A. Patankar, P. Singh, D. D. Joseph, R. Glowinski, and T.-W. Pan, "A new formulation of the distributed lagrange multiplier/fictitious domain method for particulate flows," *International Journal of Multiphase Flow*, vol. 26, pp. 1509–1524, 2000.

[66] S. V. Apte, M. Martin, and N. A. Patankar, "A numerical method for fully resolved simulation (FRS) of rigid particleâĂŞflow interactions in complex flows," *Journal of Computational Physics*, vol. 228, no. 8, pp. 2712 – 2738, 2009.

[67] R. Glowinski, T.-W. Pan, T. Hesla, and D. Joseph, "A distributed Lagrange multiplier/fictitious domain method for particulate flows," *International Journal of Multiphase Flow*, vol. 25, no. 5, pp. 755 – 794, 1999.

[68] A. G. Kidanemariam, C. Chan-Braun, T. Doychev, and M. Uhlmann, "Direct numerical simulation of horizontal open channel flow with finite-size, heavy particles at low solid volume fraction," *New Journal of Physics*, vol. 15, p. 025031, Feb. 2013.

[69] T. Wu, X. Shao, and Z. Yu, "Fully resolved numerical simulation of turbulent pipe flows laden with large neutrally-buoyant particles," *Journal of Hydrodynamics, Series B*, vol. 23, no. 1, pp. 21 – 25, 2011.

[70] E. Biegert, B. Vowinckel, and E. Meiburg, "A collision model for grain-resolving simulations of flows over dense, mobile, polydisperse granular sediment beds," *Journal of Computational Physics*, vol. 340, pp. 105 – 127, 2017.

[71] B. Vowinckel, T. Kempe, and J. Frohlich, "Fluid-particle interaction in turbulent open channel flow with fully-resolved mobile beds," *Advances in Water Resources*, vol. 72, no. Supplement C, pp. 32 – 44, 2014.

[72] H. Tang, W. Grivas, D. Homentcovschi, J. Geer, and T. Singler, "Stability considerations associated with the meniscoid particle band at advancing interfaces in Hele-Shaw suspension flow," *Physical Review Letters*, vol. 85, pp. 2112 – 2115, 2000.

[73] H. K. Kytomaa and S. W. Corrington, "Ultrasonic imaging velocimetry of transient liquefaction of cohesionless particulate media," *International Journal of Multiphase Flow*, vol. 20, pp. 915–926, 1994.

[74] P.-G. de Gennes, F. Brochard-Wyart, and D. Quere, *Capillarity an wetting phenomena: drops, bubbles, pearls, waves*. 2004.

[75] R. Jain, R. Kasturi, and B. G. Schunck, *Machine Vision*. New York, NY, USA: McGraw-Hill, Inc., 1995.

[76] R. Jain, R. Kasturi, and B. G. Schunck, "Machine vision," ch. 5, New York, NY, USA: McGraw-Hill, Inc., 1995.

[77] W. K. Pratt, *Digital Image Processing*. John Wiley & Sons, Inc, 3rd ed., 2001.

[78] J. W. Tukey, *Exploratory data analysis*. MA: Addison-Wesley, 1971.

[79] Y. Shan, M. Normand, and M. Peleg, "Estimation of the surface concentrationof adhered particles by colour imaging," *Powder Technology*, vol. 92, pp. 147–153, 1997.

[80] J. Abanades and S. Atares, "Investigation of solid mixing in a deep fluidized bed of coarse particles by image analysis," in *CdROM proceedings*, (Brighton UK IChemE), World Congress on Particle Technology 3, 1998.

[81] K. Lim, V. Gururajan, and P. Agarwal, "Mixing of homogeneous solids in bubbling fluidised beds: Theoretical modelling and experimental investigation using digital image analysis," *Chemical Engineering Science*, vol. 48, pp. 2251–2265, 1993.

[82] G. Grasa and J. C. Abanades, "A calibration procedure to obtain solid concentrations from digital images of bulk powders," *Powder Technology*, vol. 114, pp. 125 – 128, 2001.

[83] E. Alpadydin, *Introduction to Machine Learning, Second Edition*. MIT Press, 2009.

[84] T. G. Beckwith and R. D. Marangoni, *Mechanical Measurements*. Addison-Wesley, New York, 5th ed., 1993.

[85] G. M. Homsy, "Viscous fingering in porous media," *Annual Reviews of Fluid Mechanics*, vol. 19, pp. 271 – 311, 1987.

[86] D. Pihler-Puzovic, R. Perillat, M. Russell, A. Juel, and M. Heil, "Modelling the suppression of viscous fingering in elastic-walled Hele-Shaw cells," *Journal of Fluid Mechanics*, vol. 731, pp. 162 – 183, 2013.

[87] A. Ramachandran and D. T. Leighton, "The effect of gravity on the meniscus accumulation phenomenon in a tube," *Journal of Rheology*, vol. 51, p. 1073, 2007.

[88] R. H. Davis and A. Acrivos, "Sedimentation of noncolloidal particles at low Reynolds numbers," *Annual Reviews of Fluid Mechanics*, vol. 17, pp. 91 – 118, 1985.

[89] I. E. Zarraga, D. A. Hill, and D. T. Leighton, "The characterization of the total stress of concentrated suspensions of non-colloidal spheres in Newtonian fluids," *Journal of Rheology*, vol. 44, pp. 185 – 220, 2000.

[90] R. M. Miller and J. F. Morris, "Normal stress-driven migration and axial development in pressure-driven flow of concentrated suspensions," *Journal of Non-Newtonian Fluid Mechanics*, vol. 135, pp. 149 – 165, 2006.

[91] J. F. Brady, "Macroscopic modeling of viscous suspension flows," *Applied Mechanics Review*, vol. 6, pp. S229 – S235, 1994.

[92] J. W. Swan and J. F. Brady, "The hydrodynamics of confined dispersions," *Journal of Fluid Mechanics*, vol. 687, pp. 254 – 299, 2011.

[93] D. Brutin, B. Sobac, and C. Nicloux, "Influence of substrate nature on the evaporation of a sessile drop of blood," *Journal of Heat Transfer*, vol. 134, p. 061101, 2012.

[94] F. Xu, J. Kim, and S. Lee, "Particle-induced viscous fingering," *Journal of Non-Newtonian Fluid Mechanics*, vol. 238, pp. 92–99, 2016.

APPENDIX A

SUSPENSION BALANCE MODEL FOR SINGLE DISPERSE SUSPENSION SYSTEM

For mixture, the governing equations are:

$$\nabla \cdot \boldsymbol{v} = 0 \tag{A.1}$$

$$\rho g + \nabla \cdot \boldsymbol{\Sigma} = 0 \tag{A.2}$$

For particle phase, the governing equations are:

$$\frac{\partial \phi}{\partial t} + \nabla \cdot (\phi \boldsymbol{v}^p) = 0 \tag{A.3}$$

$$\nabla \cdot \boldsymbol{\Sigma}^p + \rho_p g \phi + \boldsymbol{F} = 0 \tag{A.4}$$

The relation between $\vec{v}$ and $\vec{v}^p$ is descried as follows:

$$\vec{v} = \phi \vec{v}^p + (1 - \phi)\vec{v}^f \tag{A.5}$$

And inter-phase drag force $\boldsymbol{F}$ is given as:

$$\boldsymbol{F} = -\frac{9\eta_l}{2a^2}\frac{\phi}{f(\phi)}(\boldsymbol{v}^p - \boldsymbol{v}). \tag{A.6}$$

where η_l is the viscosity of carrying fluid and $f(\phi)$ is referred to as a hindrance function,

which is an empirical function.

For the particle phase, the stress tensor consists of the normal particle stress and the stress from viscosity:

$$\boldsymbol{\Sigma}^p = \boldsymbol{\Sigma}^p_n + 2\eta_l \hat{\eta_p}(\phi)\boldsymbol{E} \tag{A.7}$$

where $\hat{\eta_p}(\phi)$ is the non-dimensional empirical particle shear viscosity, which is non-dimensionalized by η_l and $\boldsymbol{E}$ is the symmetric component of the strain tensor, expressed as $\boldsymbol{E} = \frac{1}{2}[\nabla \boldsymbol{v} + (\nabla \boldsymbol{v})^T]$.

To simplify, the normal shear stress $\boldsymbol{\Sigma}^p_n$ can be decomposed as:

$$\boldsymbol{\Sigma}^p_n = -\Pi \boldsymbol{I} + \boldsymbol{\Sigma}^p_{nd} \tag{A.8}$$

where Π is the particle pressure, defined as trace of the particle normal stress tensor $\Pi = -\frac{1}{3} trace(\boldsymbol{\Sigma}^p_n)$, and $\boldsymbol{\Sigma}^p_{nd}$ is the normal stress difference.

By defining an empirical term of the particle suspension viscosity η_s, which could be expressed in dimensionless form as $\hat{\eta_s} = 1 + \hat{\eta_p}$ and plugging into Eq. (A.7), we acquire:

$$\boldsymbol{\Sigma}^p = -\Pi \boldsymbol{I} + 2\eta_l(\hat{\eta_s} - 1)\boldsymbol{E} + \boldsymbol{\Sigma}^p_{nd} \tag{A.9}$$

The suspension stress with the particle stress included thus is expressed as:

$$\boldsymbol{\Sigma} = -(p^f + \Pi)\boldsymbol{I} + \eta_l \hat{\eta_s} 2\boldsymbol{E} + \boldsymbol{\Sigma}^p_{nd} \tag{A.10}$$

By defining the suspension pressure P as $P = p^f + \Pi$ and plugging Eq. (A.10) into Eq. (A.2) and neglecting the inertia term, we have:

$$0 = -\nabla P + 2\eta_l \nabla \cdot (\hat{\eta_s}\boldsymbol{E}) + \nabla \cdot \boldsymbol{\Sigma}^p_{nd} \tag{A.11}$$

Combining Eq. (A.1) and Eq. (A.3) gives:

$$\frac{\partial \phi}{\partial t} + \vec{v} \cdot \nabla \phi = -\nabla \cdot [\phi(\vec{v}^p - \vec{v})] \tag{A.12}$$

In the last equation, the term $\phi(\vec{v}^p - \vec{v})$ describes the flux of particle migration and can be related to the force F in Eq. (A.4) by $\phi(\vec{v}^p - \vec{v}) = -\frac{2a^2 f(\phi)}{9\eta_l} F$. Applying all these and combining Eq. (A.4) and Eq. (A.12) gives:

$$\frac{\partial \phi}{\partial t} + \vec{v} \cdot \nabla \phi = -\frac{2a^2 f(\phi)}{9\eta_l} \nabla \cdot [f(\phi) \nabla \cdot \ \mathbf{\Sigma}^p] \tag{A.13}$$

In cylindrical coordinate, we can define the velocity vector as $\vec{v} = v_r \vec{e}_r + v_\theta \vec{e}_\theta + v_z \vec{e}_z$ and the r, θ, z are the flow direction, vorticity direction and shear direction, respectively. According to research in past, the particle normal stress could also be empirically defined as:

$$\mathbf{\Sigma}_n^p = -\eta_l \dot{\gamma} \hat{\eta_n}(\phi) \begin{bmatrix} \lambda_2 & & \\ & \lambda_1 & \\ & & 1 \end{bmatrix} \tag{A.14}$$

where the λ_1 and λ_2 are empirical values.

By expanding all terms, the particulate stress tensor takes the following form,

$$\mathbf{\Sigma}^p = \begin{bmatrix} -\eta_l \dot{\gamma} \lambda_2 + 2\eta_l(\hat{\eta_s} - 1)\frac{\partial v_r}{\partial r} & \eta_l(\hat{\eta_s} - 1)(\frac{1}{r}\frac{\partial v_r}{\partial \theta} - \frac{v_\theta}{r} + \frac{\partial v_\theta}{\partial r}) & \eta_l(\hat{\eta_s} - 1)(\frac{\partial v_r}{\partial z} + \frac{\partial v_z}{\partial r}) \\ \eta_l(\hat{\eta_s} - 1)(\frac{\partial v_r}{\partial z} + \frac{\partial v_z}{\partial r}) & -\eta_l \dot{\gamma} \lambda_3 + \eta_l(\hat{\eta_s} - 1)(\frac{2}{4}\frac{\partial v_\theta}{\partial \theta} + \frac{2v_r}{r}) & \eta_l(\hat{\eta_s} - 1)(\frac{\partial v_\theta}{\partial z} + \frac{1}{r}\frac{\partial v_z}{\partial \theta}) \\ \eta_l(\hat{\eta_s} - 1)(\frac{\partial v_r}{\partial z} + \frac{\partial v_z}{\partial r}) & \eta_l(\hat{\eta_s} - 1)(\frac{\partial v_\theta}{\partial z} + \frac{1}{r}\frac{\partial v_z}{\partial \theta}) & -\eta_l \dot{\gamma} \hat{\eta_n} + 2\eta_l(\hat{\eta_s} - 1\frac{\partial v_z}{\partial z}) \end{bmatrix}$$

Thus, the divergence of $\mathbf{\Sigma}^p$ is expressed in the following matrix,corresponding to the r, θ, z directions.

$$\nabla \cdot \mathbf{\Sigma}^p = \begin{bmatrix} \frac{1}{r}\frac{\partial}{\partial r}[-\eta_l \dot{\gamma} \hat{\eta_n} \lambda_2 r + 2\eta_l(\hat{\eta_s} - 1) r \frac{\partial v_r}{\partial r}] + \frac{\partial}{\partial z}[\eta_l(\hat{\eta_s} - 1)\frac{\partial v_r}{\partial z}] \\ \frac{1}{r}\frac{\partial}{\partial \theta}[-\eta_l \dot{\gamma} \hat{\eta_n} \lambda_3 + 2\eta_l(\hat{\eta_s} - 1)\frac{v_r}{r}] \\ \frac{1}{r}\frac{\partial}{\partial r}[r\eta_l(\hat{\eta_s} - 1)\frac{\partial v_r}{\partial z}] + \frac{\partial}{\partial z}(\eta_l \dot{\gamma} \hat{\eta_n}) \end{bmatrix} \tag{A.15}$$

If we non-sensationalize the above equations making use of the scales below

$$h = h^* b \quad r = r^* R_0 \quad \epsilon = \frac{b}{R_0} \ll 1 \quad \dot{\gamma} = \dot{\gamma}^* \frac{U_0}{b}$$
$$\Sigma_{ij} = \Sigma^*_{ij} \frac{\eta_l U_0}{b} \quad P = P^* \frac{\eta_l U_0}{b\epsilon} \quad t = t^* \frac{R_0}{U_0}$$

the divergence then becomes:

$$\nabla \cdot \mathbf{\Sigma}^{p*} = \frac{U_0 \eta_l}{b} \begin{bmatrix} \frac{1}{b}\frac{\partial}{\partial z^*}[(\hat{\eta_s} - 1)\frac{\partial v_r^*}{\partial z^*}] \\ \frac{1}{R_0}\frac{\partial}{\partial \theta}[-\dot{\gamma}^* \hat{\eta_n} \lambda_3^* \frac{\eta_l U_0}{b} + 2(\hat{\eta_s} - 1)\frac{b}{R_0}\frac{v_r^*}{r^*}] \\ \frac{1}{b}\frac{\partial}{\partial z^*}[-\dot{\gamma}^* \hat{\eta_n}] \end{bmatrix} \tag{A.16}$$

Considering the lubrication theory in the r direction, we have:

$$\frac{\partial P^*}{\partial r^*} = \frac{\partial}{\partial z^*}(\eta_s(\hat{\phi})\dot{\gamma}^*) \tag{A.17}$$

Equating Eq. (A.17) and the r component of Eq. (A.16), and then combine with Eq. (A.6), we eventually have the non-dimensional expression for the velocity difference between particle and suspension in r direction:

$$v_r^{p*} - v_r^* = \frac{2}{9}\left(\frac{a}{b}\right)^2 \frac{f(\phi)}{\phi}[\frac{\partial P^*}{\partial r^*} - \frac{\partial^2 v_r^*}{\partial z^{*2}}] \tag{A.18}$$

APPENDIX B

SUSPENSION BALANCE MODEL FOR BI-DISPERSE SUSPENSION SYSTEM

The governing equations for the bulk suspension are given as follows:

$$\nabla \cdot \boldsymbol{u} = 0 \tag{B.1}$$

$$\nabla \cdot \boldsymbol{\Sigma} = 0 \tag{B.2}$$

Expanding the Eq. B.1, the conservation law is expressed in the following non-dimensionalized form:

$$\frac{\partial u_r}{\partial r} + \frac{1}{r}(\frac{\partial u_\theta}{\partial \theta} + u_r) + \frac{\partial u_z}{\partial z} = 0 \tag{B.3}$$

where the scales implemented are $r = Rr^*$, $z = bz^*$, $u_r = U_0 {u_r}^*$, $u_\theta = U_0 {u_\theta}^*$, $u_z = \epsilon U_0 {u_z}^*$ with ϵ defined as $\epsilon = \frac{b}{R} \ll 1$. The stars in the non-dimensionalized form are dropped for simplicity.

For the particulate phases,

$$\tfrac{\partial \phi_i}{\partial t} + \nabla \cdot (\phi_i \boldsymbol{u}_i^p) = 0 \tag{B.4}$$

$$\nabla \cdot \boldsymbol{\Sigma}_i^p + \boldsymbol{F}_i = 0 \tag{B.5}$$

where $\boldsymbol{u}$ and Σ represent the velocity vector and the stress tensor respectively, the superscript p indicates those terms are for particulate phases and the subscript i takes the values of $i = 1, 2$, corresponding to two different species of particles. The inner drag force F_i

and the particulate stress tensor are given as:

$$\boldsymbol{F}_i = -\frac{9\eta_l}{2a_i^2}\frac{\phi_i}{f(\phi)}(\mathbf{u}_i^p - \mathbf{u}) \tag{B.6}$$

$$\boldsymbol{\Sigma}_i^p = 2\eta_l\hat{\eta_{p_i}}\boldsymbol{E} + \boldsymbol{\Sigma}_{n_i}^p \tag{B.7}$$

with the empirical expression being:

$$\boldsymbol{\Sigma}_{n_i}^p = -\eta_l\hat{\eta}_n\dot{\gamma}\frac{\phi_i}{\sum_{j=1}^n \phi_j}\begin{bmatrix}\lambda_2 & & \\ & \lambda_1 & \\ & & 1\end{bmatrix} \tag{B.8}$$

$$\hat{\eta}_{p_i} = (\hat{\eta}_s - 1)\frac{\phi_i}{\phi} \tag{B.9}$$

$$\hat{\eta}_s = (1 + \frac{\alpha\phi}{1 - \frac{\phi}{\phi_m}})^{3.3\phi_m} \tag{B.10}$$

$$\hat{\eta}_n = (\frac{\phi}{\phi_m})^2 K_n\hat{\eta}_s \tag{B.11}$$

$$f(\phi) = (1-\phi)^{4.4} \tag{B.12}$$

where η_l refers to the liquid viscosity, $\hat{\eta}_n$ is the normal viscosity, $\hat{\eta}_p$ is the particulate viscosity, $\hat{\eta}_s$ is the shear viscosity, $f(\phi)$ is the hindrance function, α and K_n are empirical constants. Another constitute equation is the expression for total stress tensor of the bulk suspension, which takes the following form, with p being the hydrostatic pressure and $\boldsymbol{E}$ being the rate of strain:

$$\boldsymbol{\Sigma} = -p\boldsymbol{I} + 2\eta_l\boldsymbol{E} + \boldsymbol{\Sigma}_1^p + \boldsymbol{\Sigma}_2^p \tag{B.13}$$

where $\boldsymbol{E} = \frac{1}{2}[\nabla\boldsymbol{v} + (\nabla\boldsymbol{v})^T]$.

By plugging in all terms given above into Eq. B.5, we have the following expressions for the divergence of the particulate stress tensor.

$$\nabla \cdot \mathbf{\Sigma}_i^p = \{\frac{\partial}{\partial r}(2\eta_l\hat{\eta}_{p_i}\frac{\partial u_r}{\partial r} - \eta_l\hat{\eta}_n\dot{\gamma}\frac{\phi_i}{\phi}\lambda_2) + \frac{1}{r}\frac{\partial}{\partial\theta}[\eta_l\hat{\eta}_{p_i}(\frac{1}{r}\frac{\partial u_r}{\partial\theta} - \frac{u_\theta}{r} + \frac{\partial u_\theta}{\partial r})]$$
$$+ \frac{1}{r}\hat{\eta}_n\dot{\gamma}\frac{\phi_i}{\phi}\eta_l(\lambda_1 - \lambda_2) + \frac{2}{r}\eta_l\hat{\eta}_{p_i}(\frac{\partial u_r}{\partial r} - \frac{1}{r}\frac{\partial u_\theta}{\partial\theta} - \frac{u_r}{r}) + \frac{\partial}{\partial z}[\eta_l\hat{\eta}_{p_i}(\frac{\partial u_z}{\partial r} + \frac{\partial u_r}{\partial z})]\}\boldsymbol{r}$$
$$+ \{\frac{\partial}{\partial r}[\eta_l\hat{\eta}_{p_i}(\frac{1}{r}\frac{\partial u_r}{\partial\theta} - \frac{u_\theta}{r} + \frac{\partial u_\theta}{\partial r})] + \frac{1}{r}\frac{\partial}{\partial\theta}[\frac{2}{r}\eta_l\hat{\eta}_{p_i}(\frac{\partial u_\theta}{\theta} + u_r) - \eta_l\hat{\eta}_n\lambda_1\frac{\phi_i}{\phi}]$$
$$+ \frac{2}{r}\eta_l\hat{\eta}_{p_i}(\frac{1}{r}\frac{\partial u_r}{\partial\theta} - \frac{u_\theta}{r} + \frac{\partial u_\theta}{\partial r}) + \frac{\partial}{\partial z}[\eta_l\hat{\eta}_{p_i}(\frac{1}{r}\frac{\partial u_z}{\partial\theta} + \frac{\partial u_\theta}{\partial z})]\}\boldsymbol{\theta}$$
$$+ \{\frac{\partial}{\partial r}[\eta_l\hat{\eta}_{p_i}(\frac{\partial u_r}{\partial z} + \frac{\partial u_z}{\partial r})] + \frac{1}{r}\frac{\partial}{\partial\theta}[\eta_l\hat{\eta}_{p_i}(\frac{\partial u_\theta}{\partial z} + \frac{1}{r}\frac{\partial u_z}{\partial\theta})]$$
$$+ \frac{1}{r}\eta_l\hat{\eta}_{p_i}(\frac{\partial u_r}{\partial z} + \frac{\partial u_z}{\partial r}) + \frac{\partial}{\partial z}(2\eta_l\hat{\eta}_{p_i}\frac{\partial u_z}{\partial z} - \eta_l\hat{\eta}_n\dot{\gamma}\frac{\phi_i}{\phi})\}\boldsymbol{z} \quad \text{(B.14)}$$

The expression can be non-dimensionalized with scales $r = Rr^*$, $z = bz^*$, $u_r = U_0{u_r}^*$, $u_\theta = U_0{u_\theta}^*$, $u_z = \epsilon U_0{u_z}^*$, $\dot{\gamma} = \frac{U_0}{b}\dot{\gamma}^*$, $\Sigma_{ij} = \frac{\eta_l U_0}{b}\Sigma_{ij}^*$ with ϵ defined as $\epsilon = \frac{b}{R} \ll 1$, which gives,

$$\nabla \cdot \Sigma_i^p = \frac{\eta_l U_0}{b^2}\{\frac{\partial}{\partial r}(2\epsilon^2\hat{\eta}_{p_i}\frac{\partial u_r}{\partial r} - \epsilon\hat{\eta}_n\dot{\gamma}\frac{\phi_i}{\phi}\lambda_2) + \frac{1}{r}\frac{\partial}{\partial\theta}[\hat{\eta}_{p_i}(\frac{\epsilon^2}{r}\frac{\partial u_r}{\partial\theta} - \epsilon^2\frac{u_\theta}{r} + \epsilon\frac{\partial u_\theta}{\partial r})]$$
$$+ \frac{\epsilon}{r}\hat{\eta}_n\dot{\gamma}\frac{\phi_i}{\phi}\eta_l(\lambda_1 - \lambda_2) + \frac{2}{r}\hat{\eta}_{p_i}(\epsilon^2\frac{\partial u_r}{\partial r} - \frac{\epsilon^2}{r}\frac{\partial u_\theta}{\partial\theta} - \epsilon^2\frac{u_r}{r}) + \frac{\partial}{\partial z}[\hat{\eta}_{p_i}(\epsilon^2\frac{\partial u_z}{\partial r} + \frac{\partial u_r}{\partial z})]\}\boldsymbol{r}$$
$$+ \frac{\eta_l U_0}{b^2}\{\frac{\partial}{\partial r}[\hat{\eta}_{p_i}(\frac{\epsilon^2}{r}\frac{\partial u_r}{\partial\theta} - \epsilon^2\frac{u_\theta}{r} + \epsilon^2\frac{\partial u_\theta}{\partial r})] + \frac{1}{r}\frac{\partial}{\partial\theta}[\frac{2\epsilon^2}{r}\hat{\eta}_{p_i}(\frac{\partial u_\theta}{\theta} + u_r) - \epsilon\hat{\eta}_n\lambda_1\frac{\phi_i}{\phi}]$$
$$+ \frac{2}{r}\hat{\eta}_{p_i}(\frac{\epsilon^2}{r}\frac{\partial u_r}{\partial\theta} - \epsilon^2\frac{u_\theta}{r} + \epsilon^2\frac{\partial u_\theta}{\partial r}) + \frac{\partial}{\partial z}[\hat{\eta}_{p_i}(\frac{\epsilon^2}{r}\frac{\partial u_z}{\partial\theta} + \frac{\partial u_\theta}{\partial z})]\}\boldsymbol{\theta}$$
$$+ \frac{\eta_l U_0}{b^2}\{\frac{\partial}{\partial r}[\hat{\eta}_{p_i}(\epsilon\frac{\partial u_r}{\partial z} + \epsilon^3\frac{\partial u_z}{\partial r})] + \frac{1}{r}\frac{\partial}{\partial\theta}[\hat{\eta}_{p_i}(\epsilon\frac{\partial u_\theta}{\partial z} + \frac{\epsilon^2}{r}\frac{\partial u_z}{\partial\theta})] + \frac{1}{r}\hat{\eta}_{p_i}(\epsilon\frac{\partial u_r}{\partial z} + \epsilon^3\frac{\partial u_z}{\partial r})$$
$$+ \frac{\partial}{\partial z}(2\epsilon\hat{\eta}_{p_i}\frac{\partial u_z}{\partial z} - \hat{\eta}_n\dot{\gamma}\frac{\phi_i}{\phi})\}\boldsymbol{z} \quad \text{(B.15)}$$

Note that the non-dimensionalized force $\boldsymbol{F}$ can also be expanded in vector form as:

$$\boldsymbol{F} = \frac{9\eta_l U_0}{2a_i^2}\frac{\phi_i}{f(\phi)}[(u_{ir}^p - u_r)\boldsymbol{r} + (u_{i\theta}^p - u_\theta)\boldsymbol{\theta} + (u_{iz}^p - u_z)\boldsymbol{z}] \tag{B.16}$$

By order matching, we find the govening equation for the particulate phase to the leading order,

$$o(\frac{1}{\epsilon}) \qquad u_{ir}^p - u_r = 0 \tag{B.17}$$

$$o(\frac{1}{\epsilon}) \qquad u_{i\theta}^p - u_\theta = 0 \tag{B.18}$$

$$o(1) \qquad \frac{9\epsilon b^2}{2a_i^2}\frac{\phi_i}{f(\phi)}(u_{iz}^p - u_z) = \frac{\partial}{\partial z}(-\hat{\eta}_n\dot{\gamma}\frac{\phi_i}{\phi}) \tag{B.19}$$

$$\tag{B.20}$$

For the bulk suspension, we follow same procedures to expand all terms and non-dimensionalize each variable and get the following equations in different directions,

$\boldsymbol{r}\ direction:$

$$\begin{aligned}\frac{\partial P}{\partial r} &= 2\epsilon^2\frac{\partial}{\partial r}(\hat{\eta}_s\frac{\partial u_r}{\partial r}) - \epsilon\frac{\partial}{\partial r}(\hat{\eta}_n\lambda_2\dot{\gamma}) + \frac{\epsilon^2}{r^2}\frac{\partial}{\partial\theta}(\hat{\eta}_s\frac{\partial u_r}{\partial\theta}) - \frac{\epsilon^2}{r^2}\frac{\partial}{\partial\theta}(\hat{\eta}_s u_\theta) + \frac{\epsilon^2}{r}\frac{\partial}{\partial\theta}(\hat{\eta}_s\frac{\partial u_\theta}{r}) \\ &+ \frac{\epsilon}{r}\hat{\eta}_n\dot{\gamma}(\lambda_1 - \lambda_2) + \frac{2\epsilon^2}{r}\hat{\eta}_s(\frac{\partial u_r}{\partial r} - \frac{\partial u_\theta}{\partial\theta} - u_r) + \epsilon^2\frac{\partial}{\partial z}(\hat{\eta}_s\frac{\partial u_z}{\partial r}) + \frac{\partial}{\partial z}(\hat{\eta}_s\frac{\partial u_r}{\partial z})\end{aligned} \tag{B.21}$$

$\boldsymbol{\theta}$ *direction* :

$$\frac{1}{r}\frac{\partial P}{\partial \theta} = \epsilon^2\frac{\partial}{\partial r}(\frac{\hat{\eta}_s}{r}\frac{\partial u_r}{\partial \theta}) - \epsilon^2\frac{\partial}{\partial r}(\hat{\eta}_s\frac{u_\theta}{r}) + \epsilon^2\frac{\partial}{\partial r}(\hat{\eta}_s\frac{\partial u_\theta}{\partial r}) + \frac{2\epsilon^2}{r}\frac{\partial}{\partial \theta}(\hat{\eta}_s\frac{\partial u_\theta}{\partial \theta}) + \frac{2\epsilon^2}{r}\frac{\partial}{\partial \theta}(\hat{\eta}_s u_r)$$
$$- \frac{\epsilon}{r}\frac{\partial}{\partial \theta}(\hat{\eta}_n\dot{\gamma}\lambda_1) + \frac{2\epsilon^2}{r}\hat{\eta}_s\frac{\partial u_r}{\partial \theta} - \frac{2\epsilon^2}{r}\hat{\eta}_s u_\theta + 2\epsilon^2\hat{\eta}_s\frac{\partial u_\theta}{r} + \frac{\epsilon^2}{r}\frac{\partial}{\partial z}(\hat{\eta}_s\frac{\partial u_z}{\partial \theta}) + \frac{\partial}{\partial z}(\hat{\eta}_s\frac{\partial u_\theta}{\partial z}) \tag{B.22}$$

$\boldsymbol{z}$ *direction* :

$$\frac{1}{\epsilon}\frac{\partial P}{\partial z} = \epsilon\frac{\partial}{\partial r}(\hat{\eta}_s\frac{\partial u_r}{\partial z}) + \epsilon^3\frac{\partial}{\partial r}(\hat{\eta}_s\frac{\partial u_z}{\partial r}) + \frac{\epsilon}{r}\frac{\partial}{\partial \theta}(\hat{\eta}_s\frac{\partial u_\theta}{\partial z}) + \frac{\epsilon^3}{r^2}\frac{\partial}{\partial \theta}(\hat{\eta}_s\frac{\partial u_z}{\partial \theta}) + \frac{\epsilon}{r}\hat{\eta}_s\frac{\partial u_r}{\partial z}$$
$$+ \frac{\epsilon^3}{r}\hat{\eta}_s\frac{\partial u_z}{\partial r} + 2\epsilon\frac{\partial}{\partial z}(\hat{\eta}_s\frac{\partial u_z}{\partial z}) - \frac{\partial}{\partial z}(\hat{\eta}_n\dot{\gamma}) \tag{B.23}$$

Thus to the leading order, the governing equations for the bulk suspension are,

$$o(1) \qquad \frac{\partial P}{\partial r} = \frac{\partial}{\partial z}(\hat{\eta}_s\frac{\partial u_r}{\partial z}) \tag{B.24}$$

$$o(1) \qquad \frac{1}{r}\frac{\partial P}{\partial \theta} = \frac{\partial}{\partial z}(\hat{\eta}_s\frac{\partial u_\theta}{\partial z}) \tag{B.25}$$

$$o(\frac{1}{\epsilon}) \qquad \frac{\partial P}{\partial z} = 0 \tag{B.26}$$

So far, the system is fully described with leading order governing equations listed above. By rearranging terms and combining the equations, we have the following equation, which is numerically solvable:

$$\frac{\eta_n}{\eta_s}\frac{\phi_i}{\phi}z = (\eta_n\dot{\gamma}\frac{\phi_i}{\phi})(\frac{\partial P}{\partial r}) = const \tag{B.27}$$

The problem is closed if we impose the following constraints relating the flow rate to the

velocity as well as the concentration profiles:

$$Q = \int_{-\frac{h}{2}}^{\frac{h}{2}} u_r dz$$
$$Q\phi_{0i} = \int_{-\frac{h}{2}}^{\frac{h}{2}} u_{ri}\phi_i dz$$

The momentum equation can actually be combined with the transport equation to provide us information of the dependence of ϕ on time in radial direction. Given Eq. B.6 and Eq. B.5, it is easy to get the following expression by simple rearrangement.

$$\boldsymbol{u}_i^p = \frac{2a_i^2}{9\eta_l}\frac{f(\phi)}{\phi}\nabla\cdot\boldsymbol{\Sigma}_i^p + \boldsymbol{u} \tag{B.28}$$

Combining the above Eq. B.28 and the transport equation (conservation of mass) Eq. B.4 for particulate phase, we get the following expression after rearrangement,

$$0 = \frac{\partial\phi_i}{\partial t} + \frac{2a_i^2}{9\eta_l}\nabla\cdot[f(\phi)\nabla\cdot\boldsymbol{\Sigma}_i^p] + \boldsymbol{u}\cdot\nabla\phi_i \tag{B.29}$$

Following same procedure as in first section, the yield equation to the leading order in ϵ is,

$$\frac{2a_i^2}{9b^2\epsilon}\frac{\partial}{\partial z}[f(\phi)\frac{\partial}{\partial z}(-\hat{\eta}_n\dot{\gamma}\frac{\phi_i}{\phi})] + u_r\frac{\partial\phi_i}{\partial r} + \frac{u_\theta}{r}\frac{\partial\phi_i}{\partial\theta} + u_z\frac{\partial\phi_i}{\partial z} + \frac{\partial\phi_i}{\partial t} = 0 \tag{B.30}$$

It's worth mentioning that in our current experimental setup, the particle size $a \sim 0.1mm$, the gap size $b \sim 1mm$, thus we have $\frac{2a_i^2}{9b^2\epsilon} \sim o(1)$, which is essential to keep all the terms in Eq.(B.30).

Taking into consideration the fact that it doesn't hurt to assume that the velocity in r direction is inverse proportional to r and the velocity in θ direction is independent of θ, it's straightforward to draw the conclusion from conservation of mass that $u_z = 0$. Thus

Eq.(B.30) further reduces to the following PDE, which is ready to be solved with proper boundary and initial conditions.

$$\frac{2a_i^2}{9b^2\epsilon}\frac{\partial}{\partial z}[f(\phi)\frac{\partial}{\partial z}(-\hat{\eta}_n\dot{\gamma}\frac{\phi_i}{\phi})] + \frac{\partial\phi_i}{\partial t} = 0 \tag{B.31}$$